Titre: Title:	Development of Phase-Shifting Profilometry for 3D Brain Cavity Reconstruction and in vivo Detection of Intrinsic Fluorescence Through a Neurosurgical Microscope
Auteur: Author:	Leticia Angulo Rodriguez
Date:	2018
Type:	Mémoire ou thèse / Dissertation or Thesis
Référence: Citation:	Angulo Rodriguez, L. (2018). Development of Phase-Shifting Profilometry for 3D Brain Cavity Reconstruction and in vivo Detection of Intrinsic Fluorescence Through a Neurosurgical Microscope [Ph.D. thesis, École Polytechnique de Montréal]. PolyPublie. https://publications.polymtl.ca/3170/

UNIVERSITÉ DE MONTRÉAL

DEVELOPMENT OF PHASE-SHIFTING PROFILOMETRY FOR 3D BRAIN CAVITY RECONSTRUCTION AND IN VIVO DETECTION OF INTRINSIC FLUORESCENCE THROUGH A NEUROSURGICAL MICROSCOPE

LETICIA ANGULO RODRIGUEZ

INSTITUT DE GÉNIE BIOMÉDICAL

ÉCOLE POLYTECHNIQUE DE MONTRÉAL

THÈSE PRÉSENTÉE EN VUE DE L'OBTENTION

DU DIPLÔME DE PHILOSOPHIÆ DOCTOR

(GÉNIE BIOMÉDICAL)

JUIN 2018

UNIVERSITÉ DE MONTRÉAL

ÉCOLE POLYTECHNIQUE DE MONTRÉAL

Cette thèse intitulée:

DEVELOPMENT OF PHASE-SHIFTING PROFILOMETRY FOR 3D BRAIN CAVITY RECONSTRUCTION AND IN VIVO DETECTION OF INTRINSIC FLUORESCENCE THROUGH A NEUROSURGICAL MICROSCOPE

présentée par : ANGULO RODRIGUEZ Leticia

en vue de l'obtention du diplôme de : Philosophiæ Doctor

a été dûment acceptée par le jury d'examen constitué de :

Mme SANTATO Clara, Doctorat, présidente

M. LEBLOND Fréderic, Ph. D., membre et directeur de recherche

M. DEHAES Mathieu, Ph. D., membre

M. DE GUISE Jacques A., Ph. D., membre externe

DEDICATION

With immense gratitude and love to my parents, my parents-in-law, my husband and our beloved baby for being a source of motivation and strength in my life

ACKNOWLEDGEMENTS

I would like to express my gratitude to my supervisor, Prof. Frederic Leblond, for accepting me as his first PhD student at Polytechnique Montreal, and for always being open for discussion and to exchange ideas and views. In addition, I thank you for all your help and guidance.

I thank my committee members: Prof. Clara Santato, Prof. Mathieu Dehaes, Prof. Jacques de Guise and Prof. Sofiane Achiche for evaluating my thesis and providing their valuable feedback.

A big thank you to Dr. Kevin Petrecca, Chief of Neurosurgery and head of the Brain Cancer research group at the Montreal Neurological Institute, for testing the device developed in this PhD during brain cancer surgeries, and for continuously giving me inputs on the project at the end of each surgery so I could improve my device further. Thanks as well to the nursing staff at the Montreal Neurological Institute for helping me in every possible way during the late evenings and weekends that I spent there trying to make things work.

Thanks to all my colleagues at the Laboratory of Radiological Optics for sharing their knowledge with me. Catherine St-Pierre, thank you not only for the times you lent me a hand with math and programming but also for allowing me to know more about the culture and language of Quebec. And thanks to all the students that worked with great motivation under my supervision at the lab, especially Youmna Badawy.

I also want to use this opportunity to express my sincere thanks to the technicians in the Department of Engineering Physics: Jean-Paul Levesque, Francis Boutet and Evgueni Babian for helping me build the device that is presented in this thesis piece by piece and for always being available to talk through the device design.

In addition, I would also like to thank the expert scientists Samuel Belanger and Mathias Strupler from whom I learned a lot about optical design and image analysis; thank you Sam and Mathias for helping me and sharing your experience with me since the beginning of my PhD.

Besides, I would like to express my appreciation to Mrs. Amal Bennani, Student Records Officer at the Institute of Biomedical Engineering, who looked after me and helped me complete the graduation requirements for the PhD degree.

Last but not least, I dearly thank the good friends from all around the world that I made in Montreal for being a family when we were thousands of miles away from home. And also thanks to the old friends and family that always sent me words of encouragement. I thank with all my heart my loving parents, Leticia and Emilio, for working so hard to give me and my brother the best education and for instilling values in us, particularly for teaching us the importance of integrity, dedication and hard work; thank you mom for inspiring me and for giving me the confidence to dream big! Also, I would like to extend my deepest gratitude to my biggest supporter, my husband Alexis, for being with me throughout all my graduate studies and for believing in me and at the same time pushing me to reach my goals and do better! And to my parents-in-law: thank you so much, Beatrice and Daniel, for supporting me through the difficult moments as if I was your own daughter. Finally, thanks for the life of my baby girl that came into my life at the end of my PhD; one day you will know how much you encouraged me to write and defend my thesis and how much I have loved you since then.

RÉSUMÉ

Les microscopes neurochirurgicaux ont été conçus pour détecter la fluorescence produite par des tissus biologiques ; de plus, la spectroscopie optique peut être utilisée pour guider une opération chirurgicale telle que la résection d'une tumeur du cerveau. Néanmoins, les microscopes actuels n'ont pas de capacité hyperspectrale, ce qui les empêche d'évaluer quantitativement les propriétés optiques des tissus (absorption et diffusion). Ils ne peuvent utiliser ces marqueurs pour réaliser une correction d'atténuation qui permettrait d'obtenir des valeurs quantifiées de fluorescence. Une première étape importante permettant d'évaluer précisément les propriétés d'absorption et de diffusion des tissus biologiques est la détermination de la forme géométrique de l'échantillon. Cette thèse présente un système hyperspectral intégré dans un microscope neurochirurgical commercial. Un tel système est capable de réaliser deux fonctions : (a) extraire le profil 3D du cerveau ; et, (b) détecter la signature spectrale de l'auto-fluorescence des tissus du cerveau. Ce sont des développements initiaux essentiels en vue de la création de nouveaux équipements qui permettront de quantifier la fluorescence intrinsèque des tissus durant une opération chirurgicale. Ceci dans le but de détecter des anomalies sans ambiguïté.

Un système d'imagerie a été développé et consiste en un Projecteur Digitale de Lumière associé avec un microscope neuro chirurgical permettant à la lumière structurée d'être projetée sur une cavité chirurgicale. La détection est réalisée en utilisant un système hyperspectral de haute sensibilité qui est également couplé avec le microscope à travers un port optique libre. La projection de lumière structurée est utilisée pour réaliser une reconstruction 3D. Elle a été évaluée en utilisant une structure de la forme d'une pyramide avec plusieurs marches, ce qui permet de déterminer l'exactitude et la précision du système de la profilométrie. L'exactitude et la précision moyennes pour toutes les reconstructions de hauteurs des marches des pyramides (de 1.5 à 30 mm) étaient respectivement de 0.3 mm et 0.6 mm. Des mesures de profilométrie à différents angles ont également été effectuées en tournant une plate-forme de ±15°, 30° et 45°. L'erreur de reconstruction moyenne pour tous les angles a été de 1.94 degrés (σ = 1.2 degrés). En outre, un fantôme optique de la forme d'un cerveau avec des propriétés optiques dans des échelles de valeurs physiologiques réalistes a été fabriqué. Son profil a été reconstruit avec une exactitude comparable au test avec des pyramides.

Pour la détection de la fluorescence, le même système de détection a été utilisé mais le Projecteur Digitale de Lumière a été remplacé par une source bleue venant d'un microscope chirurgical. Une technique a été développée pour récupérer la fluorescence intrinsèque des tissus du cerveau et la méthode a été testée *in vivo* durant des opérations de résection de gliome à l'Institut et hôpital neurologique de Montréal. La méthode comprend une calibration technique pour corriger les données de fluorescence hyperspectrale dans le but d'enlever la réponse spectrale et spatiale de l'instrument d'imagerie. Ensuite, un algorithme a été développé pour corriger l'effet de l'atténuation de la lumière sur les propriétés optiques du tissu en normalisant la fluorescence avec des images de réflectance de lumière blanche dans le but de produire des données d'imagerie spécialement reliées à la fluorescence émise par les molécules du tissu. Les données préliminaires d'un cas clinique ont permis de révéler que les tissus en bonne santé ont une fluorescence avec une intensité plus grande que celle des tumeurs, hypothèse qui se retrouve également dans la littérature.

En conclusion, le système d'imagerie développé comme partie intégrante de cette thèse est capable de fournir une hauteur pixel par pixel dans la cavité chirurgicale (profil 3D) et une carte de l'auto-fluorescence de la surface du cerveau.

ABSTRACT

Neurosurgery microscopes have been developed to detect fluorescence associated with biological tissue; in addition, optical spectroscopy can be used to guide surgical procedures including the resection of brain tumors. However, current microscopes do not have hyperspectral capabilities, which prevents these systems from quantitatively evaluating tissue optical properties (absorption and scattering) and use these values to implement an attenuation correction leading to quantified values of fluorescence. An important first step allowing to accurately assessing the absorption and scattering properties of biological tissue is the determination of the geometric shape of the sample. Here we present a hyperspectral system integrated onto a commercial neurosurgical microscope that is capable of supporting two functionalities: (a) extracting the 3D profile of the brain, and (b) detecting the spectral signature of brain tissue autofluorescence. These functionalities represent critical initial advancements towards the development of new devices that will be able to quantify intrinsic tissue fluorescence during surgical procedures in order to unambiguously detect abnormalities.

An imaging system was developed that consists of a Digital Light Projector coupled to a neurosurgical microscope allowing structured light to be projected on the surgical cavity. Detection is achieved using a high sensitivity hyperspectral system also coupled to the microscope through a free optical port. The projection of structured light is used to perform a 3D reconstruction, which was evaluated using a phantom in the shape of a pyramid with multiple steps allowing determining the accuracy and precision of the profilometry system. The average accuracy and precision for all reconstructions of pyramid step heights (from 1.5 to 30 mm) was 0.3 mm and 0.6 mm, respectively. Profilometry measurements at different angles were also acquired by rotating a platform by ±15°, 30° and 45°. The mean reconstruction error for all angles was 1.94° (STD = 1.2°). Additionally, a brain-shaped phantom with optical properties within the range of realistic physiological values was fabricated and its profile was reconstructed with accuracies comparable with the pyramid step phantom.

For fluorescence detection, the same detection system was used but the Digital Light Projector was replaced with the wide-field blue source from a fluorescence neurosurgical microscope. A technique was developed to recover intrinsic brain tissue fluorescence and the

method was tested *in vivo* during glioma resection procedures at the Montreal Neurological Institute and Hospital. The method includes a calibration technique to correct hyperspectral fluorescence data in order to remove the spectral and spatial response of the imaging instrument. Then, an algorithm was developed to correct for the light attenuation effect of tissue optical properties by normalizing the fluorescence with white light reflectance images with the objective to produce imaging data specifically related to fluorescence emitted by tissue molecules. Preliminary data from a clinical case suggested that healthy tissue has higher fluorescence intensity than tumor, which is in line with the literature.

In conclusion, the imaging system developed as part of this thesis is able to provide pixel-by-pixel heights within the surgical cavity (3D profile) and autofluorescence maps of the brain surface.

TABLE OF CONTENTS

LIST OF TABLES

LIST OF FIGURES

LIST OF SYMBOLS AND ABBREVIATIONS

ALA	Aminolevulinic acid
CNR	Contrast-to-noise ratio
CT	Computer tomography
DLP	Digital Light Projector
DMD	Digital Micromirror Device
EM	Electron multiplication
EMCCD	Electron multiplying charge-coupled device
FAD	Flavin adenine dinucleotide
FGS	Fluorescence-guided surgery
FOV	Field of view
FWHM	Full width at half maximum
GBM	Glioblastoma multiforme
HbO	Oxyhemoglobin
HbR	Deoxyhemoglobin
H&E	Hematoxylin and eosin stain
ICCD	Intensified charge-coupled device
IR	Infrared
LED	Light-emitting diode
LCTF	Liquid Crystal Tunable Filter
LRO	Laboratory of Radiological Optics
Neuro	Montreal Neurological Institute and Hospital
MRI	Magnetic resonance imaging

NA	Numerical aperture
NADH	Reduced nicotinamide adenine dinucleotide
NIR	Near infrared region of the electromagnetic spectrum
nm	Nanometers
ns	Nanoseconds
OIR	Optical index ratio
PpIX	Protoporphyrin IX
qFI	Wide-field quantitative fluorescence imaging
REB	Research Ethics Board
Redox	Reduction-oxidation
RMSE	Root Mean Square Error
ROx	Reduction-oxidation ratio
SFDI	Spatial frequency domain imaging
UV	Ultraviolet
μ_a	Absorption coefficient
μ'_s	Reduced scattering coefficient
λ	Wavelength

LIST OF APPENDICES

CHAPTER 1 INTRODUCTION

1.1 Motivation

In the United States, 70% of new cases of malignant primary brain tumors correspond to malignant gliomas [1]. Glioblastoma multiforme (GBM) is a type of glial tumor (grade IV) that constitutes 60-70% of malignant gliomas; only 3.3% of people who suffer from it survive 5 years and the average survival time is 1 year [1]–[3]. Meningioma is another type of tumor (WHO grade from I to III) that accounts for 20% of intracranial tumors [2].

Surgery is the most widespread treatment to treat a brain tumor [4]. The degree of tumor resection, for example, is an important factor for the evolution of a patient with a glioblastoma or meningioma [2], [5]–[11]; however, to completely remove a tumor, the boundary of the tumor region should be identified [4]. Nevertheless, gliomas infiltrate into healthy tissue making complete removal of all cancer tissue very difficult to achieve [12].

Neuronavigation systems are used to guide the surgeon during neurosurgery by showing the same brain structures that are seen in the microscope field of view (FOV) on the preoperative magnetic resonance (MRI) or X-ray (CT) images [13]. CT and MRI can be very useful for the location of a tumor and subsequent removal [14]; the drawback, however, is their lack of sensitivity to trace tumor boundaries, since cancer cells are often found outside the detected tumor margins [15]. In addition, there is an accuracy error of at least 1 cm between the recorded dimensions of the brain in preoperative images and its subsequent deformation due to craniotomy, the use of a retractor and the continuous removal of brain tissue [16]–[18].

Therefore, new tools are needed to assist surgeons in recognizing tumor margins in real time, such as fluorescence-guided surgery (FGS) [19]. Intraoperative fluorescence images can offer high contrast between healthy and cancerous tissue, as well as being safe for the patient since imaging is done using non-ionizing radiation [20], [21]. In addition, accurate delineation of the tumor can help avoid damage to healthy tissue, nerves and blood vessels [19].

Several fiber optic probes have been built for the intraoperative detection of fluorescence and to provide a means to estimate fluorophore concentrations [22], [23]. However, using a probe changes the surgical workflow, *i.e.*, there is disruption in the procedure. Besides, probes

interrogate the tissue of interest at a single point, being unable to assess the entire resection cavity. Therefore, a wide-field imaging system integrated to a surgical microscope was presented by Valdes et al. [24]. This system takes spectral images of protoporphyrin IX (PpIX) fluorescence that results from the administration of exogenous 5-aminolevulinic acid (5-ALA).

However, even if PpIX has received increasing attention over the last decade after demonstrating preferential expression in high-grade gliomas following 5-ALA injection [5], [25]–[29], its use had not been approved in Canada at the time the research reported in this thesis was conducted. For that reason, as part of this PhD project, an imaging device, software and image analysis algorithms were developed to guide the resection of tumors during neurosurgeries through the detection of tissue autofluorescence that does not require administration of exogenous fluorescent chemical compounds. This choice, rather than putting the emphasis on PpIX detection, was not only done to ensure in-human testing of the new techniques in the thesis time-frame but also because tissue autofluorescence presents certain advantages in terms of practicality and eventual clinical use since it avoids potential problems related with regular approval of a drug in conjunction with a medical device.

The system presented in this thesis images tissue in the visible part of the electromagnetic spectrum and does so by acquiring spectroscopic data, more specifically hyperspectral datasets. This means the system is capable of creating a spectral cube of images (spatial and spectral dimensions) of the brain taken over several separate wavelength ranges, in order to capture the autofluorescence signature of brain tissue. The system design was done to ensure adaptation to one of multiple stereovision ports of a commercial clinical neurosurgical microscope also allowing the development of hardware and software for 3D reconstructions of the brain cavity. Although the fluorescence and 3D surface information were not used together as part of this thesis, their combination is essential for the quantification of fluorescence based on hyperspectral data because surface curvature is one of the factors that affect how light reflects off of biological tissue [30]. Approaches to use the 3D surface profile to correct the fluorescence intensity map of the tissue surface were developed elsewhere [22], [30] and are the subject of other projects in the Laboratory of Radiological Optics (LRO).

In summary, although the methods developed in the context of this project are applicable to other medical applications, the scope of this project is limited to do 3D reconstructions and to detect fluorescence through a microscope for neurosurgery.

1.2 Objectives and summary of technology developments

The main objective of this project is to develop a spectroscopic imaging system that allows generating the 3D shape of the cerebral cavity during surgery and to detect tissue autofluorescence through a neurosurgical microscope with minimal alteration to the standard surgical procedure for brain tumor resection. The system is versatile and it can be connected to one of the free stereovision ports of at least two different Carl Zeiss microscopes: the OPMI Pentero 900 used during neurosurgeries at the Montreal Neurological Institute and Hospital (Neuro) and the NC-4 model used for laboratory tests at the LRO, where most of the experimental work is carried out.

The different components of the system are fully controlled by a computer using a custom user interface. The interface allows the user to manipulate different image acquisition parameters and to control the projection of structured light (patterns of light specified by the user) onto the tissue, in addition to the visualization and registration of the images. Optical and mechanical design software is used to model every hardware component in order to build the system in the most optimal way.

Next, each mechanical and optical component are purchased, assembled and characterized to perform laboratory tests on tissue-simulating phantoms specially designed to quantify system performance in preparation for eventual clinical use. Then, the system is used for *in vivo* imaging of brain cancer in human patients at the Neuro. Finally, algorithms for spectral-spatial calibration of hyperspectral data and subsequent image analysis are developed to perform 3D reconstructions of tissue surface and recover autofluorescence.

1.3 Overview of thesis

This thesis reports on the work carried out as part of a PhD in Biomedical Engineering at the Laboratory of Radiological Optics at Polytechnique Montreal, under the direction of Professor Frederic Leblond (Department of Engineering Physics).

Following this introductory chapter, chapter 2 includes a review of literature presenting the main theoretical concepts necessary to understand the project. This includes a description of basic principles behind surface profilometry and a presentation of different profilometry methods with advantages and disadvantages. A review is provided relating to the use of profilometry in medical applications. For autofluorescence, the basic principles are presented together with an introduction to light propagation in tissue and a description of exogenous and endogenous fluorescence in clinical applications. Then, an overview is given of the current technologies for fluorescence-guided surgery, along with the key elements that fluorescence imaging systems require to detect fluorescence in the operating room.

The system design is presented in chapter 3. The technical characteristics of the optical and mechanical design of the new imaging system are described here, followed by the explanation of how the image acquisition software was programmed.

Chapter 4 explains the algorithms implemented to perform profilometry as well as each experiment that was planned to test the ability of the instrument to create three-dimensional images of structures through the neurosurgical microscope. The results for each profilometry experiment are also set out in this chapter.

Next, chapter 5 describes in detail each of the experiments carried out and the image analysis algorithms that were developed and tested to detect autofluorescence through the neurosurgical microscope. In addition, lab and clinical results are presented, the latter obtained during brain cancer surgeries.

Finally, in chapter 6 we find a critical discussion of the results obtained with the imaging system developed during this PhD. To conclude, this chapter presents the limitations of the system, possible improvements and future applications.

CHAPTER 2 REVIEW OF LITERATURE

2.1 Profilometry

2.1.1 Basic principles

3D reconstruction is the process of creating the 3D shape of an object. This process can be divided into two categories depending on the nature of the information used to retrieve heights pixel-by-pixel: (a) passive and (b) active methods [31].

Stereovision is considered a passive method, because in order to create three-dimensional images, it only needs 2D images taken by two cameras (stereo pair) placed at different viewpoints [32], [33]. 3D information is obtained from the difference or disparity (measure of the displacement of a point of interest) between the pair of images [34].

On the other hand, active methods are based on the projection of structured light (usually fringe patterns) onto a surface [31]. The fringe pattern will be deformed by the geometry of the object when it is seen from an angle that is different than that associated with the line-of-sight between the light source and the surface. The information pertaining to the shape of the object can be retrieved from the distorted light pattern [35].

2.1.2 Profilometry techniques

2.1.2.1 Passive methods: the two camera case

To perform a 3D reconstruction of an object using the passive method, one needs to first identify pixels with similar characteristics in two images of the same object acquired from cameras seeing the object from different angles. This process is called image matching [32], [36]. To simplify this task, a rectification method is applied. Rectification is the repositioning of stereo images in the same image plane, parallel to a baseline, as shown in Figure 2-1. The figure also shows that a baseline is the distance between the optical centers (point of intersection of light rays to form an image) of the two cameras [37]. This facilitates image matching because now the images have a common image plane [32] and pixel-to-pixel matching is done in just one dimension [38] given

that both pixels have, at this point, the same vertical (*y*-axis) location, as it is also shown in Figure 2-1.

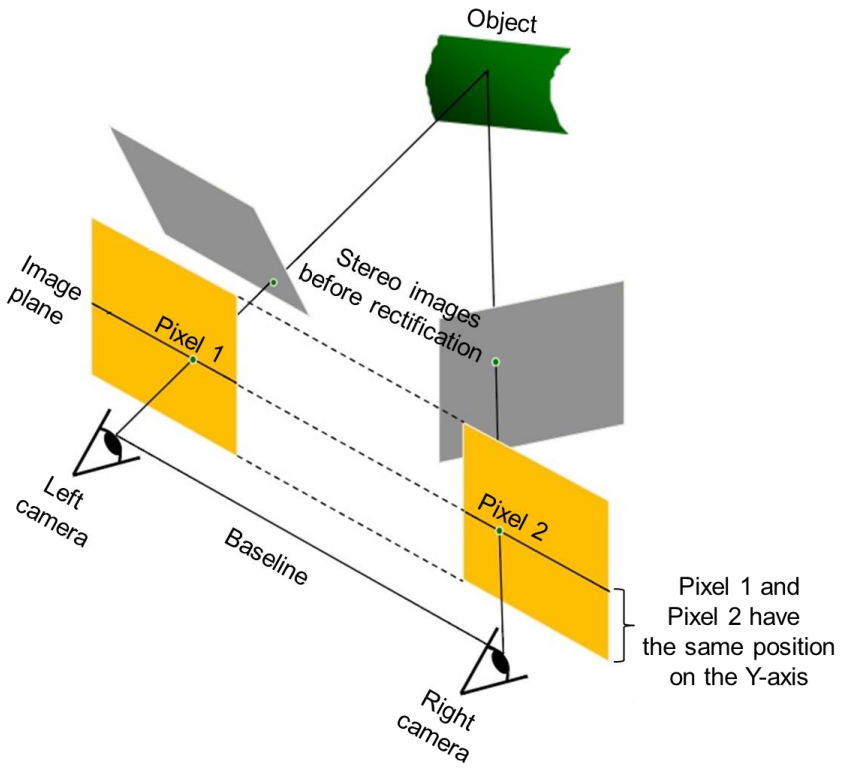

Figure 2-1: In the rectification process, there is a rearrangement in position to place the two images on the same image plane that is parallel to the baseline [39].

3D reconstruction can be carried out by the triangulation method once rectification of the stereo pair and image matching have been done [32], [40]. As shown in Figure 2-2, to implement the triangulation technique, suppose that two images are captured by two cameras (C_L and C_R) with optical centers parallel to each other. The two cameras have the same focal length (f) that corresponds to the distance from the camera lens to the focus point on the camera sensor; and the two cameras are separated from each other by a baseline (b, distance between the two cameras). The two pixels (p_L and p_R) of the cameras that capture the same 3D point of an object (P) are aligned with each other; this means that same pixel rows in the two stereo images capture the same object details. Taking into account that each pixel has coordinates x (x_L and x_R) on a camera

sensor, and that the object is located at a horizontal distance (X) from the left camera, one can calculate the depth or vertical distance (Z) from the object to the location of the cameras by forming similar triangles [37]. From the triangles, we obtain:

$$\frac{x_L}{f} = \frac{X}{Z} \quad \text{and} \quad \frac{x_R}{f} = \frac{X+b}{Z} \quad . \tag{2-1}$$

Then, the disparity ($d = x_R - x_L$) between the two pixels is inversely proportional to depth [37]. If the disparity is calculated pixel-to-pixel between the two images, one can create a disparity map that contains information about the depth of each pixel.

$$d = x_R - x_L = \frac{fb}{Z} \tag{2-2}$$

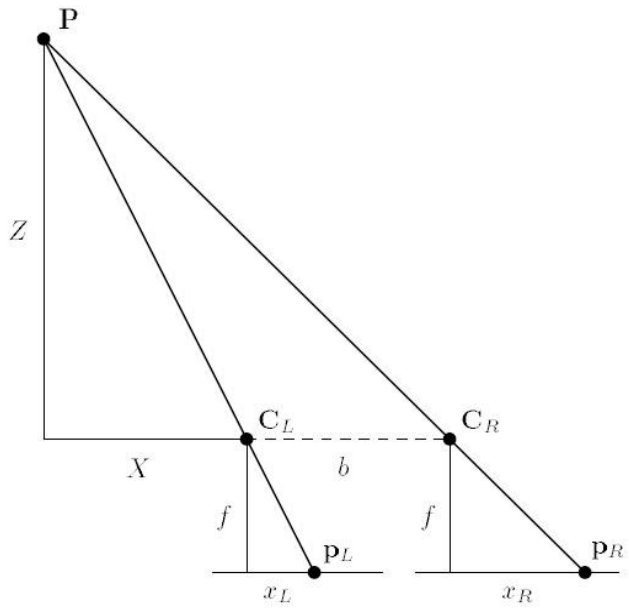

Figure 2-2: The triangulation principle using two cameras consists in defining the depth (Z) of a point (P) by forming similar triangles [37]. The change in the pixel location between the two images ($d = x_R - x_L$) is in inverse proportion to Z.

2.1.2.2 Active methods: structured light

As mentioned before, image matching consists in finding a pixel in the two images from different cameras that capture the same object's surface detail. This, however, is a challenge [31] because based on pixel characteristics (such as texture features and intensity) one pixel can match many other pixels [41]. The active method uses a projector to project structured light onto a sample and a camera takes an image from an angle to recover 3D-depth without having to form matching pairs. The structured light pattern with sine-shaped intensity gradients is deformed by the geometry of the sample due to the angle between camera and projector. The deformation of the light pattern due to the shape of the object is represented by a change in the phase of the sine wave intensity profile. Thus, the phase of the sine wave contains information of the height of the object. Next, the phase is computed for each pixel using the arctangent function, and this value is proportional to the surface height at an individual measurement point [35].

2.1.2.3 Four step phase-shifting profilometry algorithm

For this project, it was decided to implement the structured light method and a profilometry algorithm based on the projection of sine-wave patterns with four phase shifts instead of three. This method is called *four step phase-shifting profilometry algorithm* [138]. Even though a 3D image can be created from the projection of only three images, in practice more images need to be acquired, *i.e.*, three more reference images on a flat reference surface [139]. The *four step phase-shifting profilometry algorithm* is less error-prone than the profilometry algorithm with three phase shifts since the averaging of four images instead of three helps to reduce noise in the 3D maps [139]. As a result, with this algorithm it is not necessary to acquire, for each reconstruction, reference images on a flat surface. This is expected to facilitate use in an operating room environment where it is impractical to take reference images as it is critical not to interrupt the flow of the surgery and to maintain a sterile surgical field.

To reconstruct a surface, four sinusoidal-intensity fringe patterns with relative $\pi/2$ radians phase shifts are projected on a surface. The resulting deformed patterns that are detected can be modeled with the following equations:

$$I_1(x,y) = I_a + I_b \cos(\phi(x,y)) \tag{2-3}$$

$$I_2(x,y) = I_a - I_b \sin(\phi(x,y)) \tag{2-4}$$

$$I_3(x,y) = I_a - I_b \cos(\phi(x,y)) \tag{2-5}$$

$$I_4(x,y) = I_a + I_b \sin(\phi(x,y)) \tag{2-6}$$

where I_1, I_2, I_3 and I_4 are the light intensities for pixel locations x and y associated with the different phase shifts: 0, π/2, π, -π/2. I_a is a constant term or mean intensity for the four fringe patterns and I_b is half of the peak-to-peak amplitude of the sinusoidal fringes of the four patterns with phase ϕ. The terms I_a and I_b are illustrated in Figure 2-3.

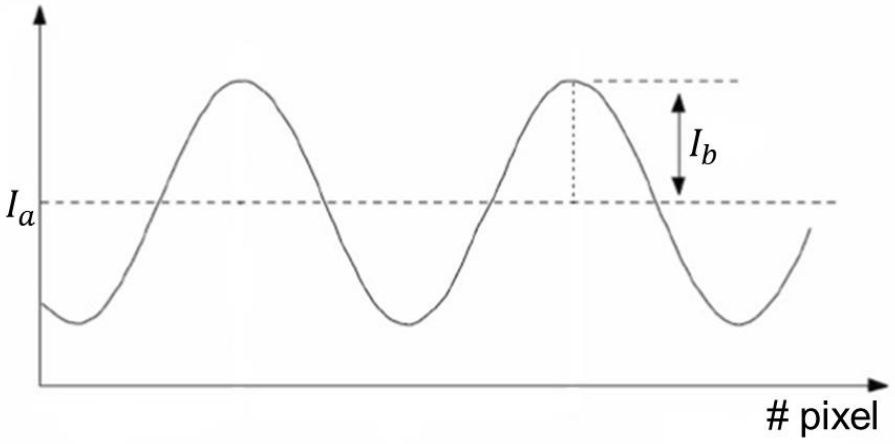

Figure 2-3: I_a denotes the mean intensity value of a sine wave and I_b the peak-valley half intensity. The axis labeled "# pixel" corresponds to the x-axis.

The simplification (obtained based on Eqs. 2-3 to 2-6) shown in Eq. (2-7) relate the phase (ϕ) at each pixel with the intensity of each of the four images. However, even if the phase can take any real value, it is limited to a 2π interval (between -π and +π) when the arctangent function is used to calculate it. One must then apply a phase unwrapping algorithm by means of which multiples of 2π are added to the phase in order to reconstruct the continuous phase that is not constrained between -π and +π [138]. For this project, the phase information was recovered after running a 2D phase unwrapping function in Matlab presented by Gdeisat et al. [140].

$$\tan\big(\phi(x,y)\big) = \frac{I_4(x,y) - I_2(x,y)}{I_1(x,y) - I_3(x,y)} \tag{2-7}$$

In order to convert pixels detected on the camera sensor to centimeters, the size of the projected pattern is measured accurately with a ruler along the *x*-axis to obtain an individual conversion factor (k_x). Then, knowing the total length of the illuminated region along the *x*-axis (L_x), it is possible to determine the length of each projected oscillation in centimeters (p):

$$p = \frac{(k_x L_x)}{\omega} \tag{2-8}$$

where ω is an integer representing the number of fringes.

Then, the height (h) is determined by multiplying the phase (ϕ) by the variable p and by a scaling factor (c) that is found with a calibration unit of known depth dimensions, like a step:

$$h = \phi c p \text{ [cm]} \tag{2-9}$$

2.1.2.4 Advantages and disadvantages of reconstruction methods

The advantage of the structured light method over the two camera approach is that in structured light one of the two cameras is replaced by a projector. Therefore, it's not necessary to create matching pairs like with the two camera technique. Matching pairs of images can be challenging and computationally demanding. However, the difficulty of structured light is interpreting the pattern under difficult photometric conditions, *i.e.*, when projecting a pattern with low illuminating power [31].

Additionally, with a single structured light setup, other structured light techniques can be implemented, for example, modulated imaging [42] to calculate the optical properties of biological tissue. Indeed, it has been published that the projection of structured light with a single instrument serves two purposes: 3D reconstruction of tissue structures and retrieval of its optical properties [30]. The imaging system developed in this thesis also aims to be able to provide information on the tissue optical properties; such functionality will be addressed by another research project at the LRO.

2.1.3 Profilometry in clinical applications

In the past, some profilometry systems have been developed for clinical applications, for example, to 3D reconstruct facial gestures to relate them with signs of diseases, such as facial paralysis [43]–[45]; also to capture the movement of the heart in order to have a better understanding of problems with heart prostheses and the functioning of heart valves [46]. Moreover, 3D reconstruction techniques have also been applied to 3D endoscopy to measure cavities in biological organs [47] and in 3D otoscopy to perform quantitative measurements of the inflammation of the eardrum and thus detect middle ear disorders [48].

In addition, in the area of neurosurgery, a profilometry system has been reported in open spinal surgery to make an accurate registration between intraoperative images and the preoperative CT scan to achieve precise screw fixation for spinal fusion [49]. This system comprises two cameras mounted onto the stereovision port of a neurosurgical microscope. The same setup has been exploited to estimate brain deformation after dura opening taking as reference the preoperative MRI images [18]. The accuracy of this system is 2.21±0.31 mm in spinal surgeries [49] and 0.9–1.1 mm for the assessment of brain deformation [50]. To achieve 3D reconstructions, this setup employs the passive method where two cameras take an image of the same object from two different observation points; then, the same features in the two images are matched.

2.2 Tissue autofluorescence

2.2.1 Fluorescence properties

Luminescence is the process of emitting light when a molecule passes from a higher state of energy to a lower one. When a photon initiates the light emission process, this event is called photoluminescence. Fluorescence and phosphorescence are both in this category [51]; in both processes, a molecule is excited by incident radiation from an external light source that is absorbed by the sample [52]. The difference between fluorescence and phosphorescence lies in the timescale on which the emission occurs, being in the order of nanoseconds (ns) for fluorescence and much longer (> seconds) for phosphorescence [51]. On the contrary, when the

emission of light is triggered by a chemical reaction catalyzed by an enzyme, it is called bioluminescence; this is a special quality of living organisms [53].

Fluorescent molecules (fluorophores) are characterized by excitation and emission spectra [54]. The excitation spectrum (also called extinction coefficient) represents the relative intensity of light that is absorbed by the fluorophore at each wavelength (usually expressed in nanometers (nm) or wavenumber shifts (cm^{-1}) with respect to the excitation wavelength) [55]. The unit of measure for the excitation spectrum at a given wavelength is $cm^{-1}\ M^{-1}$, where the molarity, M, is the number of moles per liter of a fluorescent solution. The emission spectrum is independent of the excitation wavelength and represents the fluorescence intensity as a function of wavelength. In addition, the Stokes shift is the separation in frequency between the maximum point of the excitation and emission spectra of a fluorophore [54]; a small Stokes shift means that the excitation and emission occur at frequencies close to each other.

Fluorescent molecules are also characterized by their quantum efficiency (between 0 and 1), which is a measure of the relative fraction of photons absorbed by a molecule that induces fluorescence events instead of, *e.g.*, being transformed into heat or reemitted as light through elastic or inelastic scattering [54]. Another property of fluorophores is photobleaching which is the irreversible process leading to conformational molecular changes rendering the molecules non-fluorescent after being repeatedly excited [56]. Finally, a fluorescent substance is also characterized by its lifetime. The lifetime of a fluorophore is the average time that the molecule remains in an excited state. This time scale is usually of the order of nanoseconds for both organic and inorganic fluorophores [54].

2.2.2 Light propagation in biological tissue

A number of interactions occur when light enters and propagates through biological tissue, as the composition of tissue is heterogeneous with a range of different optical properties within its volume [57], [58]. Light can be either directly reflected from the surface of the sample or it can be absorbed or scattered, as illustrated in Figure 2-4. The optical properties of the tissue are generally described by the refraction index, the absorption and scattering coefficients [59].

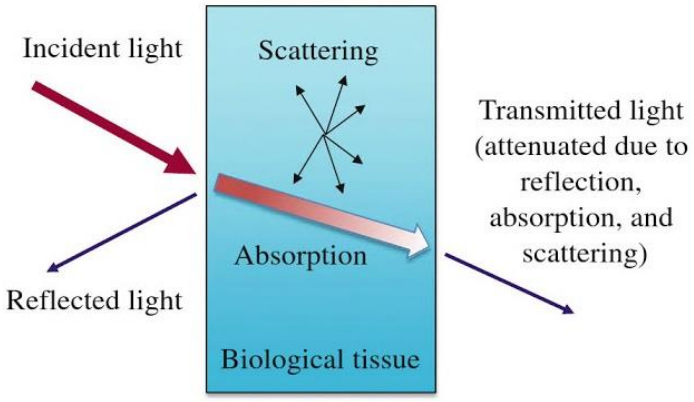

Figure 2-4: Schematics showing different light-tissue interaction mechanisms [59].

Scattering occurs because of changes in the refractive index of tissue [58] caused by heterogeneities associated with varying density and size of cells, organelles as well as properties of the extra-cellular matrix [59], [60]. Scattering can be either elastic or inelastic. During elastic scattering, the scattered photons keep the same energy as that of the incident photon as observed in the case of Rayleigh scattering. In inelastic scattering, such as Raman scattering, the photons interact with the vibrational modes of the molecules resulting in a loss of energy for the reemitted photons [59]. At the cellular level, the most important scatterers are the subcellular organelles, *e.g.*, mitochondria [61].

Light penetration depth in biological tissue depends on the relative amount of light being absorbed or diffused by the tissue. The absorption of light by the tissue depends on its molecular composition, *i.e.*, on the concentration of the main tissue absorbers usually referred to as chromophores. In the visible spectrum (390-700 nm), the most important chromophores are blood (oxy- and deoxyhemoglobin) and melanin, with absorption coefficients generally decreasing as the wavelength increases, as shown in Figure 2-5. Ultraviolet (UV, < 390 nm) absorbers are mainly proteins and amino acids, and in the infrared (IR) region, water is the dominant absorber [62]. Water absorbs light weakly in the visible and becomes increasingly important as the wavelength increases in the near-infrared (NIR) region of the electromagnetic spectrum that lies from 700 to 1200 nm. Water absorption becomes dominant at mid-infrared wavelengths (maximum at 2940 nm) [63].

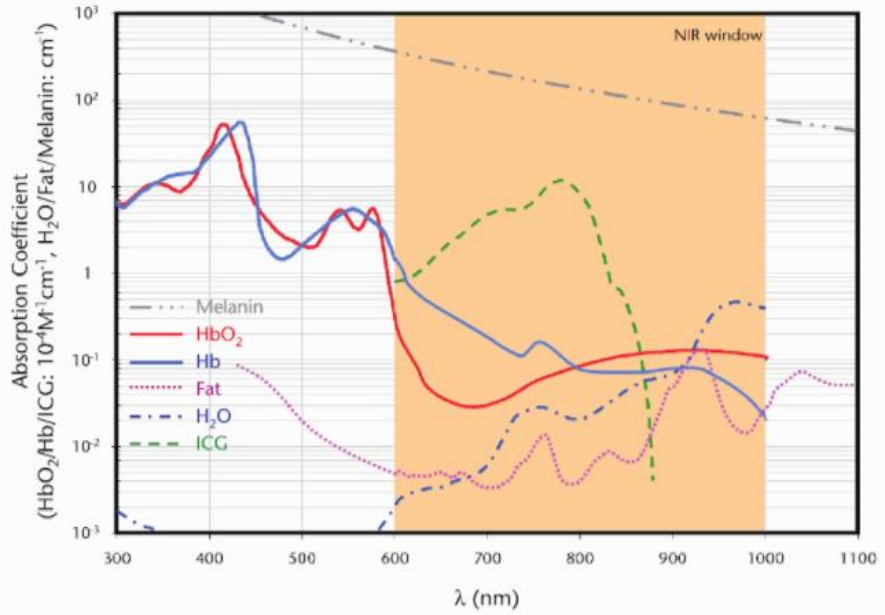

Figure 2-5: Absorption spectrum of main chromophores in tissue along a broad range of wavelengths [64].

In the brain and also for most types of tissues, the most important chromophores are oxy- and deoxyhemoglobin [65]. Within the so-called therapeutic window (600-1300 nm), there is low absorption in most tissues, because hemoglobin absorption (either oxy or deoxy) decreases by several orders of magnitude from blue to red and into the NIR, as it is shown in Figure 2-5. The region where blood absorbs the least light is above 600 nm, allowing greater effective light penetration depth. In that region, scattering dominates over absorption and light becomes mostly diffuse [58]. The light absorbed by the tissue can be dissipated as heat, it can be emitted in the form of fluorescence or it can be of use in photochemical reactions [58]–[60], [66]. Each molecular process is associated with a different quantum mechanical interaction probability, with, *e.g.*, selective absorption typically being several orders of magnitude more probable than fluorescence.

This emission of light at the same wavelength as tissue excitation is known as diffuse reflectance [61]. The reflectance signal represents a weighted average of the light having traveled at different depths and, consequently, it is an average measurement of the tissue properties within a specific volume. Diffuse reflectance provides information relating with both tissue scattering

and absorption; and alterations in tissue morphology and functional status (size and shape, concentration and oxygenation status of blood) can be used as a surrogate marker to differentiate tissue types, *e.g.*, normal *vs.* cancer tissue [67]. For example, as cancer progresses, angiogenesis (formation of new blood vessels [68]) and tissue hypoxia (low oxygen in tissue [69]) affect the concentration of oxy- and deoxyhemoglobin, which in turns affect absorption; thus, optical measurement of hemoglobin through diffuse reflectance images can be also used as a surrogate measure of, *e.g.*, angiogenesis and hypoxia. Consequently, reflectance images can detect local changes of tissue absorption and scattering; whereas, when tissues are in disease states, such as cancer, they have different biochemical composition than healthy tissues (changes in the structure of lipids, fatty acids, carbohydrates and proteins) and also altered metabolism levels [70], which results in a different fluorescence spectrum [58]. Therefore, fluorescence signals can detect changes in the biochemical composition of tissue [71].

2.2.3 Endogenous and exogenous fluorescence

In general, fluorescence techniques for the detection of brain tumors can be separated into: (a) intrinsic fluorescence (autofluorescence); and, (b) exogenous fluorescent agents targeting specific cellular processes suitable for human use, *e.g.*, the ALA-PpIX system whereby injection of the ALA molecule triggers the preferential accumulation of the fluorescent molecule PpIX in some tumor types including glioblastoma and meningioma [72].

The fluorescence associated with endogenous tissue fluorophores is called autofluorescence [61]. In brain tissue, endogenous fluorescence is mainly due to concentrations of molecules that are involved in cell metabolism, *e.g.*, reduced nicotinamide adenine dinucleotide (NADH) [73], lipopigments [4] and flavin adenine dinucleotide (FAD) [74].

Intrinsic fluorophores are generally excited in the wavelength range including blue and UV light where light penetration is low due to the large absorption to elastic scattering ratio. The wavelength at 375 nm, for instance, can be used to efficiently excite NADH and FAD due to their high absorption at this wavelength. In addition, the wavelength at 405 nm is useful to excite NADH, FAD and other sources of endogenous fluorescence in the brain including lipopigments, porphyrins and chlorins [4]. Despite the fact that at these excitation wavelengths autofluorescence only provides information for superficial tissue layers, fluorescence is generated without the

administration of any chemical compound, thus avoiding potential medical complications or side effects, and allowing researchers to by-pass the complexity associated with regulatory approvals for new drugs [72].

By measuring the autofluorescence spectrum, one can obtain the emission intensities of brain tissue fluorophores as well as information relating with their relative concentration allowing, *e.g.*, to calculate metrics as the oxidation-reduction states, which can be useful for cancer detection [75]. However, an important difficulty in autofluorescence detection for *in vivo* brain tissue is the absorption associated with large concentrations of hemoglobin. Another challenge – when compared to using exogenous targeted markers – is that autofluorescence levels are typically much lower, namely up to 3-4 orders of magnitude in the case of the ALA-PpIX system for gliomas [51]. As a result, recovering autofluorescence signals require more sensitive light detection systems and typically longer integration times than with exogenous agents, hindering the prompt delivery of information during neurosurgery [72]. Moreover, the emission of light from biomolecules present in a variety of tumors still needs to be studied through experiments in clinical research [51], [76]. Furthermore, surprisingly, there are not enough results of human tissue autofluorescence [77], [78]; in contrast, autofluorescence in rats, mice, pigs and kidney tissue is well reported in the literature [79], [80].

Alternatively, fluorescence contrast to identify specific cells *in vivo* can also be produced by exogenous fluorescent molecules that are administrated to the patient. Even though exogenous markers are often easier to detect because they have distinctive emission peaks, a key design feature for exogenous fluorescent molecules that can be very challenging is their specificity to associate with diseased cells [65], [81]. When there is no specificity of association, the contrast in the image provided by a fluorophore doesn't give useful information for identifying unhealthy tissue [81].

Finally, the accuracy of fluorescence imaging systems to detect cancer can be improved by quantifying fluorophore concentration, and this could promote the use of these instruments for the early detection of cancer [51]. This process consists of correcting the attenuation of the fluorescence signal by the different layers of tissue, the effect of light scattering and the absorption of blood to make the signal specific to concentration of fluorescent markers. Within this context, since the autofluorescence spectrum is composed of a superposition of multiple

fluorescent molecules, it is very difficult to interpret [72], and its quantification is harder than for exogenous fluorescent agents.

2.2.4 5-aminolevulinic acid-induced protoporphyrin IX

Several studies have shown that the oral or intravenous administration of 5-aminolevulenic acid (5-ALA) leads tumor tissue to accumulate higher levels of the fluorophore Protoporphyrin IX (PpIX) when compared to normal adjacent tissue [5], [82]–[85]. In addition, a multicenter Phase III clinical trial showed that PpIX helped to remove brain cancer more completely [5] and it has been demonstrated as a tool for identifying tumor boundaries [12]. However, although PpIX has apparently good sensitivity, its lack of tumor specificity has limited its general adoption in surgery, because there is evidence that PpIX also accumulates in other types of abnormal as well as normal tissue [25], [86], [87]. In addition, the main emission peak of PpIX occurs in the visible region and therefore its signal has a contribution from tissue autofluorescence [88]. Figure 2-6 shows the excitation and emission spectra of PpIX of a sample of cancerous tissue.

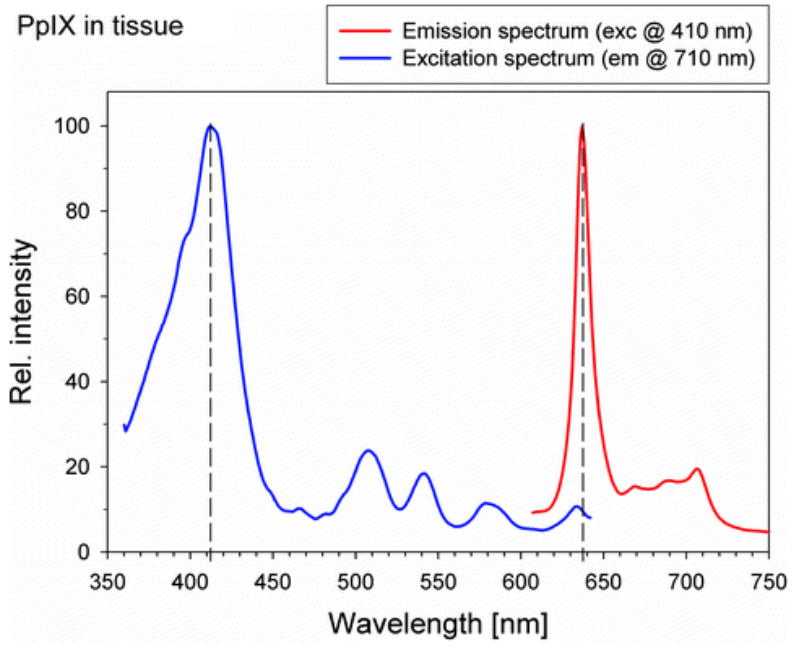

Figure 2-6: PpIX spectra of human glioblastoma tissue. The PpIX excitation maximum is shown in blue at 410 nm and the main emission peak appears in red at 635 nm with a smaller bump at 710 nm [89].

2.2.5 Fluorescence detection during neurosurgery

The pioneers of fluorescence neurosurgery were Japanese and German neurosurgeons, exploiting capabilities of fluorophores such as PpIX [12], together with research laboratories that worked in the conception of fluorescence-guided surgery systems [88]. Fluorescence produced through biochemical compounds can be monitored during neurosurgeries by: (a) spectroscopic probes that perform single point measurements; (b) modified surgical microscopes or independent systems developed in research laboratories [12].

2.2.5.1 Neurosurgical probes to allow point-by-point autofluorescence detection

Ideally, in neurosurgery applications it is preferable to have microscopy instruments that avoid directly contact with the tissue; however, probes that provide point measurements have a higher sensitivity to light detection since they can capture more light [90]. The depth of sampling [91], the volume of tissue to be analyzed [92] and the spatial resolution are determined by the design of the optical fiber probe [72]. To be able to quantify information, *i.e.*, the tissue optical properties, some probes have been designed limiting their size to less than a scattering distance; while other designs take measurements at different wavelengths to eliminate the background signal from the tissue [93], [94].

Until now, perhaps, the most complete *in vivo* research study for the observation of tumors by means of autofluorescence also includes white light reflectance measurements by a spectroscopic probe that was used during surgery in 26 patients [95]–[97]. The procedure consisted in recording the background signal from the environment, followed by the acquisition of the emission spectrum of tissue autofluorescence with excitation at 337 nm, and the white light diffuse reflectance signal was also acquired along with biopsies in the region of interest for which histopathology analysis were performed. The analysis of the information was made post-operatively, and the fluorescence and reflectance spectra were evaluated separately. The purpose of the study was to distinguish the boundaries of infiltrated tumor into healthy tissue (100% sensitivity; 76% specificity) and to detect also high-grade tumors (sensitivity and specificity of 80% and 89%, respectively) and low-grade gliomas (sensitivity and specificity of 94% and 93%, respectively).

On the other hand, in [4] a probe was also employed for the interrogation of different types of tumors: glioblastoma, meningioma and diffuse glioma, in addition to central nervous system metastasis and epileptic tissue. Autofluorescence spectra were acquired in these tissues using excitation sources at 405 and 375 nm with the objective of calculating the ratio between the emission intensity of different molecules in order to know the metabolic reaction [98]–[100] and associate it with cancer.

As mentioned before, the brain tissue is composed of many fluorescent molecules, including: NADH [101], FAD [102], porphyrins [103], [104], lipopigments, and chlorins [4]. In [4] and [73], the contribution of each fluorophore in the emitted signal from brain tissue was estimated using a least-square approach whereby detected spectra were projected on a basis spectra associated with the individual tissue fluorophores:

$$S_t(\lambda) = \sum_{i=1}(f_i S_i(\lambda)) \tag{2-10}$$

where:

$S_t(\lambda)$: the whole measured spectrum

i: fluorophore index (i = 1 to N, with N the number of fluorophores considered in the analysis)

$S_i(\lambda)$: individual emission spectrum of each fluorophore

f_i: the factor weighting the relative contribution of each fluorophore

Figure 2-7 (right) shows that for excitation at 405 nm, five main fluorophores can be considered in the autofluorescence signal of brain tissue: NADH, flavin, lipopigments, porphyrins and chlorins. Alternatively, for excitation at 375 nm, the two primary contributions to the autofluorescence spectrum of brain tissue are NADH and flavin. However, in the total spectrum, the emission of flavin is less than 5% the emission of NADH. Therefore, for an excitation of 375 nm, most of the spectrum corresponds to NADH [73], as it can be seen in Figure 2.7 (left).

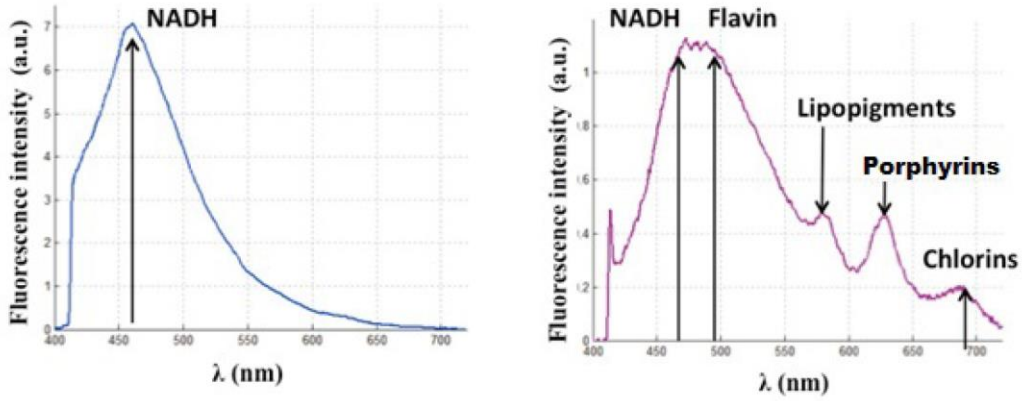

Figure 2-7: Molecules that emit fluorescence in brain tissue when they are excited at 375 nm (left) and 405 nm (right) [73].

When calculating the integral under the curve of the emission spectrum of NADH, FAD and porphyrins**,** two different ratios can be obtained [98], [104]: (a) the reduction-oxidation (redox) ratio (*ROx*), and (b) the optical index ratio (*OIR*). The *ROx* can be calculated considering the fluorescence emission of FAD and NADH [4], [105]:

$$ROx = \frac{I_{FAD} - I_{NADH}}{I_{FAD} + I_{NADH}} \tag{2-11}$$

where:

I_{FAD}: the area under the curve of FAD emission

$I_{NADH:}$ the area under the curve of NADH emission

The *OIR* can be obtained with the emission of NADH and porphyrins [4]:

$$OIR = \frac{I_{NADH}}{I_{Por}} \tag{2-12}$$

where:

I_{Por}: integral under the porphyrin emission

As part of the results published by Poulon et al. in [4], healthy tissue (control) has significantly higher fluorescence intensity than tumor at excitation wavelengths of 375 and 405 nm (Figure 2-8). This can be explained due to a lower absorption in healthy tissue (tumors have greater vascularization than normal tissue) which consequently results in an apparently more intense fluorescence [106]. Moreover, in the same study Poulon et al. [4] reported that healthy tissue had higher *ROx* when compared to tumor tissue ($p < 0.001$). Finally, the *OIR* also showed a marked difference between tumor and healthy tissue ($p < 0.001$).

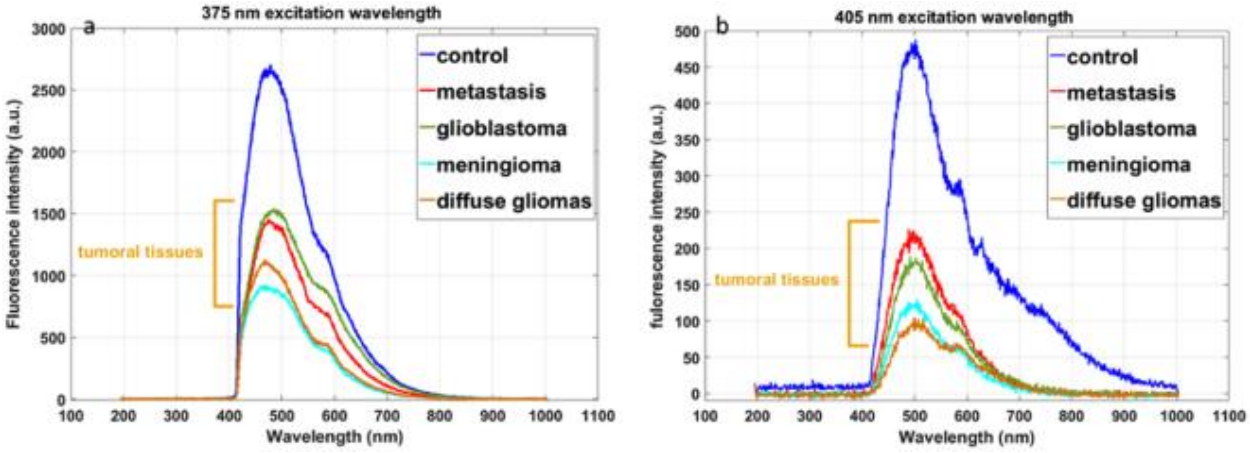

Figure 2-8: Fluorescence of different types of tumor and of control tissue (epileptic) with excitation at 375 nm and 405 nm [4].

In addition, the redox state of some coenzymes such as NADH and FAD makes them emitting different fluorescence intensities [100]. This value is influenced by the cell metabolism and the supply of oxygen to the cells [107]–[109]. The *ROx* changes inversely with changes in the metabolic rate, which means that as the *ROx* decreases the metabolic rate increases [99]**.** This can be useful to analyze if there is a significant alteration in the metabolism of tumor regions [110], [111]. Previously, it has been published that such differences in metabolism rates exist in normal and cancerous tissue [104] since tumors cause a reduction of collagen in tissue to expand through infiltration and metastasis [112]. Indeed, the calculation of *ROx* has helped before to differentiate healthy tissue from cancer [111], [113]–[115]**.**

Furthermore, in the past, some studies have also reported a porphyrin accumulation in tissue of mice with renal cancer [103], [116] and in humans with oral [117] and bladder cancer [104]**.** In addition to the increased levels of porphyrins in cancer, it was found that the *OIR* (NADH/porphyrins) also provides a statistically significant difference between healthy and cancerous bladder tissue [104], [118].

2.2.5.2 Modified surgical microscopes in fluorescence imaging

Contrary to single-point probes, fluorescence imaging systems can show spectral information pixel-by-pixel across a large field of view to identify the extent of the tumor [119]. Surgical microscopes currently available on the market are adapted to detect fluorescence by adding optical filters allowing surgeons to alternate between a white light mode – for the visualization of tissue structure – and fluorescence imaging following tissue excitation around a wavelength selected based on the excitation spectrum of the fluorophore of interest [88].

With the advent of ALA-PpIX as an effective contrast mechanism for high-grade glioma, the research group of Stummer et al. [120] used a surgical microscope that had a white xenon lamp from which blue light in the range 375-440 nm was filtered to excite PpIX during tumor resection procedures. By adding a longpass filter at 455 nm in the detection path, they were able to visualize the fluorescence of PpIX (emission at > 635 nm). Later, Leica also commercialized a microscope for the Phase III clinical trials of this research group; and now there are similar versions of this microscope on the market built not only by Leica, but also by Zeiss [72].

In the past, other hyperspectral systems have been made that can be connected directly to one of the side ports of a neurosurgical microscope [119], [121]. Reference [119] reported a hyperspectral imaging system that includes a LCTF (Liquid Crystal Tunable Filter) and a CCD (charge-coupled device) camera coupled to a Leica Wild Heerbrugg M690 neuromicroscope. In that system, fluorescence excitation was at 340 nm and diffuse reflectance illumination was provided by a xenon lamp with customized excitation optics placed at the microscope head. Fluorescence and white light reflectance emissions were recorded from 400 to 720 nm. An empirical algorithm was developed to distinguish between normal and tumor tissues. The formula considered that diffuse reflectance varies inversely with hemoglobin absorption, thus the maximum diffuse reflectance intensity is around 700 nm. The wavelength at which there is the

maximum emitted fluorescence intensity from the tissue is next identified on the emission spectrum, and finally the ratio of fluorescence and diffuse reflectance at those specific wavelengths provided a threshold value to identify tumor tissue.

On the other hand, new imaging systems must have the ability to quantify fluorescence *in situ*. The concentration of a fluorophore within the tissue can vary widely by several orders of magnitude depending on how it is distributed and how it is associated with different biomarkers of disease. Quantification of fluorophore concentrations helps to compare information between different research centers and to track results on the evolution of a patient over time and also within groups of patients [88].

A PpIX fluorescence quantification system integrated to a surgical microscope was presented by Valdes et al. [24]. This system acquires spectral images of the fluorescence emission (600-720 nm) and white light reflectance (450-720 nm) to produce pixel-by-pixel quantitative fluorescence images using a LCTF and a CMOS (complementary metal-oxide semiconductor) camera attached to the side port of a Zeiss OPMI neurosurgical microscope. The microscope is equipped with a blue source (400-410 nm) and a broadband xenon lamp [122]. In order to quantify PpIX fluorescence, the system employs an empirical algorithm that takes into account the wavelengths at which tissue would absorb more light (excitation wavelengths) and wavelengths at which it is expected that light scattering affects more the fluorescence signal (emission wavelengths). The raw fluorescence signal is then divided by the multiplication of absorption and scattering factors contained in the white light reflectance signal.

2.2.6 Instrumentation of a fluorescence imaging system

The basic components of a fluorescence imaging system are: (a) an excitation source adapted to excite the fluorophores of interest; (b) suitable lenses and filters for light detection; and (c) a camera. Each of these components is now described along with specific requirements for fluorescence imaging:

(a) Excitation light source

To choose an excitation source, one must consider mainly the spectral bandwidth, the solid angle of the beam and the output efficiency. Among the possible excitation source technologies we

find: (a) gas lamps with a wide bandwidth filtered for specific wavelengths; (b) lasers; and, (c) light-emitting diodes (LEDs). To choose an excitation source it is important: (i) to be able to block the excitation light source from reaching the camera sensor, (ii) that the illumination covers the required field of view (FOV) with sufficient intensity, (iii) the possibility to integrate it onto the microscope, and (iv) the cost [88].

Among the illumination sources, the lamps have the lowest efficiency, the widest spectral bandwidth and the largest solid angle. A large part of the photons emitted by the lamps are blocked by the excitation filter and this can cause great heat dissipation. Therefore, they are not recommended for fluorescence. Nevertheless, surgical microscopes use these types of excitation sources [88].

The narrow spectral bandwidth of a laser makes it easier to filter the excitation light. New versions of high-power laser diodes can be useful to excite a fluorophore at very low concentration; however, the light exposure limits for skin and eyes must be verified and this can complicates regulatory approval for fluorescence systems. In addition, to increase the illumination area of a laser diode to cover the required FOV, it is necessary to use beam expanders. The temperature at which laser diodes operate must also be regulated and its current should be controlled in order to fix the output power and the shape of the spectrum; this requires additional hardware, which must be placed far away from the patient because of potential safety issues relating with electrical hazard [88].

Among the technical characteristics of LEDs, we find: high output power, high efficiency and low cost. It is becoming easier to produce high-power LEDs as demand increases on the consumer market. However, when illuminating with LEDs, it may be difficult to achieve illumination uniformity; though it is possible to have an array of multiple LEDs to overcome this drawback. On the other hand, one of the disadvantages of LEDs is that when fluorophores exhibit small Stokes shifts, it can happen that the excitation light is transmitted through the emission filter. In this case, it is advisable to use an excitation filter to limit the output of the light source. Finally, in the future, it is expected that there will be a growth in the use of LEDs for fluorescence imaging systems [88].

(b) Optical components for capturing fluorescence light

Among the technical characteristics for detection lenses (objective) in a fluorescence system we find: the size of the FOV, the depth of field, the f-number and the working distance [88]. The optical design of a system must be achieved by considering all these factors and ensuring they are adapted to the targeted clinical application.

It is also necessary to carefully select the emission filters that are integrated into the system to – as much as possible – block light that is not specific to the fluorescent molecules. To select a filter, one has to consider the excitation source spectrum, the ambient light and the Stokes shift of the fluorophore. When a fluorophore has absorption and emission spectra that are widely separated, such as PpIX, the selection of an emission filter is easier than when the absorption and emission spectra are very close to each other. Emission filters can be either longpass, bandpass or notch filters. The excitation light that passes through the emission filter (bleed-through), either because it leaks through the rejection band or because it has a large incidence angle, determines the noise floor of an apparatus and in consequence will affect its sensitivity to detect the fluorescent molecules of interest [88].

(c) Camera sensor

The dynamic range of a camera, its read-out-noise, its spatial resolution and gain are technical characteristics that establish its utility and optimal adaptation to a specific clinical application. A bit depth of at least 10-bit facilitates the quantification of a signal by capturing a signal that varies in concentrations by at least 2-3 orders of magnitude as long as there is relatively low background (dark) counts. CCD cameras are widely used as fluorescence detectors; when working at low temperatures, they can have low read-out noise; generally, they have high resolution and they can be found in 16-bit versions. Some cameras with more sensitivity are the electron multiplying charge-coupled device (EMCCD) and the intensified-CCD (ICCD). These can be very useful when the signal intensity is very low because of analog gains of more than 1000X, but the quality of the signal is easily degraded at high noise levels [88].

2.2.7 Required characteristics of a intraoperative fluorescence imaging system

One of the principal objectives of an intraoperative fluorescence imaging system is to capture low fluorescence signals. However, the light sensitivity of such a system is not the only factor

determining its utility in the operating room. Other characteristics to consider for practicality and ease of integration into the surgical workflow are: (a) ability to provide real-time overlay of fluorescence images (molecular information) and reflectance images (structural information); (b) *in situ* fluorophore quantification, *i.e.*, displaying fluorescence in a manner that provides information that specifically relates to the concentration of fluorescent molecules; (c) ergonomy and data acquisition/processing speed for minimal disruption of the procedural workflow, (d) ability to operate under normal ambient light conditions through, *e.g.*, the development of optical components preventing ambient light to reach the detectors or data processing tools that are decoupling fluorescence signal from ambient room lighting [88]. The above-mentioned features have been incorporated into the design of the intraoperative fluorescence imaging system developed in this thesis, and the development of each one of them will be discussed in section 5.1.

Operating room lights can become a problem when working with low concentrations of fluorophores; at this point, the dynamic range of the camera might be completely used up by background light, thus preventing the acquisition of a fluorescence signal component with sufficient levels of signal to noise ratio. Figure 2-9 shows a graph of the most common light sources in the operating room, such as tungsten and halogen lamps, fluorescent lights and LEDs. Halogen and tungsten lamps radiate substantial light in the range of 600 to 850 nm and can easily contribute to the detected fluorescence signal if working in the red or NIR region. The use of these lamps in the operating rooms has been decreasing recently, which is good for the use of fluorescence systems. Even ambient light at normal levels in the operating room affects the signal if the detected fluorescence is in the visible range, from 500 to 750 nm. In this case it is necessary to implement methods to suppress the background [88].

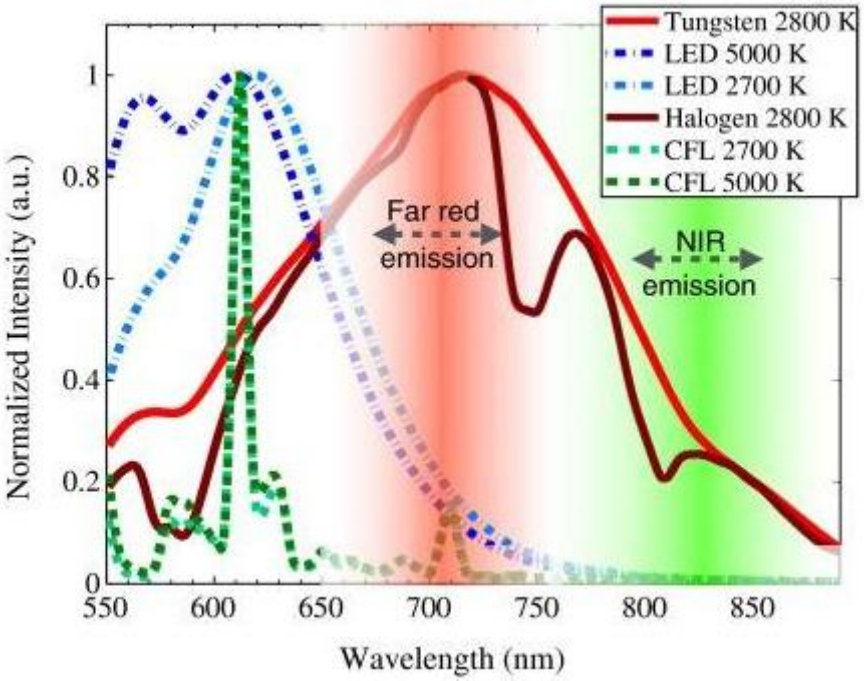

Figure 2-9: Typical light sources found in operating rooms: tungsten and halogen lamps, LEDs and fluorescent lights [88].

CHAPTER 3 SYSTEM DESIGN

An objective of this project was to design and build a hyperspectral imaging system that is seamlessly integrated to a neurosurgical microscope and that can be used to detect diffuse reflectance and intrinsic fluorescence tissue spectra over macroscopic scales (field of view > 1 cm and spatial resolution ~200 microns) as well as to acquire data that can be used to produce 3D brain surface reconstructions.

The flowchart in Figure 3-1 shows the organization of the project, which not only includes the development of the optical hardware but also the development of data calibration and processing techniques. Briefly, the main development steps realised in this thesis include:

(a) Designing and fabricating the necessary hardware components to project structured light patterns and obtain hyperspectral images through a neurosurgical microscope;

(b) Ensuring an effective user-friendly interface for automated data acquisition and calibration;

(c) Developing data processing techniques leading to 3D surface reconstructions of the brain cavity and detection of the autofluorescence signature of brain tissue.

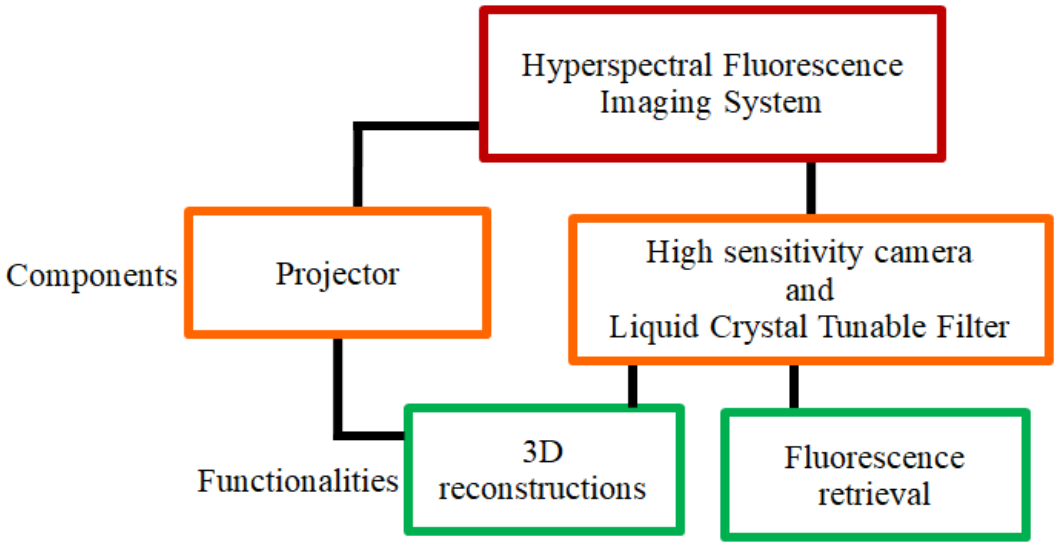

Figure 3-1: Chart presenting the different components and functions of the system that were developed as part of this PhD thesis.

3.1 Description of system components and overall functionalities

The human brain has the ability to perceive depth of objects as a result of the fusion of twin images of the same object seen by each eye. Each eye views the same object from a slightly different observation angle; this is called stereoscopic vision. Neurosurgery stereomicroscopes use this principle to provide depth perception to the surgeon. The images transmitted by the two eyepieces (left and right) are perceived from a viewpoint apart from each other by around 7 degrees [123]. On a neurosurgical microscope there are several (typically up to 5) optical ports, two of which are used during a procedure by the surgeon and sometimes an assistant. In this project, optical components were connected to free optical ports in order to provide new functionalities to the microscope.

Since each channel (optical port) of the surgical microscope operates as an independent optical path, the 3D profilometry functionality was developed by connecting the Digital Light Projector (DLP, Digital Light Innovations, TX, USA), and the fiberoptic bundle (Schott, Mainz, Germany) shown in Figure 3-2 to the right and left microscope oculars (eyepieces) of an optical port by means of custom optical adapters.

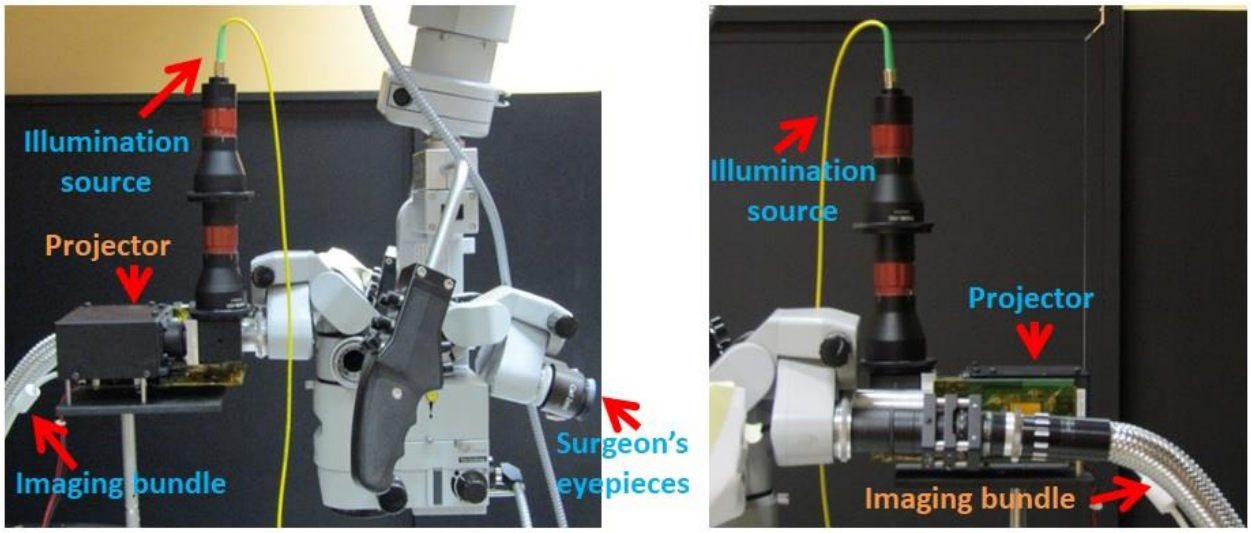

Figure 3-2: Two different side views of the optical system developed to perform 3D reconstruction of the brain surface through a neurosurgical microscope: a Digital Light Projector is coupled to a microscope ocular by means of an optical adapter and an imaging fiber optic bundle is connected to a different microscope ocular using a custom-made optical adapter.

The imaging bundle is to a certain extent flexible and can transfer an image from its distal end (microscope head) to its proximal end (a camera detection system), located up to several meters away. Specifically, the bundle is attached to a microscope ocular and it is made to travel all along the microscope arm up to the detection sub-assembly composed of a Liquid Crystal Tunable Filter (VariSpec LCTF, PerkinElmer, MA, United States) and a high sensitivity camera. The tunable filter can collect images at selected wavelengths in the range of 400-720 nm by means of bandpass filters with a full width at half maximum **(**FWHM) of 7 nm [124]. The LCTF is connected to the camera positioned outside of the sterile surgical field (Figure 3-3) and it is programmed to transmit specific spectral bands to the camera.

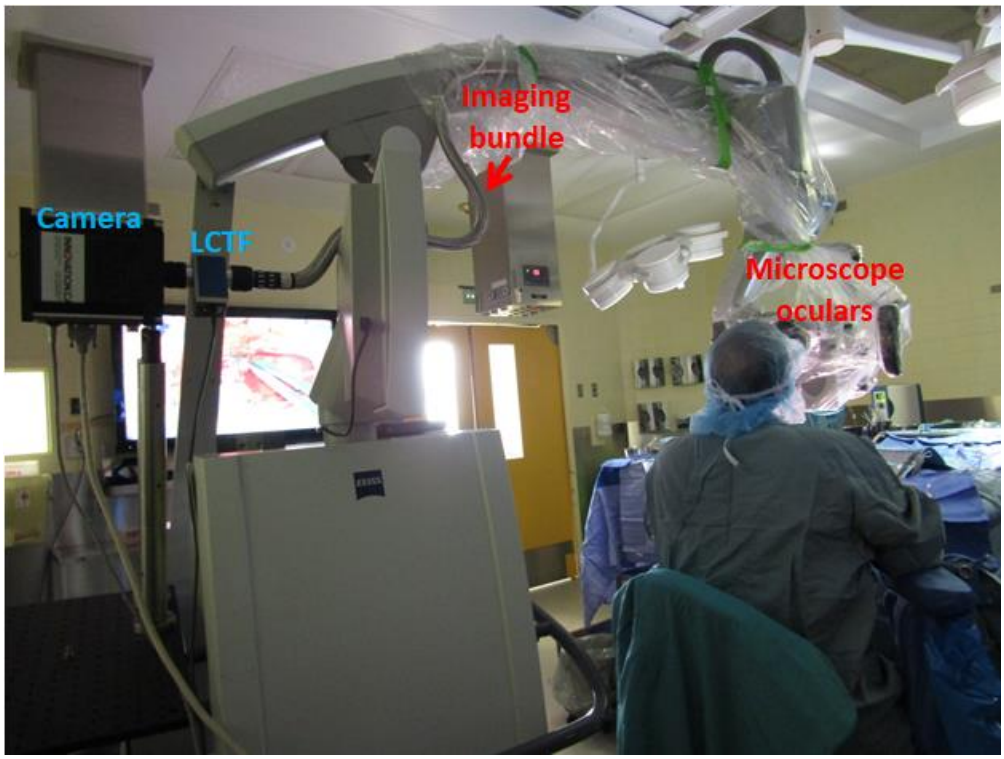

Figure 3-3: Imaging system used during a neurosurgical procedure. The LCTF is connected to a camera. The camera system is located at the proximal end of the bundle outside of the sterile surgical field.

In this thesis the system is used to provide the microscope with two new functionalities, namely: (a) 3D reconstruction of the brain surface, (b) detection of tissue autofluorescence. The tasks

listed below were carried out during this PhD towards the development and implementation of those two functions.

Functionality 1: Phase-shifting profilometry

(a) A new system was built to project light patterns of any shape and to acquire reflectance images through the surgical microscope using a highly sensitive camera that was connected to a neurosurgical microscope together with a coherent imaging bundle.

(b) A detailed study was conducted to optimize the optical coupling of the projection system with the microscope to maximize the light power density delivered to a sample within the microscope field of view.

(c) Data acquisition software was developed for automatic synchronization of structured light projection and image acquisition through the LCTF and the camera.

(d) An algorithm was developed to analyse structured light images and perform 3D surface reconstruction.

(e) The accuracy of the profilometry technique was evaluated using phantoms of known heights and tilt angles, as discussed in section 4.1.1.

(f) The depth accuracy of the technique was compared when using single mode *vs.* multimode lasers as illumination sources for the projector in an effort to improve depth accuracy.

Functionality 2: *In vivo* measurement of tissue autofluorescence

Functionality 1 (profilometry) was tested *ex vivo* on tissue phantoms (materials used to simulate how light propagates in tissue) and this was not brought in the operating room in the scope of human studies. As a result, the corresponding system was developed only to fit the surgical microscope at the Polytechnique Laboratory of Radiological Optics (LRO). However, since functionality 2 (fluorescence) was tested *in vivo* during procedures at the Montreal Neurological Institute and Hospital (Neuro), new custom adapters were developed to fit with the neurosurgical microscope there.

(a) Modifications were made to adapt the LCTF/camera system to the Zeiss Pentero microscope at the Neuro where *in vivo* tests in human are conducted.

(b) A calibration method was developed to correct hyperspectral data (reflectance and fluorescence) in order to remove the spectral and spatial response of the instrument.

(c) An algorithm was developed to correct for the attenuation effects of tissue optical properties (absorption and scattering) by normalizing the fluorescence with white light reflectance images in order to produce imaging data specifically related to fluorescence by tissue molecules.

(d) Several modifications in the positioning of the imaging system onto the microscope were made to ensure the surgical microscope auto-balancing procedure can be done with no disruption. This procedure is critical to the surgical workflow since adding pieces of equipment onto the microscope head (*e.g.*, oculars for the assistant surgeon) will modify its weight potentially bringing it off-balance. Auto-balancing is essentially achieved using a tool that detects and analyzes the load onto the microscope and executes a procedure to balance it. This allows the surgeon to apply minimal force while moving the microscope. For that reason, all the parts of the imaging system were set up in a way for the microscope to remain balanced even though additional equipment was placed on it.

(e) A clinical protocol (explained in section 5.1.2 below) was prepared and subsequently approved by the ethics committee at the Neuro.

(f) A preliminary clinical evaluation of the system during tumor resection surgeries was conducted at the Neuro in five patients.

The overall system for phase-shifting profilometry is presented in Figure 3-4, while the system for autofluorescence detection is shown in Figure 3-5. In general, both systems include a stereoscopic neurological microscope (Zeiss OPMI Pentero 900 at the Neuro and Zeiss NC-4 at the LRO, Carl Zeiss, Oberkochen, Germany) connected through a coherent imaging bundle with an LCTF and a highly sensitive camera to detect wide-field images of the surgical cavity. There are two main differences in the optical design between functionalities 1 and 2. For profilometry, a Digital Light Projector coupled with a single mode laser at 638 nm was added allowing to project linear patterns of varying spatial frequencies and phases on the surgical field. For fluorescence,

the internal blue source already integrated by the company Zeiss into the OPMI Pentero 900 surgical microscope (optical power of 8 mW/cm^2 and wavelength range of 400-410 nm [122]) was used to excite tissue fluorescence. This microscope was developed with an imaging mode allowing intraoperative PpIX fluorescence imaging [12]. The spectrum of the blue source (Figure 3-6A) was measured with a spectrometer (Ocean Optics Maya200Pro, FL, USA) in order to select appropriate filters to cut-off excitation light bleed-through during intraoperative fluorescence measurements (details about the filters are found in section 5.1.1.1 below). The light source spectrum is presented in Figure 3-6B on a logarithmic scale to illustrate the importance of including a longpass filter on the detection end in order to minimize bleed-through. This is because filtered bleed-through from the excitation source – if not managed appropriately – can be orders of magnitude higher when compared to anticipated tissue autofluorescence signals.

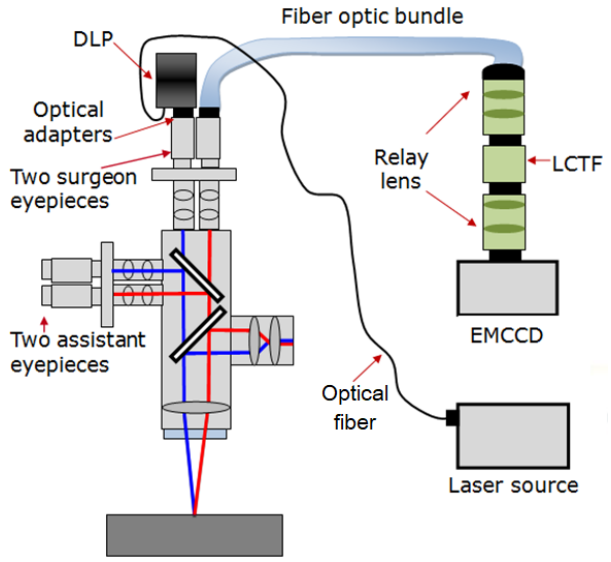

Figure 3-4: Functionality 1: Imaging system design for 3D surface reconstruction of the brain by connecting a DLP and a fiber optic bundle to the stereovision port of the neurosurgical microscope. The projector utilizes a laser source at 638 nm to project structured light onto the interrogated surface.

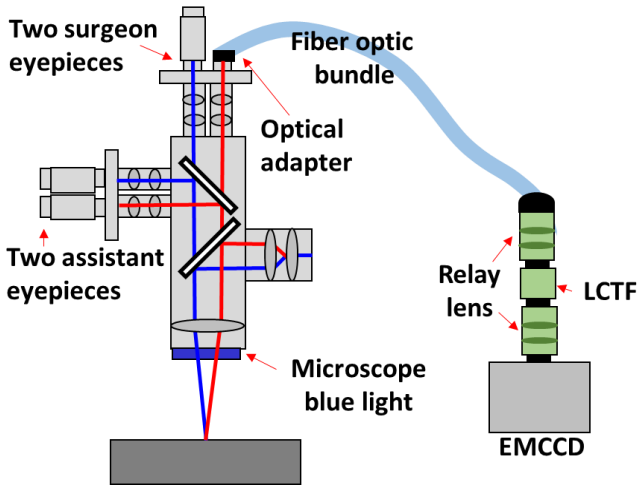

Figure 3-5: Functionality 2: Imaging system design for autofluorescence brain imaging. A coherent bundle transmits images to a LCTF and a high sensitivity camera leading to the acquisition of hyperspectral images. The internal microscope blue light acts as the excitation source for tissue autofluorescence.

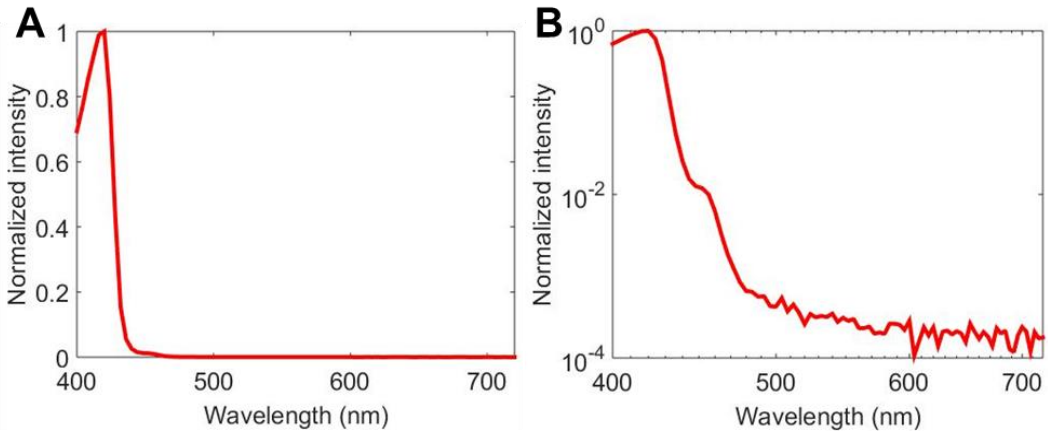

Figure 3-6: (A) Spectrum of the microscope blue source used to excite tissue autofluorescence. (B) The logarithmic plot of the spectrum in (A).

Next, each component of the hyperspectral system is described in detail.

(a) Stereoscopic microscopes

In order to have the flexibility to run preliminary tests at the LRO and use the imaging system in clinical trials at the Neuro, the setup was built to be compatible with two stereoscopic neurosurgical microscopes: the NC-4 at the LRO and the Zeiss OPMI Pentero 900 at the Neuro.

The imaging system is connected to the surgeon's eyepieces. No other microscope free viewing ports could be used because of the occurrence of back reflections. In a microscope, each optical element has a protective layer to reduce the internal reflections of light and improve light transmission through the system [125]. However, in this project, an image is projected through the right eyepiece to illuminate a tissue sample in the microscope field of view (FOV) and an image of the tissue is captured by a fiber bundle that is positioned onto the left eyepiece. However, the anti-reflection film impedes the reflection of light to a lesser or greater extent in each optical port of the microscope. In the case of the surgical microscopes that were used for this project, the anti-reflection coating is more efficient on the surgeon's eyepieces; and when light is projected through the right eyepiece, it is completely attenuated at the left eyepiece. That, however, does not occur in other optical ports of the microscope and the light of the projector is reflected in each one of them, making it impossible for a camera to capture a neat image of the tissue in the FOV, because the image would inevitably show the internal reflection of the projector.

(b) Fiber optic bundle

The imaging bundle (shown in Figure 3-7) has a length of 2.7 meters and a numerical aperture (NA) = 0.63; it effects 72% light loss between its input and output ends. The sensor has a rectangular format of 8 mm x 10 mm and it is composed of fiber arrays where the size of a single fiber is 10 µm [126]. Thus, the sensor contains 800 x 1000 fibers.

Figure 3-7: Imaging bundle with length of 2.7 m and a sensor format of 800 x 1000 fibers, where each fiber measures 10 µm [126].

(c) Liquid crystal tunable filter (LCTF)

The Varispec filter applies liquid crystal elements that are electronically controlled to select the wavelength of interest without moving pieces. The response time of the filter (to change from one wavelength to another) is 50 ms. The VIS (visible) model used in this project is sensitive within the wavelength range from 400 to 720 nm; and it has a bandwidth of 7 nm. The percentage of transmitted light varies between different wavelengths with higher sensitivity towards the NIR region (Figure 3-8). Light passing through the filter needs to be highly collimated otherwise the transmission characteristics shown in the figure can be significantly degraded.

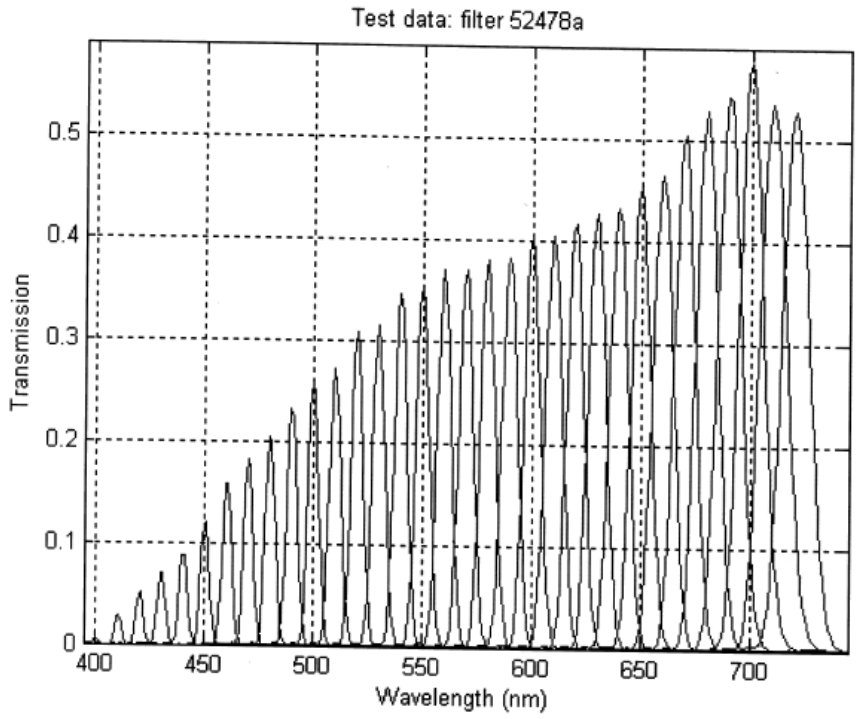

Figure 3-8: Light transmission of the LCTF per wavelength. Image taken from technical documentation of the LCTF (VariSpec).

(d) EMCCD camera

The EMCCD camera (Nuvu Cameras, QC, Canada) provides a spectral detection range from 250 to 1100 nm. The maximum gain is 5000, which refers to the maximum amount of signal amplification provided by the camera (an increment of 5000 in the magnitude of the recorded signal). Further technical characteristics of this camera are summarized in Table A-1 of Appendix A.

(e) Projector

A Digital Micromirror Device chip (DMD, Texas Instruments Inc., TX, USA) forms an image inside the DLP projector. Spatial amplitude and phase modulation of the image projected onto the sample are controlled by the DMD. The chip consists of a matrix of movable micromirrors mounted on a CMOS memory as shown in Figure 3-9**.** The data loaded into the memory spatially controls the ‘on’ and ‘off’ states of each mirror with a ‘1’ or a ‘0’. The ‘1’ and ‘0’ values are

associated with the tilt angle of each mirror: +12 degrees represents an ‘on’ mirror and -12 degrees, an ‘off’ mirror, as seen in Figure 3-10. The reflected light of the ‘on’ mirrors passes through a sequence of lenses to project the image. The gray level in an image is created by assigning a duty cycle to each mirror; that is the percentage of time the mirror is ‘on’ or ‘off’ in relation to the total frame time. Switching between ‘on’ and ‘off’ states is done at a very high speed so the changes are integrated by the observer to form a grayscale image [127].

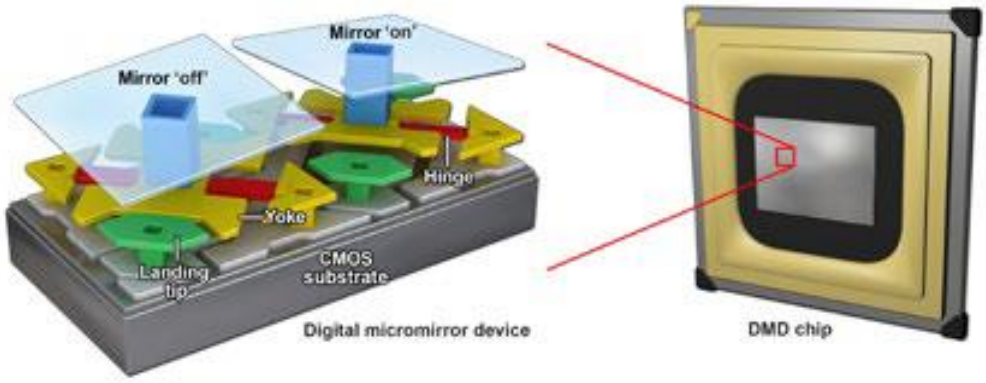

Figure 3-9: The DMD chip (right) is formed by a micromirror array that is positioned on top of a CMOS memory (left) that controls the tilt angle of each mirror [128].

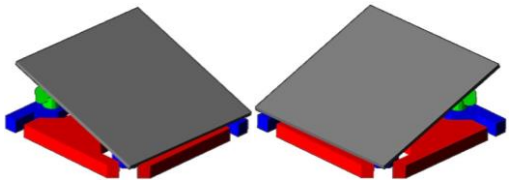

Figure 3-10: Left: micromirror in ‘on’ state tilted at +12 degrees. Right: ‘off’ micromirror at -12 degrees [129].

(f) Light source

The projector was connected to a fiber-coupled single spatial mode laser (Oxxius, Lannion, France), with a peak wavelength at 638 nm; complete technical information is presented in Table A-2 in Appendix A. The red color was chosen because the light transmission of the LCTF is higher at longer wavelengths, as it can be seen in Figure 3-8**.** Additionally, the micromirror array of the DLP should be illuminated by a collimated beam of light with the aim of forming an image

with uniform illumination and also to afford maximum light transmission from the micromirror array to the rest of the optical components in the projector and then to the microscope. However, before the beam illuminates the micromirrors, it goes from the fiber output of the laser through different optical components within the projector that are made of different types of glasses. Light at wavelengths lower than 635 nm (red) would diverge more within the projector due to the larger index of refraction of glass at those lower wavelengths. This directly impacts the collimation of the beam that illuminates the DMD chip and, in consequence, the uniformity of the image coming out of the projector. Finally, the non-uniform illumination of the projected image would limit the accuracy of the profilometry system; and, the low apertures of the microscope would constrain the passage of a more divergent beam, which can cause a major loss of optical power through the system.

On the other hand, a single mode laser coupled to a single mode fiber was chosen over a multimode model because the spatial and temporal coherence of a multimode laser create speckles within the illumination field. These speckles lead to uneven illumination while also adding ample noise to the images, thus, causing inaccuracies in the 3D reconstruction. As a result, coupling the projector with a single mode laser enhances reconstruction accuracy, which will be further explained and demonstrated in section 3.2.1.3.

3.2 Profilometry

3.2.1 Hardware

As part of this thesis, two microscope adapters were built to connect the bundle and DLP projector to the microscope oculars. Optical designs were made to ensure that the size of the projected images on the interrogated surface cover a large FOV (on the order of a few centimeters) and the image transmitted through the fiberoptic bundle captures the same surgical view that the surgeon has through the microscope eyepieces.

3.2.1.1 Adapter for image detection on the microscope ocular

The bundle adapter (TrueTex, FL, USA) is designed to be connected to one of the microscope oculars and it focuses on the ocular's image plane as it is shown in Figure 3-11. A relay lens and

a c-mount objective in the adapter provide a fractional magnification to reduce the image created in the microscope binocular to the smaller size of the Schott bundle image sensor. A design goal was to relay the 21 mm image circle from the binocular's focus field to an 8 mm image circle of the fiber optic bundle to avoid cropping the surgeon's FOV. The resulting relay magnification was 0.38X. The design incorporated a small lens tube to hold filters (*e.g.* for fluorescence imaging) with a diameter of 25 mm. This bundle adapter was designed for two different neuromicroscopes that have different types of eyepieces (Zeiss NC-4 and Zeiss OPMI Pentero 900); hence, the adapter design has a changeable part to fit mechanically each microscope model. The fiber bundle can be firmly fixed to the adapter to always capture the same image orientation. The other end of the bundle is connected to the LCTF and the EMCCD camera through relay lenses consisting of a pair of 35 mm f/1.7 c-mount lenses positioned on each side of the LCTF.

Figure 3-11: The bundle adapter is connected to one of the microscope oculars and it captures an image at the ocular's image plane.

3.2.1.2 Adapter for image projection on the microscope ocular

For an efficient light reflection from the projector to the microscope and to have a uniform illumination across the entire projected image, the DMD should be uniformly illuminated by a collimated beam. Collimation is accomplished using a beam collimator (F220APC-633, Thorlabs, NJ, USA) connected to a FC single mode fiber with a core diameter of 3 µm and NA = .12. A 2 mm beam diameter is the result of collimation by F220APC-633, which is next magnified twice by two 3X expanders (GBE03, Thorlabs), resulting in a final beam diameter of 18 mm. In order to minimize wavefront aberrations in the beam after passing through the

expanders, the maximum input beam size for each GBE03 should be 9.0 mm. Before illuminating the DMD, the magnified circular beam coming out of the expanders is then reflected to a TIR prism (total internal reflection prism, Digital Light Innovations) by a silver mirror (PFR10-P01, Thorlabs) that is positioned at 41.2° with respect to the prism. The TIR prism relies on seven surfaces to transmit light and it discriminates between incident and reflected rays based on a critical angle of 41.2° [130]; thus, the TIR prism only transmits to the DMD all the rays that have an incidence angle smaller than 41.2° and it then reflects the light modulated by the DMD in an orthogonal direction towards the projection lenses at the output of the projector. Finally, a microscopy relay lens with focal length of 45 mm (45-760, Edmund Optics, NJ, USA) and a 30 mm achromatic doublet (AC254-030-A, Thorlabs) form an image of the DMD with magnification of .72X at the image plane of the microscope ocular. The above-mentioned design is detailed in Figure 3-12.

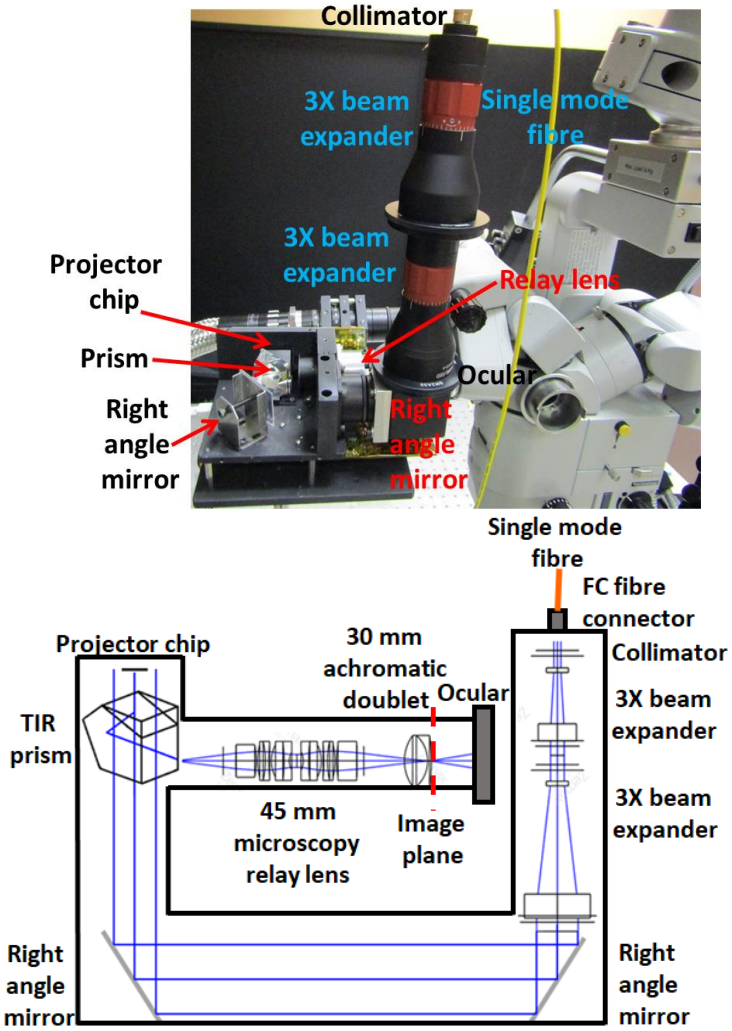

Figure 3-12: Instrumentation schematics for the projector adapter. The optical components to illuminate the DMD with a magnified collimated beam are shown; and also the projection lenses to reflect the image from the DMD towards the microscope ocular.

3.2.1.3 Evaluation of the illumination uniformity with a fiber-coupled single mode laser *vs.* a multimode fiber-coupled laser

To calculate the phase of each pixel that is proportional to depth, the *four step phase-shifting profilometry algorithm* (described in section 2.1.2.3) implemented in this project assumes that the mean intensity value and the peak-to-peak half intensity (I_a and I_b in Eqs. 2-3 to 2-6) of the sine waves are constant among the four projected patterns. In practice, however, this condition is not

always met and the intensity uniformity across the projected sinusoidal fringe patterns can change significantly [131]. In consequence, the uneven illumination of the patterns makes difficult to achieve accuracy in 3D reconstructions.

Figure 3-13A, shows an example of a sine wave pattern generated in Matlab (MathWorks, MA, USA) that was uploaded into the projector. An intensity profile in Figure 3-13B is traced from the pattern in Figure 3-13A to show that the grey level (intensity) value at each pixel along the red dashed line creates a sine wave with uniform peak-to-peak intensities.

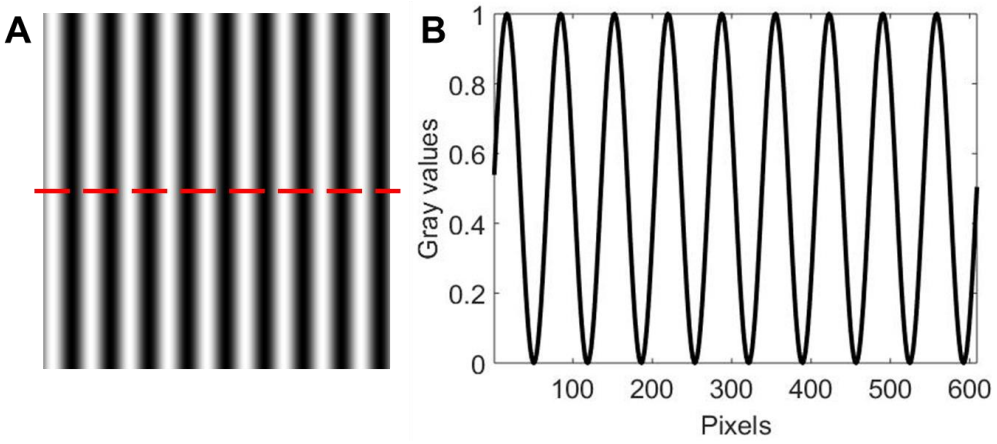

Figure 3-13: (A) Shows an example of one of the theoretical patterns that was uploaded into the projector. (B) The sine wave is created from gray intensity pixel values along the horizontal dotted red line traced on the pattern in (A).

A preliminary test was done with the setup shown in Figure 3-14 to compare the spatial uniformity of the illumination when using a single spatial mode laser *vs.* a multimode source, both already coupled to fiber patch cables. The experimental setup consists of projecting fringe patterns at varying spatial frequencies (frequencies from 1 to 10 sine waves along the length of the projected image) and four $\pi/2$ phase shifts. Each pattern was produced by two laser sources at 635 nm: (a) a tunable laser coupled to a single mode fiber (Fianium white light laser coupled to a tunable Bragg gratings filter, Photon etc, QC, Canada), and (b) a multimode laser (Intense, NJ, USA) coupled to a multimode fiber of small diameter (100 µm) and low NA = .1. Then, a CCD camera (PCO Pixelfly, Kelheim, Germany) was positioned in front of the projection lenses to capture the pattern formed at the image plane. The above-mentioned single mode laser was used

only for the test described in this section, and it was based on the results of this test that it was decided to acquire a high-power single mode red laser that is currently integrated to the through-microscope profilometry setup.

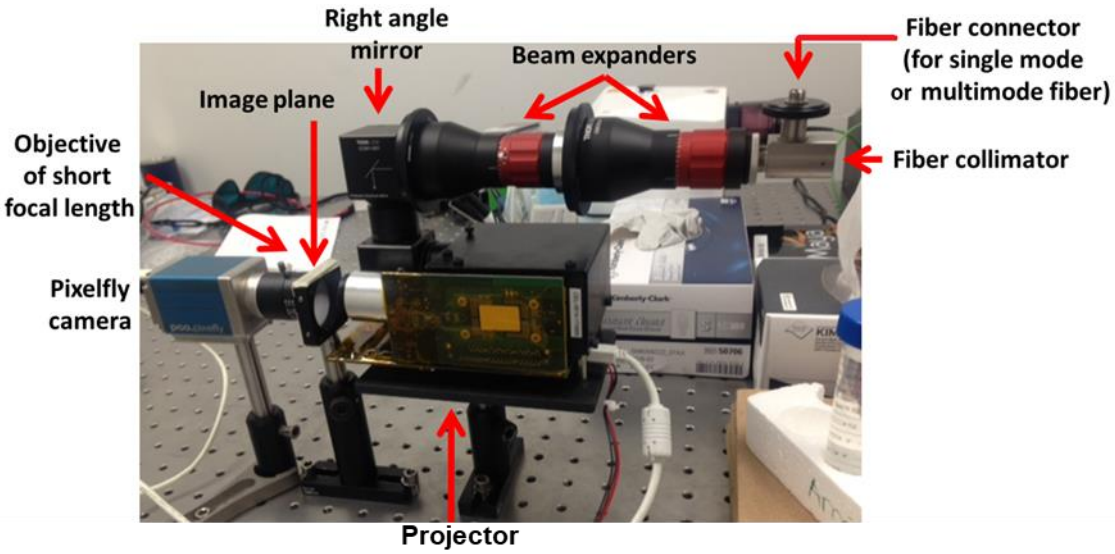

Figure 3-14: Experimental setup to run a preliminary analysis for the errors associated with using single mode *vs.* multimode sources.

The images projected by the single mode and multimode sources were captured on the camera and the mean intensity value of every column was calculated in each image to obtain column by column new data points to create an average sinusoidal wave. This new sinusoidal wave plots the spatial intensity distribution across the projected image. Figure 3-15 shows the mean signal of a pattern created by a single mode (Figure 3-15A) and a multimode source (Figure 3-15B); as seen in the figure, with a multimode source, the grayscale intensity variations across the average sine wave were more significant than with a single mode source. For every pair of images at a specific spatial frequency and phase (generated by single mode and multimode sources), the Root Mean Square Error (RMSE) was calculated between the new average sinusoidal wave and the theoretical sine wave uploaded into the projector. For every pair of patterns at defined spatial frequencies and phases, the RMSE resulted at least 10% smaller for the pattern created by a single mode source in comparison to the one of a multimode source.

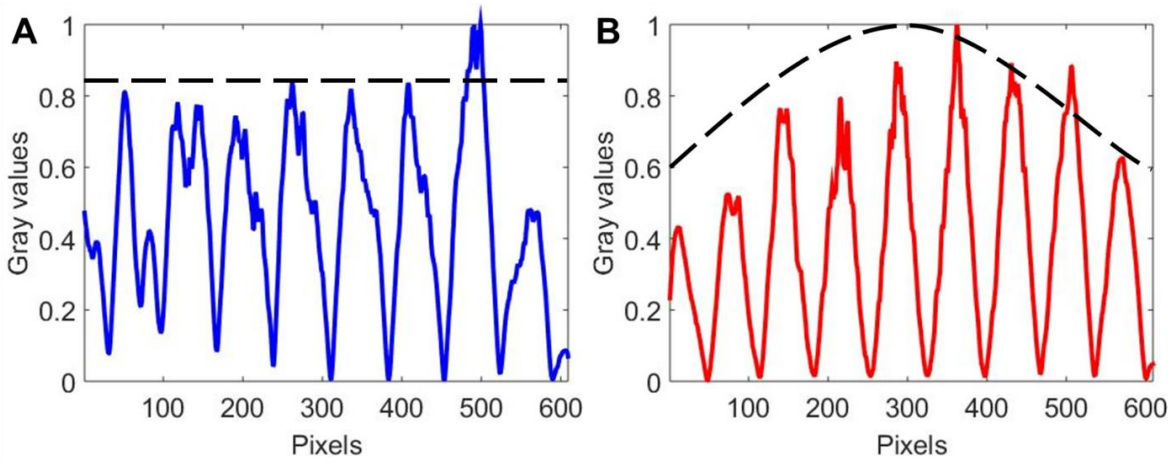

Figure 3-15: (A) Signal created with the average intensity of each column of a sine wave pattern produced by a single mode source. (B) Signal formed with the mean intensity of each column of an image projected by a multimode source.

3.2.1.4 Assessment of the imaging system etendue

To optimize the light transmission from one section of an optical system to another, it is necessary to choose components with similar etendues. The etendue (E) determines the maximum flux of light that can pass through a system. And it could be considered, from the point of view of a chemist, as the entropy of a set of light rays; so it either increases or remains constant when light goes through different optical components such as lenses and mirrors [132], [133]. It's a measure of the light dispersion in a pupil; therefore, it is a function of the emission area (A), and also of the maximum allowable numerical aperture (solid angle, Ω), as shown in Figure 3-16:

$$E = A * \Omega \ [\mathrm{sr} * \mathrm{mm}^2] \tag{3-1}$$

Figure 3-16: The etendue is determined by the emission area of a source and the solid angle of the light cone. For example, 100% of the light would pass from one section of the system to the next one if the ratio of their etendues (E_2/ E_1) was 1.

For an optical component for which the numerical aperture (NA) is known, the etendue is calculated as:

$$E = 2\pi * A * (1 - \cos(\arcsin(\mathrm{NA}))) \quad (3\text{-}2)$$

Although usually not feasible, exactly matching etendues from the illumination source to the rest of the optical components in an apparatus is the ultimate target to achieve maximum light transmission. The percentage of light from the illumination source that is transmitted through the system corresponds to the ratio of etendues as illustrated in Figure 3-16. In terms of light power, this is explained with the following equation:

$$P_{system} = P_{source} \times \frac{E_{system}}{E_{source}} \quad (3\text{-}3)$$

where:

P_{system}: light power received by the system

P_{source}: power of the source

E_{system}: effective etendue of the system that is receiving the light

E_{source}: etendue of the source

However, in the system presented in this thesis the single mode optical fiber acts first as the illumination source since the red laser light is directly transmitted from the fiber to the projector. Next, the DMD chip in the projector acts as the system that receives the light. However, further down in the light travel path, the microscope ocular also receives light from the DMD. It is at this point that the DMD acts as an illumination source and the microscope ocular as the receiving system. In Figure 3-17, two sequential steps are presented to visualize the trajectory that the light travels from the exit of the fiber to the entrance of the microscope ocular.

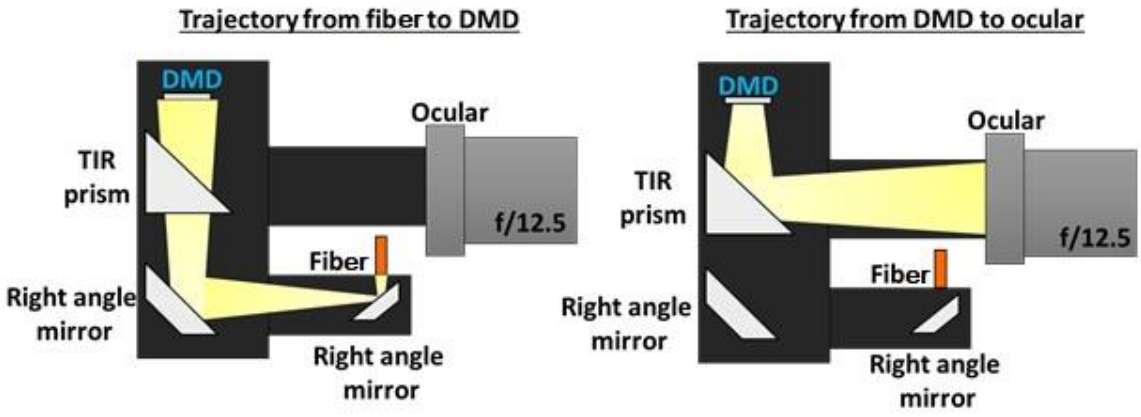

Figure 3-17: Schematic depiction of the light trajectory when illuminating the DMD. Left: first, light travels from the optical fiber to the DMD. The fiber acts as an illumination source and the DMD as a system that receives light for the calculation of a first etendue ratio. Right: light then goes from the DMD to the ocular, and a new etendue ratio should be calculated between these two elements. From this point forward, the DMD acts as a source and the microscope ocular as a system.

The DMD chip of the projector has its own acceptance angle of 12° [130], which is determined by the tilt angle of the DMD mirrors to permit adequate separation of the cone of light that determine the 'on' state of the mirror. It is then necessary to evaluate two different etendues, namely for the projector and for the microscope ocular. This means that an etendue ratio between the single mode fiber of the red laser and the DMD should be calculated, followed by the calculation of another etendue ratio between the DMD and the microscope.

The etendue of a LED is generally larger than that of the DMD given that a LED has a large emission cone. For that reason, a laser was selected as the illumination source for the DMD, as lasers are point sources with a small area and low beam divergence. Since the etendue of the laser source is much smaller in comparison with the DMD it is possible to maximize the transmission of light to the DMD. Then, the only etendue ratio that limits the light transmission in the system is the one between the DMD and the microscope ocular. In summary, the DMD has an etendue of 12 sr*mm^2 while the microscope ocular has an etendue of 1.74 sr*mm^2. The latter was calculated considering an ocular diameter of 21 mm, and an f-number of 12.5. The division

of these two etendues determines a light transmission percentage of ~15% from the projector to the focal plane of the microscope.

3.2.1.5 Overall light loss of the projection system through the microscope

The light losses associated with the etendue mismatch between DMD and ocular are only one of multiple sources of losses. The DMD is a rectangular matrix of micromirrors with a diagonal of 14 mm and pixel dimensions of 1024 x 768 on a 10.8 micron spacing (DLP5500 DLP 0.55 XGA DMD). However, the light beam that illuminates the DMD is circular (diameter = 18 mm) since it has the same shape as the optical fiber. To calculate the percentage of the transmitted light throughout the system, it's then necessary to take into account the ratio between the DMD area and the beam area. In addition, the DMD is not a perfect mirror. According to its technical manufacturer specifications, the micromirrors have a reflective index of 88% and further losses are also caused by other technical characteristics of the DMD, as illustrated in Figure 3-18. To evaluate the maximum percentage of light transmitted from the projector to the interrogated surface, all transmission percentages should be multiplied. The total transmitted light from the output end of the fiber to the surface is then about the 2%.

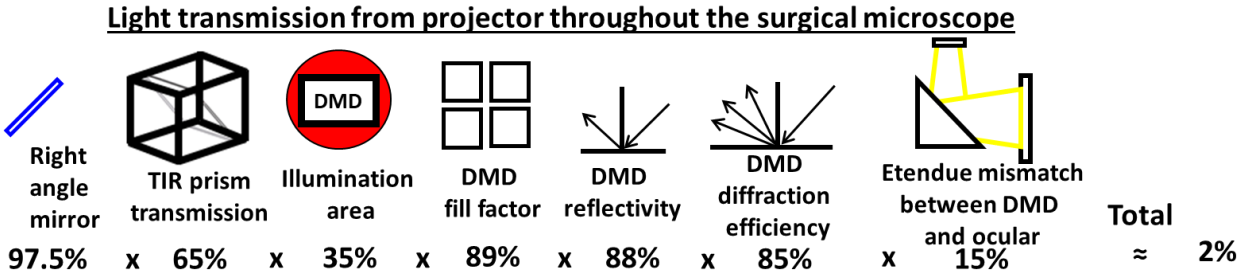

Figure 3-18: Sketch representing the transmission of light by every optical component in the projection system, indicating how much light is lost at every stage.

3.2.2 Data acquisition software

As mentioned, the main components required for 3D profile reconstruction are: a camera and a structured light projector to project sinusoidal patterns at various spatial frequencies and phases. In this thesis both systems were coupled to a commercial neurosurgical microscope. In this context, the acquisition requires a considerable amount of time especially since it involves saving

each projected image and the manual change of structured light patterns between acquisitions, which is not practical during brain surgery. For that reason, a C++ code was written by a summer research student (Laflèche Junior-Blanchette) under my supervision and that of another graduate student (Catherine St-Pierre, M.Sc.) to synchronize the projection of patterns by the DLP and the image acquisition with the LCTF and the EMCCD camera. Previously, this kind of acquisition could easily take half an hour, while now it takes less than two minutes. The tasks involved in automating projections and image acquisitions were:

(a) Design a communication protocol to initialize the camera;
(b) Program a graphical user interface to input acquisition parameters;
(c) Program the main acquisition routine to synchronize the display of an image by the projector and the image acquisition by the LCTF and EMCCD camera;
(d) Integrate the acquisitions into an automatic routine for data storage.

The software interface shown in Figure 3-19 enables the user to select a range of spatial frequencies and phases for the different fringe patterns loaded into the projector and acquire wide-field images in a span of wavelengths with specific gain and integration time. All frames are automatically saved in the selected folder. There is also the option for displaying a live image of the interrogated surface.

The same software also serves for acquiring autofluorescence tissue images (see section 3.3.2) since the function to operate the LCTF is also integrated into the user interface of the software.

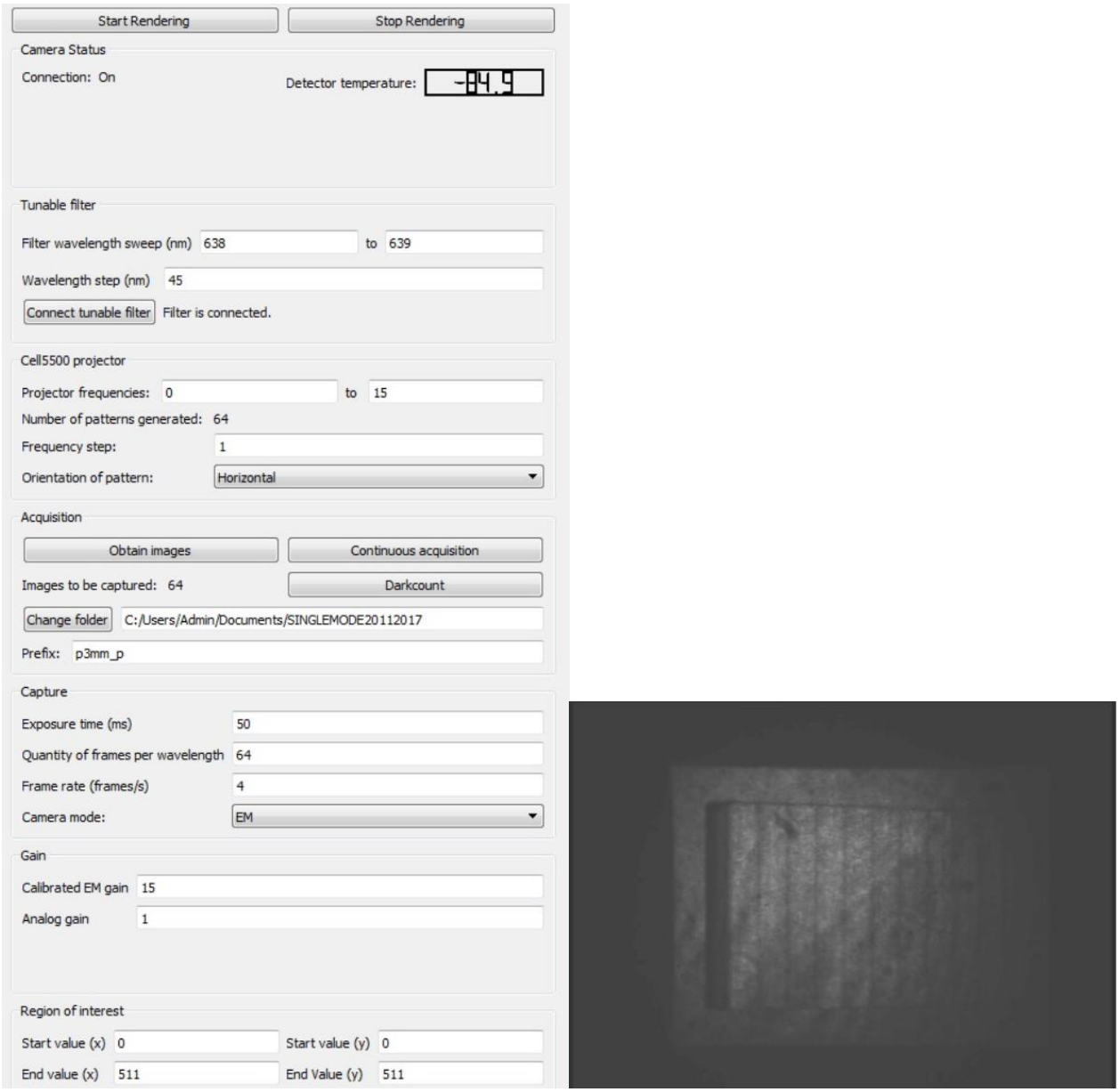

Figure 3-19: Interface developed to synchronize projections and image acquisitions for profilometry and to coordinate the LCTF with the EMCCD camera to save hyperspectral images for autofluorescence measurements. A live image is displayed in the right window.

3.3 Autofluorescence

3.3.1 Hardware: system characterization

To describe the performance of a spectral imaging system some parameters can be specified, *i.e.*, (a) the size of the FOV, (b) the spatial resolution, (c) if there is a linear relationship between the intensity of the measured light and the recorded pixel intensity, and also between the latter and the integration time, and (d) the system response [119]. Each one of these parameters is reported for the system presented in this thesis.

Next, with a focal length of 300 mm (typically used during neurosurgery) and a magnification factor of 1X, the FOV of the image detected by the Zeiss OPMI Pentero microscope and seen through the eyepieces is 132 mm x 104 mm [134]**.** To find out the size of the FOV at variable focal length and zoom settings, a calibration method has been described in [135].

In addition, measuring the spatial resolution of a system serves to know the minimum characteristics of the tissue that the system can visualize and later analyze [119]. The axial resolution for the system presented here was calculated following the Rayleigh criterion by imaging a standard 1951 USAF resolution target at set microscope parameters (zoom = 1X; focal length = 300 mm). The Rayleigh criterion is met for group 1-3 as shown in Figure 3-20; thus, the 2D resolution of the system is approximately 2.5 lp/mm or 198.4 µm, which is considered adequate for observation of tumors on the macroscopic scale [119].

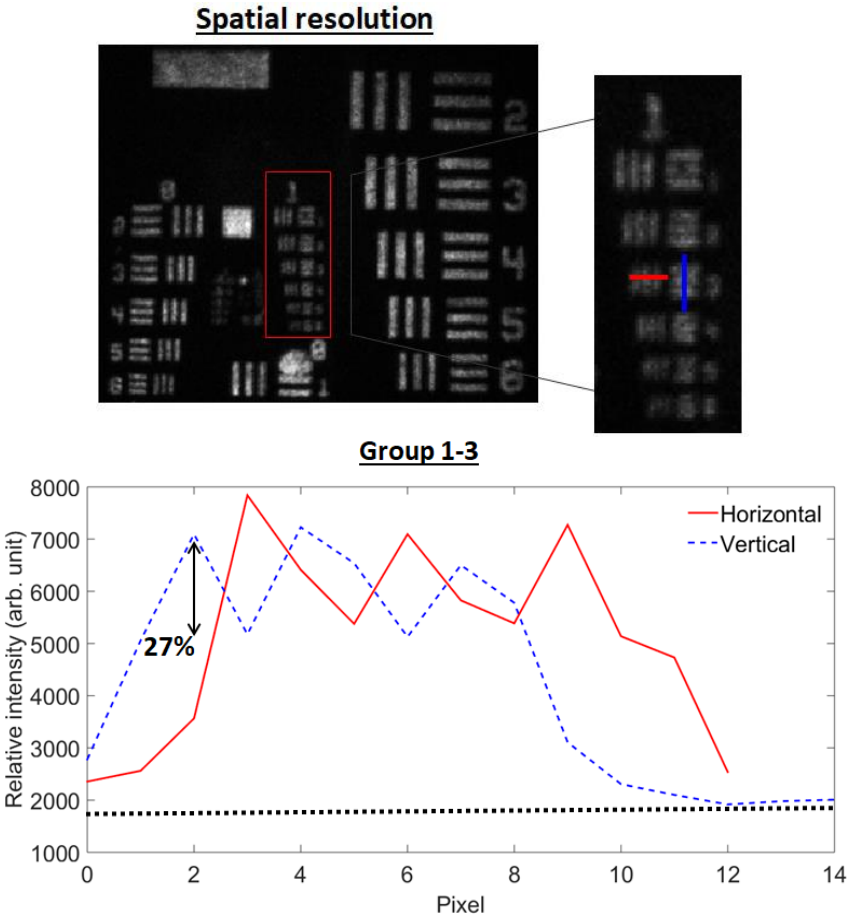

Figure 3-20: The finest details that the imaging system can resolve correspond to group 1-3 of an USAF 1951 resolution target.

On the other hand, verifying whether there is linearity between the light intensity emitted from a sample and the recorded pixel intensity is important in establishing a calibration curve leading to quantified fluorescence images. Likewise, confirming the linearity between integration times and pixel intensities facilitates the normalization of a signal when using different exposure times through simple division [119].

The linearity of measured intensities by a hyperspectral imaging system with the same optical components as the system built during this thesis (consisting of an LCTF and the EMCCD camera) was previously characterized as part of a separate master's research project in the LRO [136], [137]. The EMCCD camera and the LCTF were connected to the OPMI Pentero surgical

microscope of the Neuro. Fluorescent phantoms were created with different concentrations of PpIX: 5μg/mL, 1μg/mL, 200ng/mL, 40ng/mL and 8ng/mL; each concentration of PpIX was used for nine different combinations of optical properties (μ'_s = 15-25 cm^{-1} at 405 nm; μ_a = 20-60 cm^{-1} at 405 nm); images were taken at different integration times: 5, 10, 20, 40, 80 ms. It was found that there is linearity between the pixel intensity and the integration time, and also with the fluorescence intensity. However, it was also reported that the imaging system registered to some extent different pixel intensities for some phantoms with the same PpIX concentration and different optical properties, due to the influence of absorption and scattering in the medium. To correct for this effect, an algorithm for fluorescence quantification was needed. Such algorithm was developed and preliminarily evaluated in the course of this thesis and it is explained in chapter 5**.**

The main difference between the system in this thesis and the hardware settings of the system presented in [136], [137] is that the latter system views an image through the microscope side port, whereas for the system described in this thesis, the camera and LCTF detect the image at the image plane of the microscope eyepiece. For that reason, the linearity was verified again for the new system by making 100 phantoms with PpIX (concentrations in the range of .1 ng-10 μg), intralipid (0.5-2%) as the scatterer, and blood (0.5-5%) as the absorber to mimic the same optical properties as in [136], [137]. As seen in Figure 3-21, it was found that the linearity of measured PpIX intensities is kept till ~40 ng/ml (~10^{-1} ng/ml), suggesting that this is the PpIX detection threshold of the new system because it is the lowest concentration that can be detected before losing linearity. The loss of sensitivity of the new system compared to the one presented in [136], [137] can be traced to the fact that the microscope eyepiece receives considerably less light than the side port, due to its very small aperture (f-number = 21).

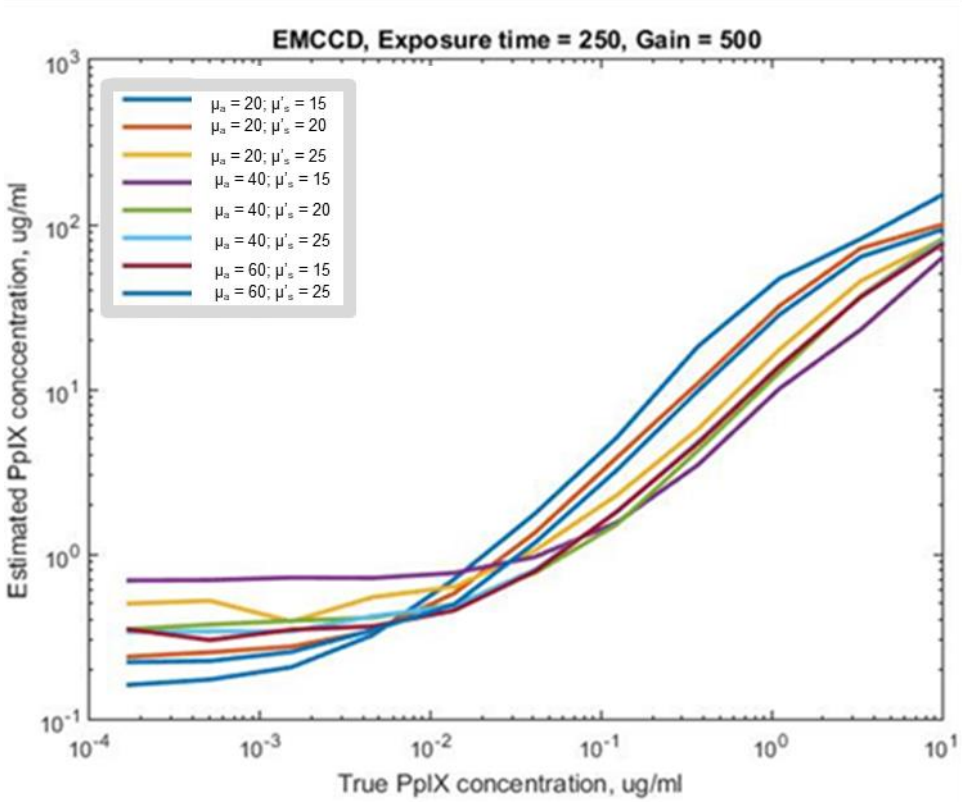

Figure 3-21: Each dataset corresponds to optical phantoms made with a pair of values for μ_a and μ'_s and a range of PpIX concentrations between .1 ng and 10 μg. The plot is linear till ~10^{-1} ng/ml (~40 ng/ml) suggesting that this is the detection threshold of PpIX for the new system.

Alternatively, as presented in [119], to determine if there is linearity between the light emitted from a sample and the intensity recorded in the camera's sensor, hyperspectral images with fixed integration times can also be taken from a Spectralon (a 99% diffuse reflectance standard) when it is illuminated with a lamp as the excitation source. Changes in emission intensity (light reflected from the surface of the Spectralon) can be manipulated by varying the excitation intensity using neutral density filters of different values between the excitation source and the standard. To analyze the linearity of the emission intensity with respect to recorded pixel intensities, the obtained spectra are normalized relative to the maximum intensity. Moreover, to determine if the pixel intensity is proportional to the integration time, different images of the Spectralon can be taken when being illuminated with the same output power but by varying the

integration time among measurements [119]. As before, data can be normalized to the highest intensity.

The measurement of the system response can serve to apply a spectral correction to the captured signal data to retrieve the spectrum of a sample that is not affected by the spectral sensitivity of the instrument [119], as explained in section 5.1.1.1.

To know the system response (*H*) and later correct for it, a NIST (National Institute of Standards and Technology) halogen calibration lamp (Newport, CA, USA) with known spectral output (provided by the lamp manufacturer) was placed in the FOV of the neuromicroscope. The signal (I_{raw}) acquired from the calibration lamp can be modeled as:

$$I_{raw}(\lambda) = I_{lamp}(\lambda) \times H(\lambda) + DK(\lambda) \quad (3\text{-}4)$$

where:

I_{raw}: captured raw signal

I_{lamp}: known spectrum of the lamp

H: system response

DK: dark count measurements obtained when the calibration lamp is off

λ: 550-720 nm with 4 nm steps

Thus, the system response is:

$$H(\lambda) = \frac{I_{raw}(\lambda) - DK(\lambda)}{I_{lamp}(\lambda)} \quad (3\text{-}5)$$

I_{lamp} and I_{raw} (once dark counts have been removed) are both normalized between 0 and 1 because the system response is calculated from the comparison of the intensities at each wavelength between the theoretical spectrum of the lamp and the spectrum of the lamp measured by the

system. The normalization of I_{lamp} and I_{raw} allows easy comparison between the two spectra. Figure 3-22 shows the system response of the imaging setup mounted onto the neuromicroscope.

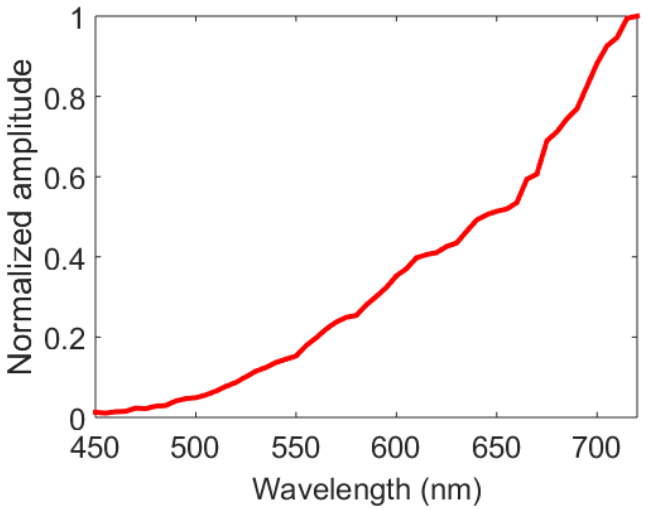

Figure 3-22: The system response (H) of the through-microscope imaging system obtained with a NIST calibration lamp.

3.3.2 Data acquisition software

As explained in section 3.2.2, new software was built as part of this PhD project to control the acquisition of hyperspectral images together with the projection of structured light at different spatial frequencies and phases. This software is meant to be used for data acquisition in autofluorescence and profilometry tests. However, only for autofluorescence measurements is it also possible to use a LabVIEW program (National Instruments, TX, USA) that was developed as part of a master's project at the LRO [136]. The user interface allows the synchronization of the EMCCD camera and LCTF to take and save hyperspectral images in real time. Different values can be entered for parameters like integration time, camera gain and wavelength range. In comparison with the C++ user interface described in section 3.2.2, the LabView program does not include the function of controlling the projector.

CHAPTER 4 BRAIN SURFACE PROFILOMETRY

4.1 Methods

4.1.1 Profilometry measurements at different heights

The projected image occupies an area of 4 x 3 cm in the Zeiss NC-4 microscope field of view at pre-defined microscope magnification and focal length values (zoom = 1X; focal length = 300 mm). The light power at 638 nm on an illuminated area projected at the zero spatial frequency (DC) is 85 $\mu W/cm^2$. The measurement was taken at a distance of 30 cm from the microscope to the image plane. The projection covers 308 by 232 pixels on the camera sensor, which corresponds to 78 pixel/cm.

To determine the 3D reconstruction accuracy and precision of the profilometry system, six step pyramids were 3D-printed. The heights of the steps varied in each pyramid from 1.5 mm to 30 mm. The overall height of all the pyramids was around 40 mm to keep it within the depth of field of the microscope (40 mm) [134]. This means this height is always in the focus range of the microscope and, therefore, it can be reconstructed. Each pyramid was printed in white to improve reflectivity and a final reconstruction for each pyramid was obtained after averaging single reconstructions with different spatial frequency projections in the span of 4 to 7 fringes along 4 cm (1-1.75 cm^{-1}). To sum up, for every pixel of the image, the height is recovered running the 3D reconstruction algorithm for a set of projections with different spatial frequencies (1-1.75 cm^{-1}). Then, to slightly smooth the 3D surface, a [13 13] Weiner filter is applied to each reconstruction and all the reconstructions are then averaged.

The choice of spatial frequencies to perform profilometry was based on the fact that preliminary reconstructions of objects with different heights (from 1.5 mm to 30 mm) were carried out from pattern projections within a wide range of spatial frequencies (.25-3.75 cm^{-1}); then the accuracy of depth calculation was evaluated at individual spatial frequencies and also when averaging groups of frequencies. It was found out that the average of spatial frequencies from 1 to 1.75 cm^{-1} demonstrated enough sensitivity to detect large and small height changes, as shown in the Results section 4.2 below.

As mentioned before, the patterns were generated through a single mode laser at 638 nm (Oxxius), coupled with a single mode fiber (core diameter = 3 µm; NA = .12). However, the same experiment was repeated for a multimode source (Intense) at 635 nm, connected to a multimode fiber with a small core diameter of 105 µm and low NA = .1 (M96L02, Thorlabs) with the aim of evaluating if the accuracy of 3D reconstructions depends on the type of laser source, as shown in section 4.2.1.

Spatial amplitude and phase modulation of the projected sine patterns were controlled by the custom user interface programmed in C++ presented in section 3.2.2. The interface enables the user to select the spatial frequency of the sine patterns while controlling simultaneous image acquisition to retrieve wide-field 3D hyperspectral images.

4.1.2 Profilometry measurements at different angles

The projected images have similar spatial characteristics as the ones projected for height measurements in the previous section. A flat adjustable angle platform (AP180, Thorlabs) was positioned at 0 degrees (perpendicular) with respect to the head of the surgical microscope. Then, the platform was moved at ±15°, ±30° and ±45° along the *x*-axis, as seen in Figure 4-1 (Left). The same platform was rotated along the *y*-axis at the same angles as before (Figure 4-1 (Right)).

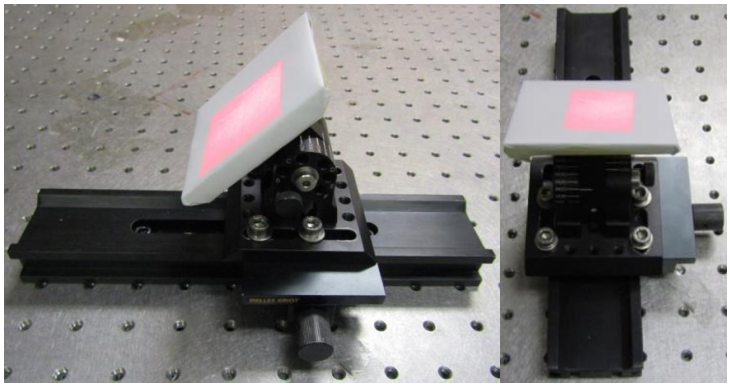

Figure 4-1: Left: platform rotates along the *x*-axis. Right: platform rotates along the *y*-axis.

4.1.3 Tissue-like phantom measurement

A brain-shaped phantom was made with specific absorption and reduced scattering coefficients (μ_a = 2 mm^{-1} and μ'_s = 2.5 mm^{-1}) consistent with values found in the literature for brain tissue

[141]. It consisted of a mixture of intralipid, water and blue food coloring. The phantom was solidified by adding 0.6% agarose as suggested in [142].

4.2 Results

4.2.1 Profilometry measurements at different heights

As previously mentioned, reconstructions at different heights were made using, both, fiber-coupled single mode and multimode lasers. With the red single mode laser source, all the pyramid steps were reconstructed with an average relative error (the theoretical height minus the measured height, divided by the theoretical height) less than 3%, as seen in Figure 4-2A. Then, the accuracy of the profilometry system was determined based on an average absolute error of 0.3 mm. The standard deviation was calculated among the estimated heights across the full surface of every step to describe the height variation. The average standard deviation for all the step areas was less than 0.6 mm and this is equivalent to the precision of the profilometry system. Figure 4-2C shows the transversal area from a reconstruction of a single pyramid step to exhibit the height distribution on the entire step area. The reflectance image of the whole pyramid is shown in Figure 4-2B; and the 3D-map in Figure 4-2D. In Appendix B, Table B-1 shows the real height of every pyramid step, together with the computed height and the errors associated with the reconstruction.

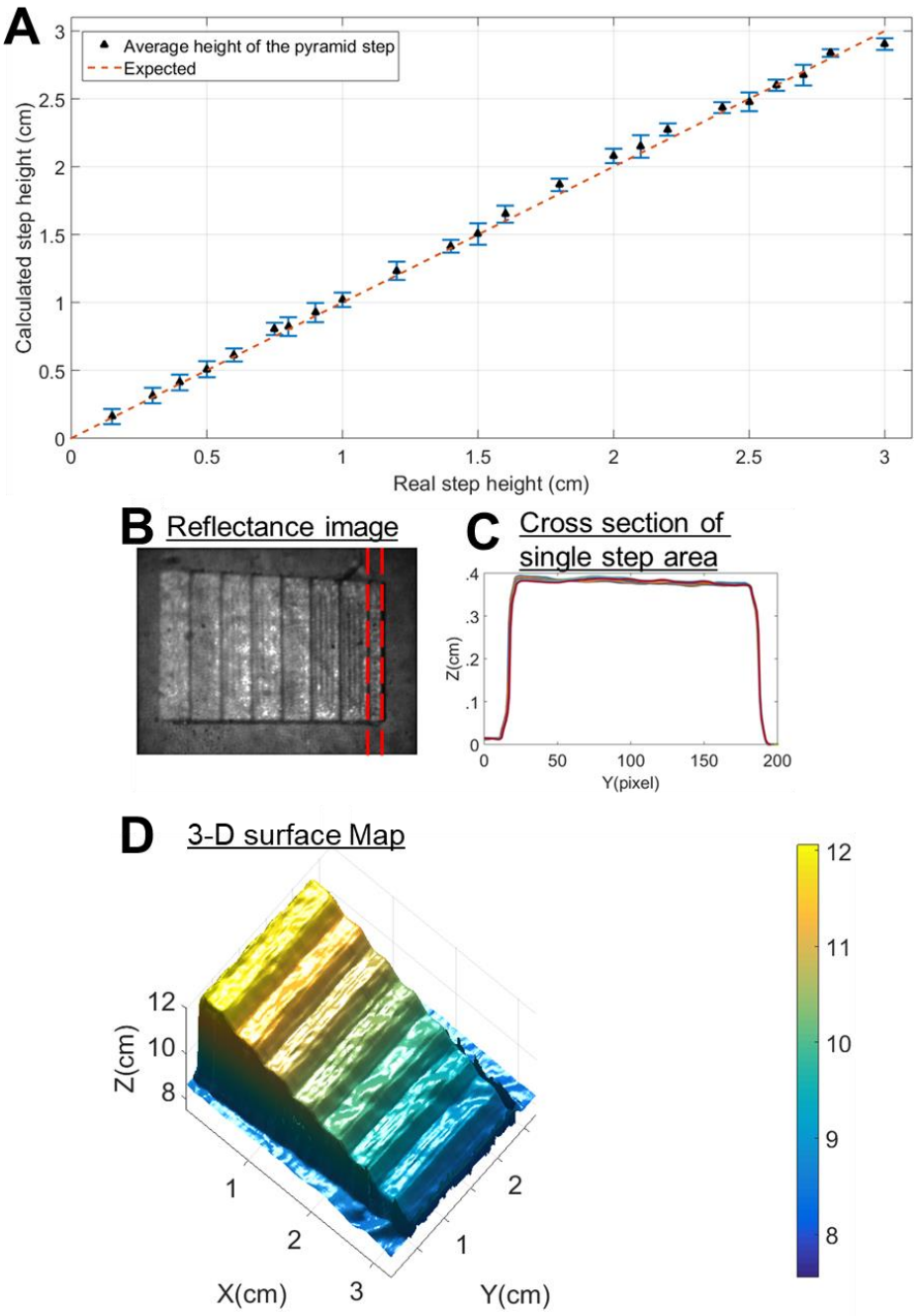

Figure 4-2: (A) Measured height of different pyramid steps as a function of the real step height. (B) Reflectance image of one of the pyramid phantoms. The cross section of the first step is outlined; the height of this step is 4 mm. (C) The transversal area of the step selected in (B) is sketched showing the low height variability across the step. (D) The 3D-surface map of the pyramid shown in (B).

Next, a similar test to measure heights of stepped pyramids was done using a red multimode source. Figure 4-3 shows how the calculated heights differ from the real step heights. In Appendix B, Table B-2 shows the real step heights of the pyramids, the heights of the reconstructed steps and the errors of the reconstructions. For the multimode source as the illumination source, the average accuracy was ~1 mm (average relative error ~10%), whereas, for the single mode source it was ~0.3 mm (average relative error ~3%). Figure 4-4 compares two pyramids that were reconstructed from images created by single mode and multimode laser projections. From the color bar, it can be noticed that the calculated heights at each pixel of every step are more variable for the reconstruction with a multimode source (on the right); this is because the baseline of such reconstructed pyramid is not as flat as for the pyramid on the left (created from images projected with a single mode laser), and these abrupt baseline level changes affect the calculated height of every pyramid step.

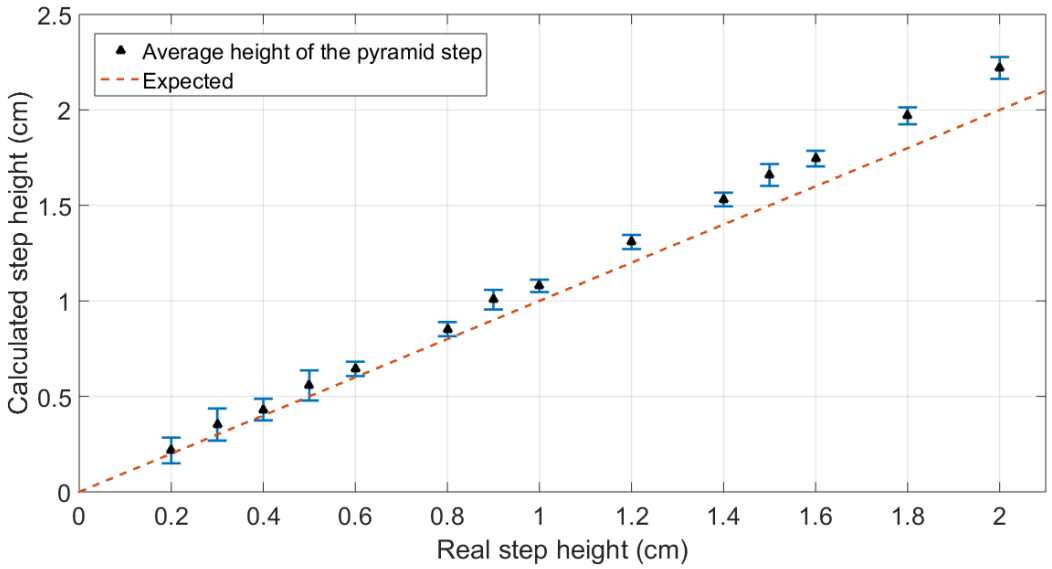

Figure 4-3: Step reconstructions with a multimode laser source. The real step height represents the physical measurement of every pyramid step that was 3D-printed. The calculated step height is the value given by the reconstruction.

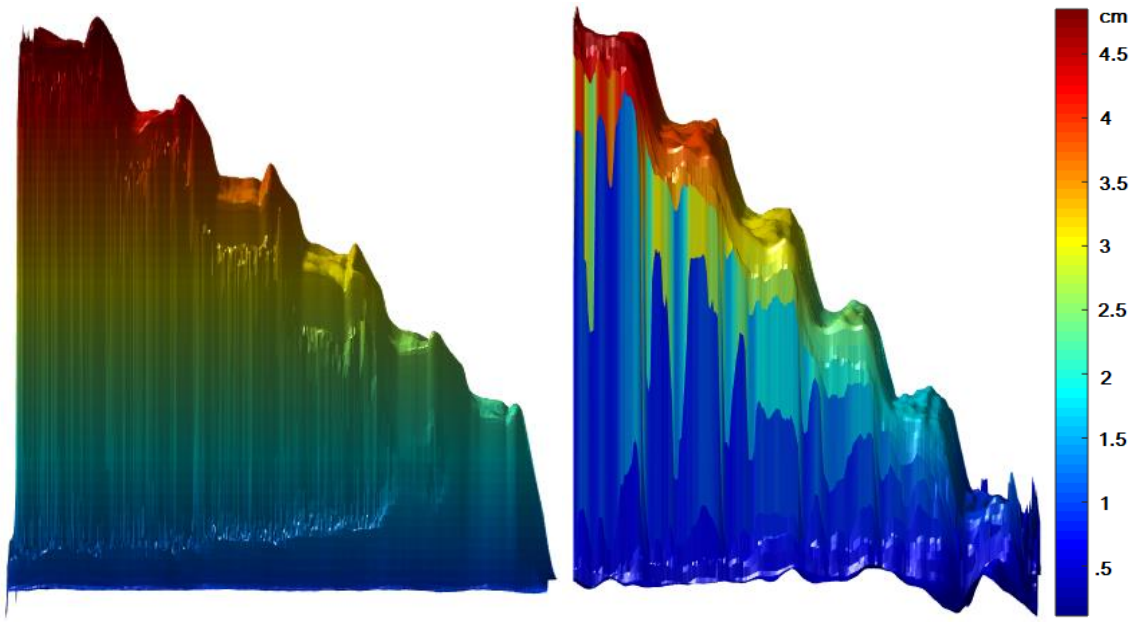

Figure 4-4: Left: pyramid that was reconstructed from patterns projected by a single mode laser. Right: pyramid reconstructed with a multimode laser as the illumination source. The color bar represents the computed height of every step.

4.2.2 Profilometry measurements at different angles

When the adjustable angle platform was moved along the *x*-axis, the object's profile was rebuilt forming side-tilt maps (Figure 4-5) after averaging individual reconstructions for spatial frequencies in the range 1-1.75 cm^{-1}.

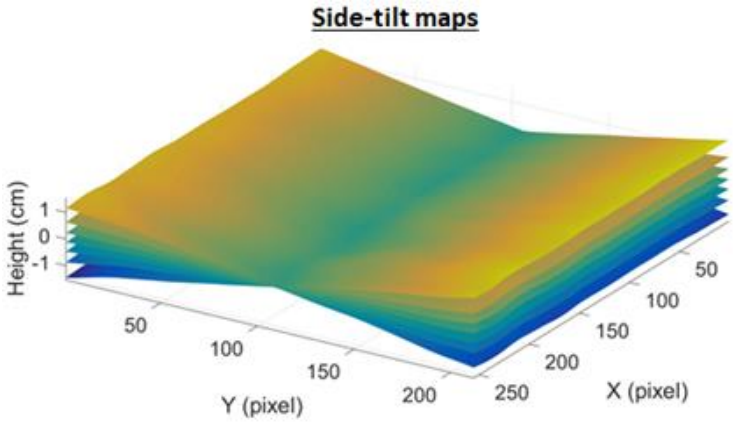

Figure 4-5: Reconstruction of side-tilt maps after rotating the platform along the *x*-axis.

Front-tilt maps (Figure 4-6) were created with the average of the same spatial frequencies as before, when the platform moved along the *y-axis*.

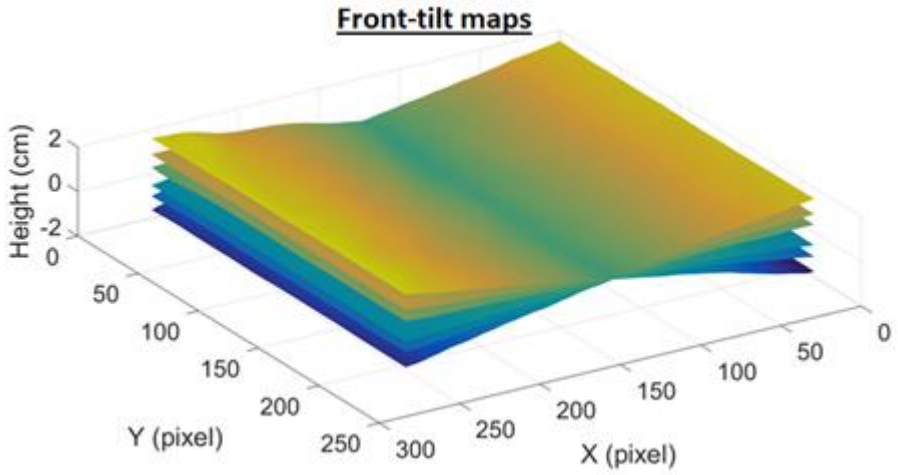

Figure 4-6: Reconstruction of front-tilt maps built when the platform rotated along the *y*-axis.

The tilt accuracy is shown in Figure 4-7; the mean reconstruction error for all angles was 1.94 degrees (STD = 1.2 degrees).

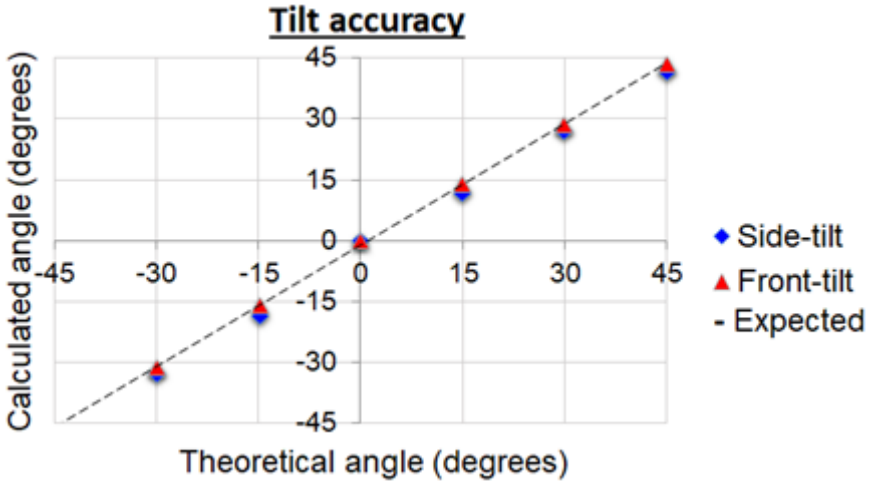

Figure 4-7: Measured tilt angles as a function of the expected real angles.

4.2.3 Tissue-like phantom measurement

The reconstructed brain profile is presented in Figure 4-8.

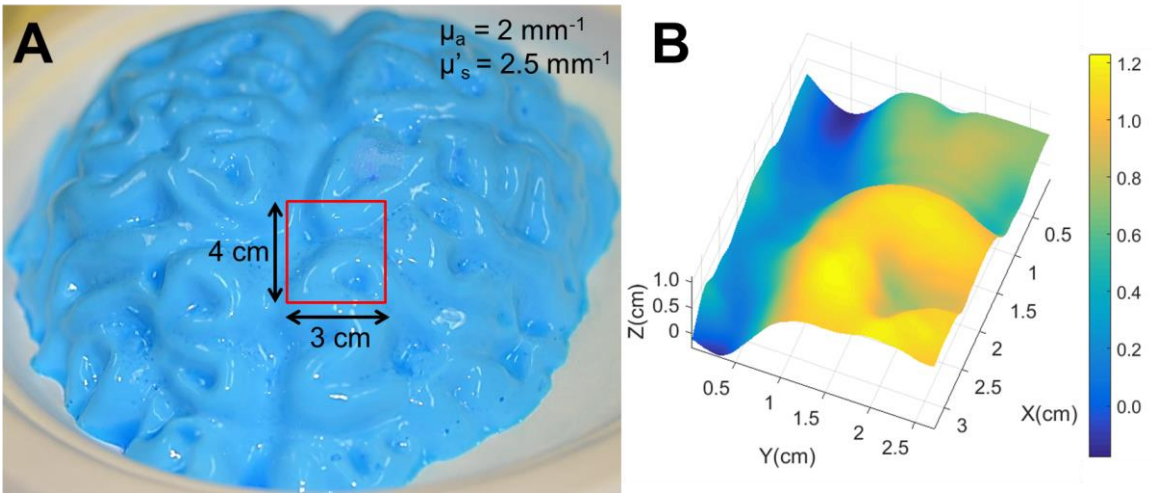

Figure 4-8: (A) A solid phantom simulating the optical properties of brain tissue was made and it was then illuminated by fringe projections of 4 by 3 cm. (B) The 3D reconstruction of the selected region in (A) is shown.

CHAPTER 5 MEASUREMENT OF TISSUE AUTOFLUORESCENCE

5.1 Methods

5.1.1 Image analysis

5.1.1.1 Spatial and spectral calibration

Preliminary experiments for spatial and spectral calibration of hyperspectral images were conducted on: (a) a flat block that does not emit fluorescence, (b) a sample of powder-form PpIX (Sigma-Aldrich, MO, USA) diluted in DMSO (concentration = 100 µg/ml), and (c) a calf brain. The image analysis technique for spatial and spectral calibration presented here was then applied to human data obtained *in vivo* during a brain tumor resection clinical case at the Neuro. Even though five clinical cases were conducted using the imaging system presented in this thesis, data from a single case is shown in this thesis document because during the first four cases the camera acquisition parameters (gain and integration time) were not optimal to retrieve high-quality images with high contrast-to-noise ratios, as described in section 5.1.6.

Spatial correction was validated by verifying the uniformity of reflectance images, *i.e.*, having similar pixel intensity values across a reflectance image, of the flat block and of the calf brain.

Spectral correction was measured by comparing the recorded spectrum of PpIX with a theoretical spectrum from the literature. Then, autofluorescence and white light reflectance signatures were retrieved on a calf brain and their shapes were compared with brain spectra from the published literature. Diffuse reflectance and fluorescence spectra shown in this chapter are the average spectra in image regions of 20 x 20 pixels.

Spatial and spectral calibration was performed for reflectance measurements following this procedure:

1. Images in the range 550-720 nm were acquired on a diffuse reflectance standard (Spectralon, LabSphere, NH, USA) while being illuminated by the internal white light excitation source of the microscope.

2. The dark count was subtracted from the images of the Spectralon at each wavelength and the dataset was then normalized by dividing by the camera gain and integration time
3. In order to later perform a spatial correction on all acquired images, the Spectralon images at all wavelengths were added together to provide an image of the spatial distribution of the illumination source on the sample, and the dataset was then scaled to a range between 0 and 1.
4. Raw reflectance data is acquired on the sample (*e.g.*, surgical cavity) when it is illuminated by the microscope white light. Dark count is also removed (subtracted) from the raw reflectance data of the sample. The result of that subtraction is then divided by the camera gain and integration time in order to obtain a hyperspectral image dataset denoted as R_{raw}^{d}.
5. To carry out the spatial correction, the hyperspectral image dataset R_{raw}^{d} is divided by the image of the Spectralon that captures the spatial distribution of the white light (obtained in step 3).
6. The microscope white light source spectrum (excitation source for diffuse reflectance, I_o) was recorded with a spectrometer (Ocean Optics Maya200Pro) and normalized to unity. The spectrum is shown in Figure 5-1.

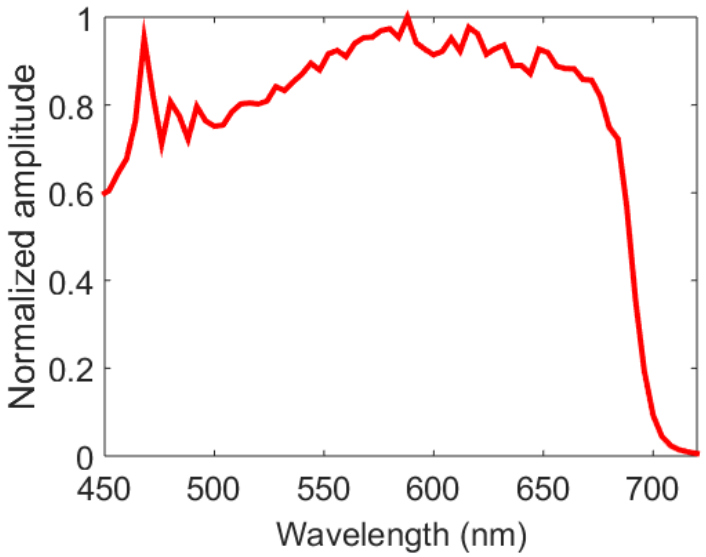

Figure 5-1: Spectrum of the microscope white lamp (I_o) measured with a spectrometer.

7. The output of the system for reflectance measurements is:

$$R^{d}_{raw}(\lambda) = I_o(\lambda) \times R^{d}_{corrected}(\lambda) \times H(\lambda) \quad (5\text{-}1)$$

where:

$R^{d}_{corrected}$: the true reflectance signal coming out of the tissue

H: the system response

I_o: the spectrum of the microscope white lamp

From here, we can obtain (Eq. 5-2) the white light reflectance image of the tissue that is spatially and spectrally corrected ($R^{d}_{corrected}$).

$$R^{d}_{corrected}(\lambda) = \frac{R^{d}_{raw}(\lambda)}{I_o(\lambda) \times H(\lambda)} \quad (5\text{-}2)$$

8. Once the corrected white light reflectance signal of the tissue is obtained, next, the fluorescence signal (signal obtained from the sample when it's illuminated under blue light) is calibrated with the same algorithm. Except that, to carry out the spatial correction on fluorescence images, the Spectralon should be illuminated by the blue source that is part of the microscope illumination system instead of the white light. Besides, for fluorescence signals, the term I_o in Eq. 5-2 is removed since the spectral recording is from 550 to 720 nm, thus it doesn't capture the blue excitation source of the microscope that has a spectral bandwidth from 400 to 410 nm; in addition, there are two longpass filters at 442 nm (BLP01-442R-25, Semrock, NY, USA) in the system to eliminate most of the excitation light. The optical filter spectrum is shown in Figure 5-2.

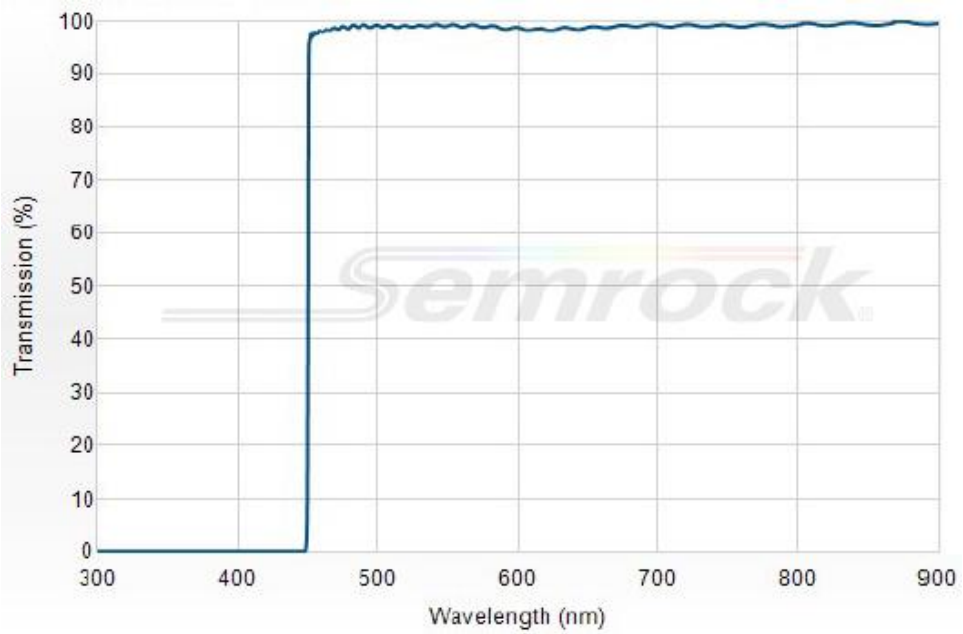

Figure 5-2: Longpass emission filter with cut-on wavelength = 442 nm [143] to eliminate blue excitation light in fluorescence measurements.

5.1.1.2 Fluorescence normalization algorithm

In the previous section, it was described how to calibrate – spatially and spectrally – a set of images associated with tissue reflectance and fluorescence. Additionally, an algorithm for fluorescence retrieval was developed to apply a reflectance-based correction to the fluorescence data to decouple intrinsic tissue absorption and scattering from the detected fluorescence signals. The objective was to ensure the corrected fluorescence images convey information pertaining specifically to fluorescent tissue molecules without the confounding effect, *e.g.*, of absorption from hemoglobin, which can vary significantly across the field of view. Therefore, after calibration of reflectance and fluorescence images, a novel formulation that was developed during this thesis is applied for the correction of wide-field fluorescence data. The algorithm is based on the Beer-Lambert law and is fully described in Appendix C. The degree of fluorescence is corrected pixel-by-pixel by considering the amount of the light transmitted from the sample. The Beer-Lambert law relates the transmitted light to the absorption (provided by different concentrations of oxy- and deoxyhemoglobin) and scattering in tissue. And, as previously

mentioned, white light diffuse reflectance images contain information about changes of tissue absorption and scattering. For that reason, in this thesis the fluorescence emission spectrum at each pixel was directly corrected with white light reflectance images using the following formula:

$$F_C(\lambda) = 10^{\left(\log_{10}(F_R(\lambda)) - \log_{10}\left(R_d^{corrected}(\lambda)\right)\right)} \quad (5\text{-}3)$$

where:

$F_{C:}$ corrected fluorescence

F_R: fluorescence dataset that has been calibrated spatially and spectrally

$R^d_{corrected}$: white light diffuse reflectance images already calibrated spatially and spectrally

λ: individual wavelengths from 550 to 720 nm in 4 nm intervals

5.1.2 Protocol for clinical cases for *in vivo* detection of autofluorescence

The clinical cases were conducted in human patients with a brain tumor at the Neuro after obtaining ethical approval from the Research Ethics Board (REB). The imaging system was tested *in vivo* in five patients during brain cancer surgeries. In the course of the first four cases, image acquisition parameters (camera gain and integration time) were optimized to achieve levels of contrast-to-noise ratios (explained in section 5.1.6) allowing to retrieve the autofluorescence signature of brain tissue**.** The objective was to detect spectroscopic tissue autofluorescence and correct data with white light reflectance to decouple intrinsic tissue attenuation factors associated with absorption and elastic scattering. During the surgeries, imaging with the hyperspectral fluorescence system was achieved at two stages: (a) tumor fully exposed, (b) when the surgery is complete.

Below, the specific procedures developed for intraoperative data acquisition are presented. At the end of the surgery, an image of the reflectance standard (Spectralon, LabSphere) was taken under blue and white light illumination. These datasets are used to apply the spatial calibration to correct differences in the spatial distribution of the excitation light, as explained in section 5.1.1.1.

5.1.3 Mechanical integration of the hyperspectral system for intraoperative use

The microscope must undergo auto-balancing and must be draped (to keep the surgical field sterile) before conducting imaging tests, as shown in Figure 5-3A. For visualization of the surgical cavity, precise positioning of the microscope by the surgeon is important and the microscope should be able to rotate in every direction. To ensure that the length of the bundle doesn't hinder the free motion of the microscope, the LCTF/EMCCD camera system was mounted on an optical table at the back of the microscope and it was lifted up with 1-meter length poles in order to put the bundle closer to the microscope arm (Figure 5-3B). With this configuration the bundle is long enough to allow the unrestricted movement of the microscope as seen in Figure 5-3C. However, when auto-balancing the surgical microscope at the Neuro the entire movement of the microscope was blocked by the microscope control system because it detected the force exerted by the bundle that was attached to the microscope oculars. To solve this problem, it was decided to change the Pentero oculars for a more robust pair with no moving parts (Figure 5-3D). This new set of oculars was removed from a surgical microscope with similar optics (Zeiss NC-4) that belongs to the Laboratory of Radiological Optics at Polytechnique Montreal.

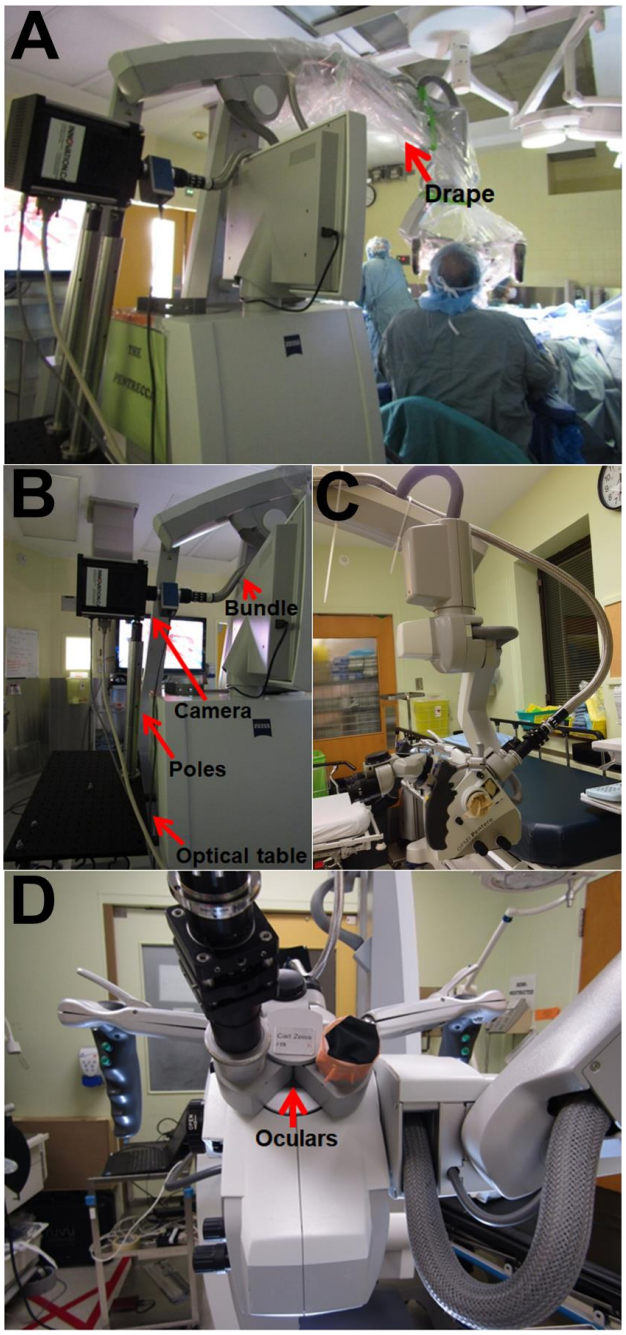

Figure 5-3: (A) The fiber bundle is attached along the microscope arm and the microscope is draped before the procedure. (B) Hyperspectral system mounted onto an optical table at the back of the microscope for use in the operating room during surgery. (C) The bundle is long enough to achieve the proper range of rotation and motion needed with the microscope. (D) A pair of oculars with no moving parts but same optical characteristics as a Zeiss OPMI Pentero ocular pair was used as a replacement to facilitate balancing the surgical microscope.

5.1.4 Intraoperative optical data acquisition parameters

1. Image acquisition sequence for each of the two imaging sessions during a clinical case: (a) fluorescence imaging under blue excitation; (b) reflectance imaging under white light illumination; (c) dark counts recording with same gain and integration time as for fluorescence; (d) dark counts recording with same camera parameters as for white light diffuse reflectance.
2. Fluorescence excitation carried out with the OPMI Pentero blue light (bandwidth 400-410 nm) set to 100% intensity.
3. White light illumination for reflectance measurements using the internal microscope white light lamp also set to maximum intensity.
4. Spectral acquisition in fluorescence and reflectance mode within the 550-720 nm spectral coverage of the LCTF in increments of 4 nm. Fluorescence images are not acquired for wavelengths below 550 nm because of the prominence of excitation source bleed-through.
5. Camera gain: For fluorescence a camera gain of 500 was found to be optimal for maximizing the levels of signal-to-noise ratio. The NUVU camera manufacturer recommended not using a gain above 500 in EMCCD mode, since the background noise would be amplified while reducing the dynamic range. For reflectance, a camera gain of 50 was found to be optimal.
6. Integration time: For fluorescence, 250 ms was found to be best to allow recording the fluorescence signal. For reflectance, 3 ms leads to sufficiently high levels of measured signal. The total acquisition time in the operating room for each imaging session was two minutes, taking into account that for every fluorescence or reflectance measurement dark counts with same gain and integration time needed to be acquired for calibration purposes.
7. Optical power of microscope blue excitation source: 8 mW/cm^2, which approximately corresponds to the maximum permissible exposure for skin set by ANSI standards from the Laser Institute of America.

5.1.5 Multimodality imaging for fluorescence and structural rendering of the surgical cavity

In order to provide structural context with the fluorescence images, the diffuse reflectance data was used to reconstruct an RGB image of the surface, providing information similar to what surgeons observe when using the surgical microscope. In this thesis, the method published in [144] was used to transform hyperspectral data of the brain to RGB images. For fluorescence imaging, the hyperspectral system used in this project was programmed to provide individual images every 4 nm in the range of 550-720 nm. The empirical algorithm, previously explained in section 5.1.1.2 to correct the tissue autofluorescence with white light reflectance was applied to human *in vivo* data and a map of corrected fluorescence intensity was overlaid on a diffuse reflectance image; where, fluorescence and reflectance intensities were the sum of pixel intensities at every wavelength. The integrated fluorescence intensity over the emission wavelengths showed an overall difference between the magnitude of fluorescence for tumor and healthy regions in the brain as shown in the following Results section 5.2.

5.1.6 Data quality assessment: contrast-to-noise ratio (CNR)

To evaluate the overall quality of a fluorescence image, the contrast-to-noise ratio (*CNR*) metric is used. This can be useful to determine detection capabilities in low contrast images. For example, the higher the *CNR* associated with an abnormality when compared to normal tissue background, the easiest it is to visualize it [145]. In general, this metric provides an estimate of how much the difference between the signal and background stands out from pixel variations [145], as it is exemplified in Figure 5-4. The formula for *CNR* is:

$$CNR = \frac{(\mu_o - \mu_B)}{\sigma_B} = \frac{\Delta_\mu}{\sigma_B} \tag{5-4}$$

where $(\mu_0 - \mu_B)$ is the contrast between two structures, meaning the difference between the average pixel intensity of an object and the average pixel intensity of the background surrounding such object; and σ_B is the standard deviation of the background (pixels outside the area of the object under study). In contrast, the image noise can be quantified using the signal-to-noise ratio

(*SNR*) metric which in situations where photonic noise (rather than camera noise associated with readout or dark noise) dominates can be increased by decreasing σ_B. For such shot-noise dominated measurements – which is the case for intraoperative fluorescence detection in this thesis – increasing the *SNR* is tantamount to maximizing the light intensity detected. The *CNR* and *SNR* of an image can be maximized by choosing light exposures, camera gains and integration times ensuring each imaging frame fills as much as possible the dynamical range of the camera.

However, the *CNR* can be impacted by the ambient light in the operating room which introduces contributions that are not tissue specific. As a result, consistently achieving high *CNR* values in the operating room is not an easy task. To minimize the impact of operating room light during the clinical cases at the Neuro, the main surgical lights were turned off and camera gain and integration time were adjusted during the first four clinical cases in order to find optimal values of such camera parameters that allowed capturing autofluorescence signals in the fifth clinical case.

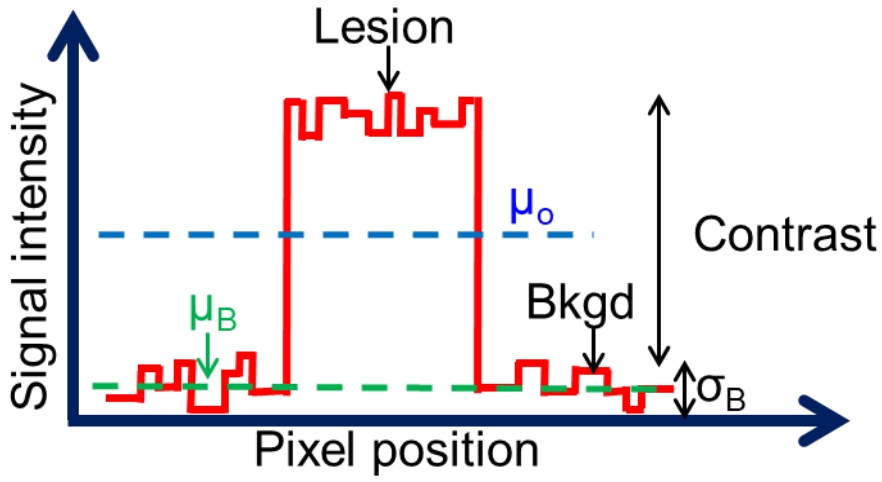

Figure 5-4: The diagram shows that the contrast is the intensity range between the background noise and a signal from an object under study such as a lesion. The lesion is easier to detect when the contrast between lesion and background is clearly higher than the noise variations [145], [146].

5.2 Results

5.2.1 Spatial and spectral calibration

5.2.1.1 Phantoms

To verify if the spectral and spatial calibration algorithm works correctly, the calibration was tested on a flat block that does not emit fluorescence (Figure 5-5A). The first objective was to confirm the usefulness of the spatial correction if it was observed that the illumination was uniform on the flat block after applying the calibration algorithm. The image of Figure 5-5B was taken while the white light of the microscope illuminates the flat structure in reflectance mode; calibration has not been yet applied to this image. After applying the calibration algorithm, the flat block looks uniform throughout the image as seen in Figure 5-5C. Next, the spectral calibration was also tested and since it is known that the flat block does not emit fluorescence, it is expected that, when illuminating the structure with an excitation source at 405 nm and doing image acquisition from 450 to 720 nm, the pixel intensity across the image of the flat block was practically zero. Figure 5-5D shows an image of the flat block under blue excitation where the calibration algorithm has not been yet applied and where it is observed that the section of higher pixel intensities in the image is bleed-through from the excitation source. Figure 5-5E shows that after applying the spectral calibration the pixel intensity throughout the image is nearly zero. After this preliminary experiment, two longpass filters with cut-on at 442 nm (described in section 5.1.1.1) were added to the detection path of the imaging system and the image acquisition was carried out next from 550 nm to 720 nm, because the bleed-through was present at lower wavelengths.

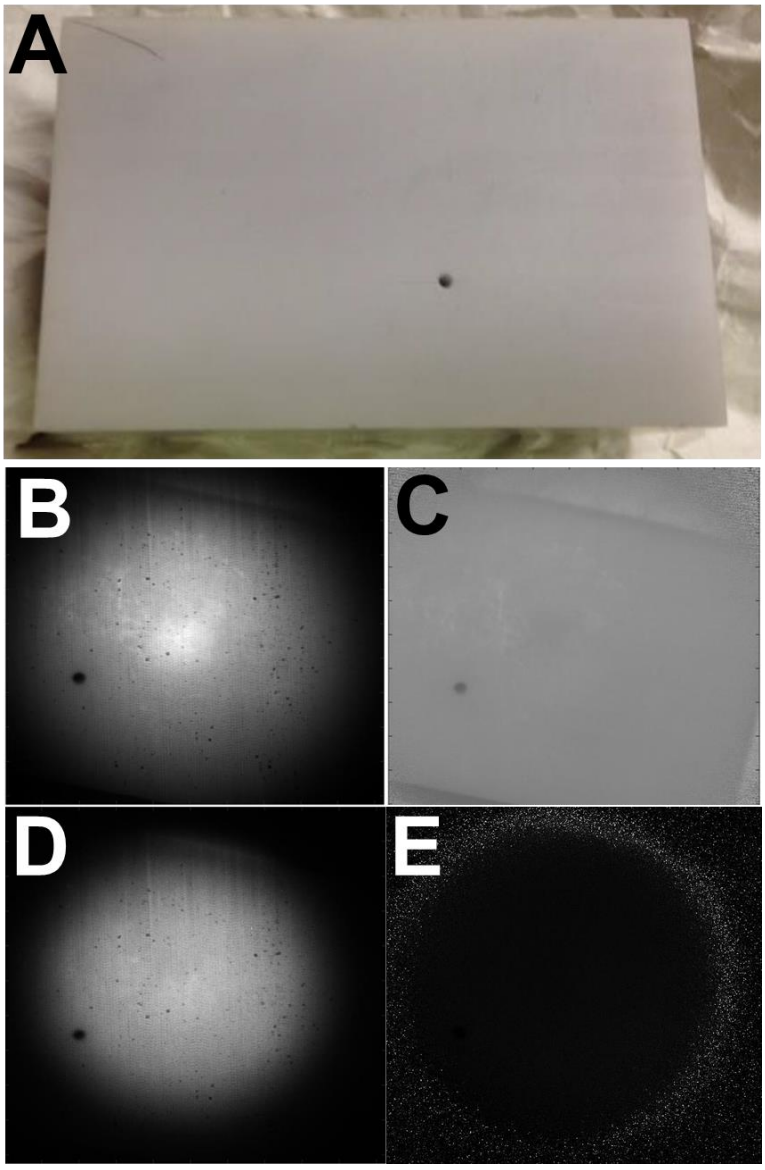

Figure 5-5: (A) Flat block on which the calibration algorithm was tested. (B). Uncorrected image of the flat block under white light excitation. (C) Corrected image of the flat block under white light excitation. (D) Uncorrected image of the flat block under blue excitation. (E) Corrected image of the flat block under blue excitation.

The spatial/spectral calibration algorithm was also tested on a sample of PpIX in a petri dish. The purpose was to observe the emission intensity distributed evenly throughout the PpIX sample after applying calibration. For comparison, Figure 5-6A shows the raw image of PpIX

fluorescence that hasn't been calibrated; and 5-6B shows the calibrated image where the pixel intensities are uniform through the sample. It was also important that the emission spectrum retrieved from hyperspectral images of PpIX (regions of 20 x 20 pixels) showed clearly the main emission peak of PpIX at 635 nm and a second emission at 705 nm. From the literature, it is expected that the main peak has higher intensity than the second one, as it is shown in the blue spectrum of Figure 5-6C once the calibration algorithm has been applied. In the red spectrum of Figure 5-6C, where no calibration has been performed, the amplitude of the peak at 705 nm exceeds the magnitude of the main emission. The RMSE (root-mean-square error) was estimated for the calibrated and uncalibrated PpIX signals with respect to a theoretical spectrum of PpIX [147] shown in black in Figure 5-6C. The RMSE for the PpIX signal that has undergone spectral and spatial calibration is 11%, whereas for the uncalibrated signal it is 22%.

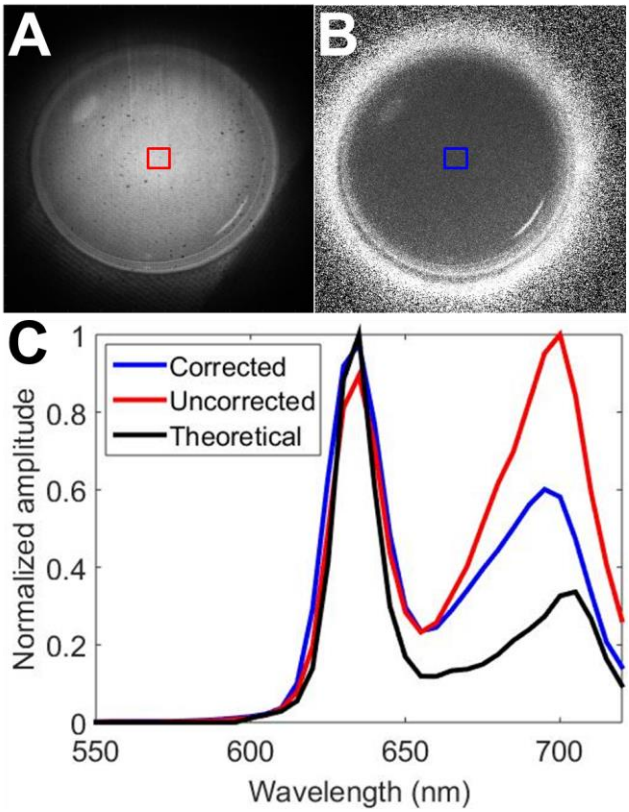

Figure 5-6: (A) Uncorrected image of PpIX in petri dish. (B) Corrected image of PpIX. (C) A theoretical spectrum of PpIX emission together with calibrated and uncalibrated spectra retrieved from regions of 20 x 20 pixels in images of a PpIX sample.

5.2.1.2 Calf brain

The algorithm for spectral and spatial calibration was also tested on a calf brain. Despite the different depths and borders of the brain, the algorithm provided images with uniform pixel intensities throughout the entire brain surface in white light reflectance mode. The large depth of field of the microscope is an important feature to achieve an effective spatial calibration, since it allows seeing well-focused structures at different depths.

Figure 5-7A shows an uncalibrated white light reflectance image of the calf brain; an average spectrum recovered from a region of 20 x 20 pixels (red square) is shown in Figure 5-7B. Next, the calibrated white light reflectance image of the calf brain is presented in Figure 5-7C together with an average spectrum (Figure 5-7D) from the exact same area as before.

The shape of the calibrated spectrum in Figure 5-7D matches white light reflectance spectra of human brain obtained using a wide-field imaging system that has been presented in details in [119]**.**

In addition, in order to smooth the signal, a Savitzky-Glay filter technique was implemented in Matlab. A 3rd order filter with 5 neighboring elements was chosen to smooth the signal without losing broadband spectral features (~50 nm) that are distinctive of autofluorescence signals of brain tissue. The filtered signal can also be seen in Figure 5-7D.

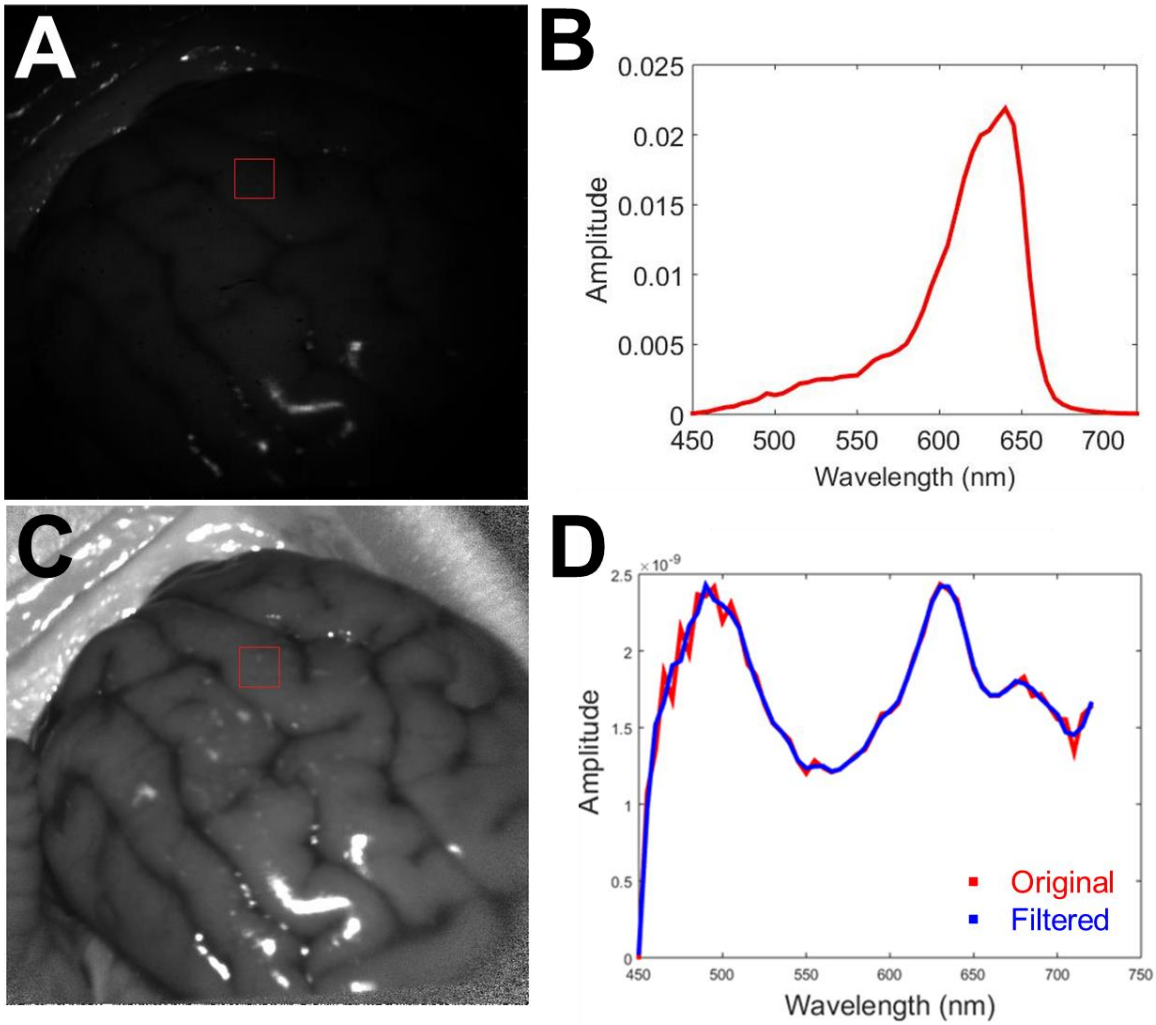

Figure 5-7: (A) Uncalibrated reflectance image of a calf brain. (B) White light reflectance spectrum obtained from the square region in (A). (C) Calibrated image of a calf brain in white light reflectance mode. (D) Filtered reflectance spectrum recovered from the red square in (C).

The spectral and spatial calibration was also performed on fluorescence data of the same calf brain when the tissue was excited with a blue excitation source at 405 nm (Coherent, Inc., CA, USA). Figure 5-8A shows an uncalibrated fluorescence image that represents the sum of fluorescence intensities at every emission wavelength; its spectrum is shown in Figure 5-8B. In addition, the calibrated fluorescence intensities of the calf brain image and its spectrum are presented in Figures 5-8C and Figures 5-8D, respectively. The calibrated fluorescence spectrum

of Figure 5-8D was also filtered with a Savitzky-Golay filter (3rd order, 5 neighboring elements). The shape of the calibrated spectrum matches human brain autofluorescence spectra also presented in [119].

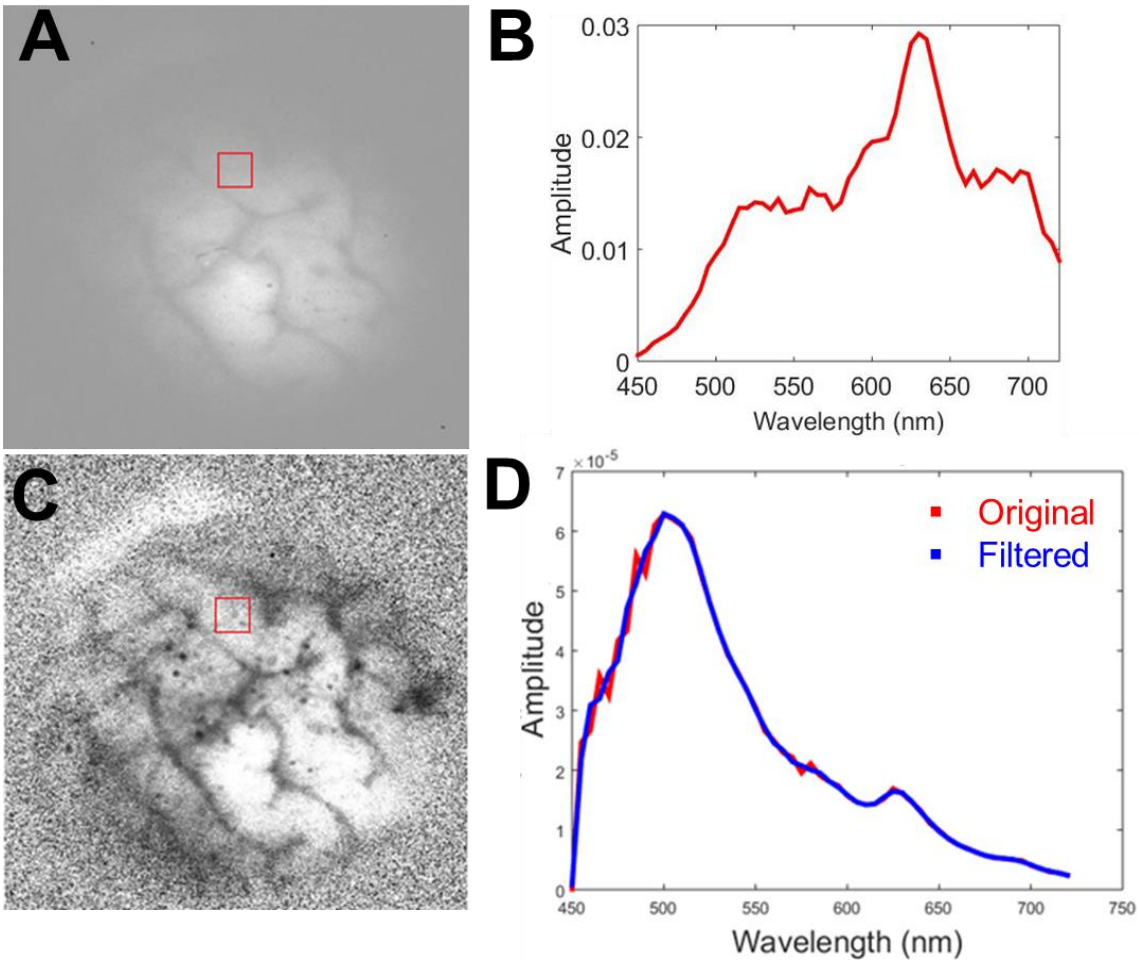

Figure 5-8: (A) Uncalibrated fluorescence image of a calf brain. (B) The average spectrum (20 x 20 pixels) of the red square region in (A). (C) Calibrated fluorescence image of a calf brain. (D) The corresponding spectrum of the square region in (C).

On the other hand, a calf brain sample where gray and white matter is visible was also analyzed. In order to better observe tissue structures, the calibrated reflectance images of the brain were converted into RGB color space, as shown in Figure 5-9A. The fluorescence spectra of gray and white matter are shown in Figure 5-9B; these spectra are taken from regions of 20 x 20 pixels of

images that have already been calibrated spectrally and spatially. The shape of the spectra corresponds with fluorescence spectra of rat brain in single-point probe measurements that have been published in [73]. Additionally, Figure 5-9C shows the corrected white light reflectance spectra of gray and white matter. Overall, in Figure 5-9 it is seen that the intensity of white matter is higher than gray matter for both fluorescence and reflectance measurements, this also agrees with what has been published for brain tissue phantoms in [119].

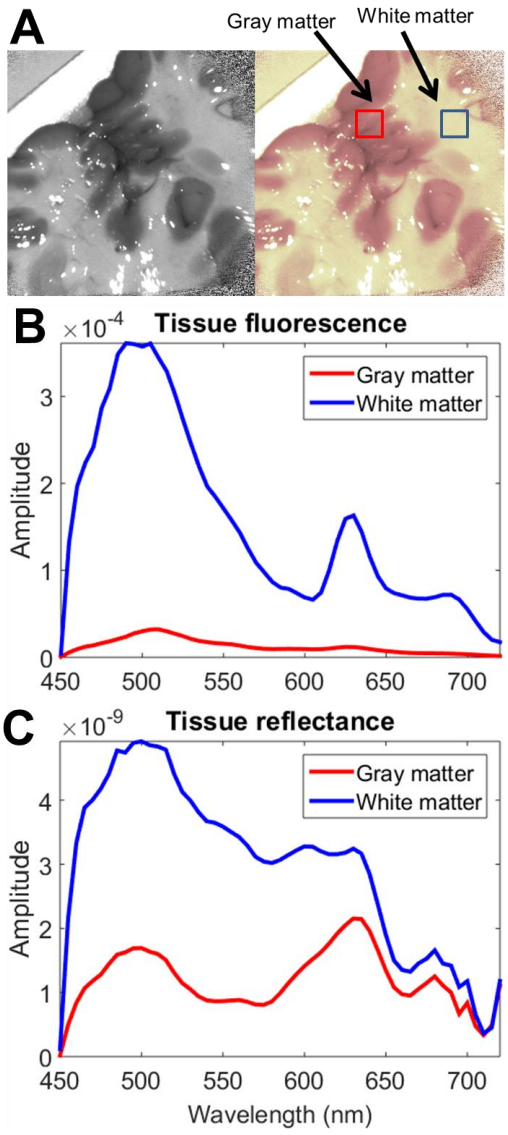

Figure 5-9: (A) White light diffuse reflectance image of white and gray matter in a calf brain and the same image in RGB format. (B) Calibrated fluorescence spectra of white and gray matter. (C) Calibrated white light reflectance spectra of white and gray matter.

5.2.2 Fluorescence quantification algorithm applied to clinical data

The images presented in this section were acquired in an adult patient during a brain cancer surgery on November 9th, 2017 at the Neuro.

Two imaging sessions were planned to acquire images during the surgery: (a) at the beginning, when the tumor is completely exposed; and, (b) at the end, when the tumor has been already removed. To present results more effectively, each stage of the image post-processing is listed below. At each point of the analysis, data is shown first for images taken at the beginning of the surgery, and then for those obtained at the end:

(a) A grayscale image of white light reflectance is obtained and then it is converted into RGB color space, as shown in Figure 5-10A and Figure 5-10D for images from the beginning and end of the surgery, respectively.

(b) An overlay of recovered fluorescence (green) on a white light reflectance image is presented in Figure 5-10B (for the beginning of the surgery) and in Figure 5-10E (for the end). This overlay is useful to identify structural information of the tissue that is being resected and identify where the fluorescence signal originates from.

(c) The tissue autofluorescence intensity that was detected in each imaging session is shown in a wide-field image, together with a graph of spectral signatures at nine specific locations in all the tissue. The spectral signatures that are presented are the averaging of spectra retrieved from sections of 20 x 20 pixels. Figure 5-10C shows the tissue autofluorescence detected at the beginning of the surgery and Figure 5-10F at the end.

The shape of autofluorescence emissions of brain tissue shown in the range from 550 to 720 nm in Figure 5-10 (C and F) are consistent with autofluorescence spectra obtained in human brain by an optical fiber probe in [96]. Also, the results in Figure 5-10 suggested that autofluorescence intensity from tumor detected at the beginning of the surgery is lower than after tumor resection (end of the surgery); similar to Poulon et al. [4] who reported that fluorescence is more intense in normal tissue than in nervous system tumors.

Moreover, all the spectral signatures of corrected fluorescence shown in Figure 5-10, from the beginning and end of the surgery, were also analyzed one by one in Appendix C; it means that

additional signals were generated for each of the nine interrogation points in the tissue. These signals are: (a) the raw fluorescence and (b) white light reflectance, already spectrally and spatially calibrated. Then, the fluorescence normalization algorithm performs a correction for the signal attenuation due to absorption and scattering in tissue by combining the raw fluorescence and white light reflectance spectra and this provides the spectral signature for (c) corrected fluorescence.

Finally, the same analysis described in this section for the detection and subsequent correction of autofluorescence by means of white light reflectance images was performed also for images of the Spectralon at nine different locations on the Spectralon surface. As the Spectralon is a 99% diffuse reflectance standard, it reflects almost all the blue excitation light; and it can be a means of knowing the contribution of the bleed-through from the excitation source (in the range from 550 to 720 nm) on the autofluorescence signal detected *in vivo* in brain tissue. As it can be seen in Figure C-1 of Appendix C, the intensity of the bleed-through is very low (comparatively with the autofluorescence signal intensity retrieved from human brain tissue) and its shape is almost flat throughout the spectrum, meaning that its intensity is almost constant through all the wavelengths, so it does not contribute to significantly change the shape or intensity of the tissue autofluorescence signal.

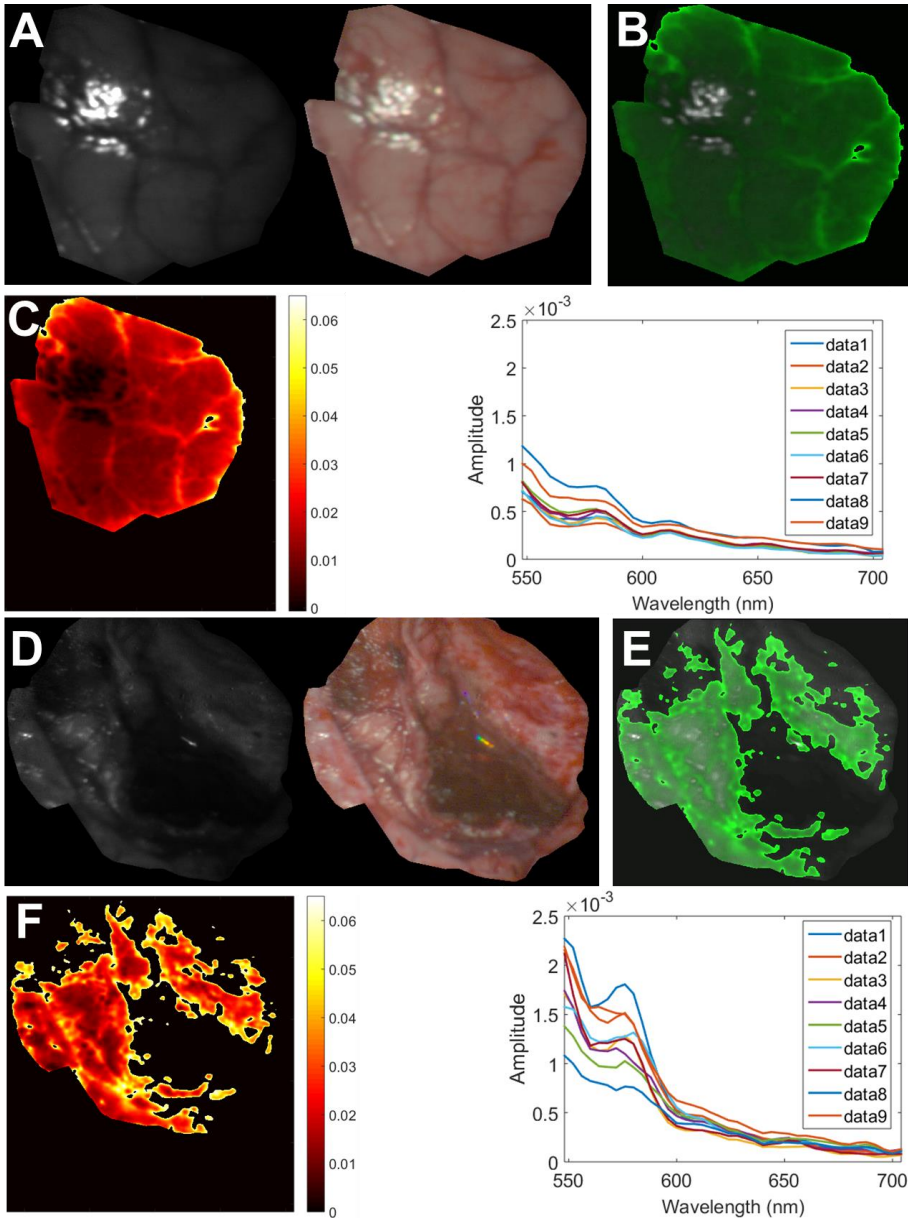

Figure 5-10: (A) Grayscale reflectance image when tumor is exposed at the beginning of the surgery (left) and its corresponding RGB image. (B) Overlay of autofluorescence (green) and white light reflectance recovered at the beginning of the surgery. (C) The tissue autofluorescence recorded at the beginning of the surgery is highlighted in red (left) and nine corrected autofluorescence spectra are displayed from different locations all over the highlighted area. (D) Grayscale reflectance image of brain tissue after tumor has been removed at the end of the surgery (left) and the same image converted into RGB. (E) Overlay of autofluorescence and white light reflectance detected at the end of the surgery. (F) Nine corrected spectra obtained at

different points in the red-colored area (at the left) indicating the autofluorescence signature of tissue at the end of the surgery.

5.2.3 Contrast-to-Noise Ratio (CNR)

The CNR was calculated in Matlab for tissue autofluorescence images (brain tissue under blue illumination) to evaluate the autofluorescence contrast of tumor and non-tumor tissue with respect to a background with no fluorescence. The images were recorded during the two imaging sessions of a clinical case at the Neuro, during which autofluorescence was detected *in vivo* by the imaging system presented in this thesis.

The CNR was assessed following Eq. 5-4**,** presented in section 5.1.6. Figure 5-11A shows an image from the beginning of the surgery with nine selected areas (blue); these areas are located within a section representing tumor where the target autofluorescence signal was detected. Figure 5-11A also shows a section indicating the background of the image (red) where no autofluorescence is present. Similarly, in Figure 5-11B it is shown a background area (red) in addition to nine more data points within the tumor resection cavity (blue) after the tumor has been removed, thus, it is suggested that the latter are non-tumor areas. All the selected areas cover 20 x 20 pixels.

The calculation of the CNR was performed for single images (Figure 5-11A and Figure 5-11B) that were the sum of the total fluorescence at all wavelengths, where dark counts had been already extracted at each wavelength and each frame had been normalized by camera gain and integration time. It was evaluated that intrinsic fluorescence at the beginning of the surgery was detected in image regions with an average CNR ~22.6 (STD = 2.2). In contrast, the average CNR of the nine selected regions for the image acquired at the end of the surgery was ~30.1 (STD = 7.1).

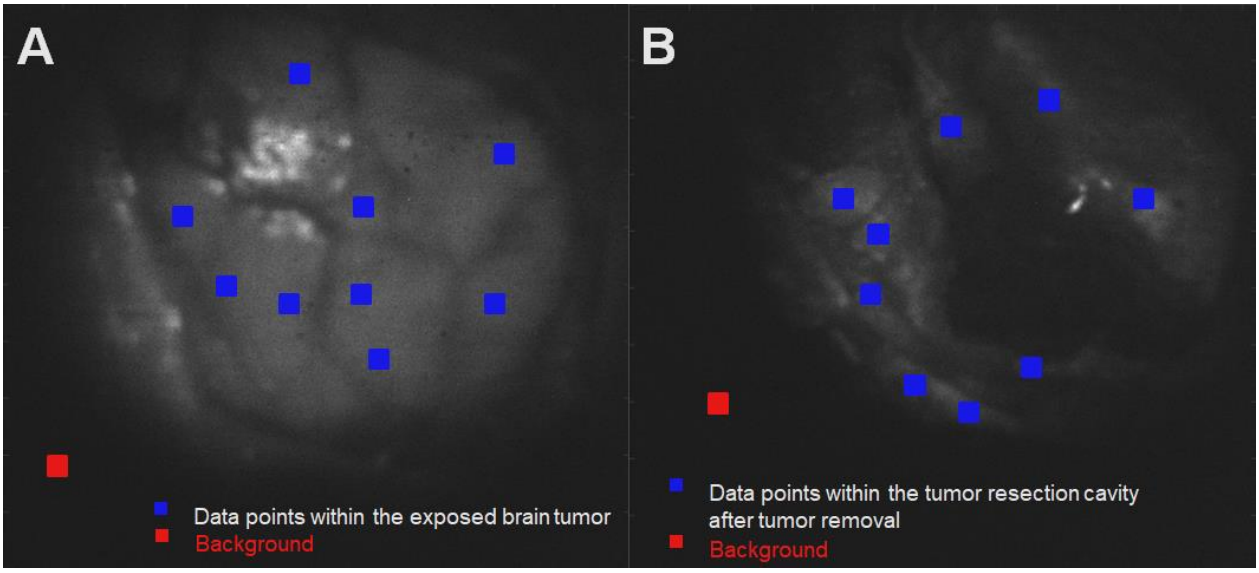

Figure 5-11: Images representing the sum of fluorescence intensities at all wavelengths from which areas representing lesions (blue squares) and backgrounds (red) were selected for the calculation of the CNR. (A) Image from the beginning of the surgery with tumor exposed. (B) Image from the end of the surgery after tumor removal.

CHAPTER 6 DISCUSSION

The overall objective of this project was to develop an imaging system to perform two main tasks through a commercial neurosurgical microscope without modifying the microscope setup: (a) profilometry and, (b) detection of brain tissue autofluorescence. The first objective was achieved by mounting a system, comprising a Digital Light Projector and an imaging fiber bundle, onto the stereovision port of the microscope that is designed to allow the surgeon to have depth perception. In summary, the DLP projects sinusoidal intensity patterns on the brain surface and an image is detected with the fiber optic imaging bundle; the projector and fiber bundle are both connected to microscope eyepieces. An algorithm is then implemented leading to 3D surface reconstruction. For the second objective, a liquid crystal tunable filter was used to detect light reemitted from the brain at several wavelengths to detect the spectral signature of the tissue on a pixelized basis on a scale up to several centimeters. Many different components were designed, assembled and characterized at several stages of the project in a complex optical, electrical and mechanical system that needed to be integrated into the surgical microscope. In this chapter the main experimental results of the thesis are summarized with an emphasis on the limitations of the new imaging system and opportunities for future improvements.

6.1 Profilometry

Depending on the profilometry method of choice, either three or four fringe patterns are projected with different phases to obtain a 3D representation of an object. However, for methods based on three phases, three reference images associated with a flat surface have to be acquired. In contrast, using a method based on four phase shifts avoids having to acquire reference images. Because of the difficulties associated with acquiring reference images during surgical procedures, this technique was adopted for this project.

6.1.1 Profilometry measurements at different heights

The profilometry method was evaluated using pyramid-shaped phantoms with steps at different heights varying from 1.5 to 30 mm, ensuring the phantoms are within the 4-cm depth of field of the neuromicroscope. The reconstructions were made by projecting sinusoidal fringe patterns

with frequencies of 4 to 7 sinusoidal periods along a length of 4 cm, corresponding to a range of spatial frequencies from 1 to 1.75 cm^{-1}. These frequencies were chosen in order to be sensitive to small and large step changes because low spatial frequencies ($\leq$ 1 cm^{-1}) were demonstrated to efficiently reconstruct larger tissue features, whereas higher frequencies provide finer details [30].

The accuracy and precision of depth reconstruction measurements were evaluated reconstructing the phantoms with focal length and zoom settings commonly used in surgery (focal length = 300 mm; minimum zoom = 1X). Based on the phantom work, the profilometry technique was demonstrated to have an average accuracy of 0.3 mm and a precision of 0.6 mm. As stated in chapter 1, following the work presented in this thesis 3D profilometry will be used in the Laboratory of Radiological Optics as prior information in a tissue light transport model for computing tissue optical properties, including scattering and absorption, during neurosurgical procedures. The 0.3 mm reconstruction accuracy obtained with the system is comparable with resolutions attained with techniques developed by other groups for similar biomedical applications. For example, Gioux et al. applied a geometric correction to estimate the precise values of scattering and absorption coefficients that were used as surrogates for tissue physiological status [30]. The range of errors in depth measurements they obtained was at ~1 mm. This level of accuracy was demonstrated to be sufficient to improve computation of tissue optical properties since the geometric correction induced up to 10 fold changes in light signals. Another profilometry system was seamlessly integrated onto the Zeiss Pentero neuromicroscope [18]. It consists of two cameras connected to the stereovision port of the microscope. This system is used to correct for brain shift deformation that occurs after opening the dura. The depth estimation error of this system is also ~1 mm, which is considered acceptable since brain deformation (between pre-operative MRI and post-dura opening) has been reported to be up to 1 cm and sometimes even more [18].

While the 3D reconstruction accuracy and precision might stay at values close to 0.3 mm and 0.6 mm, respectively, for different microscope magnifications, changes should be expected since zoom settings impact the size and the period of the projected patterns. To determine the accuracy and precision of reconstructions for other pairs of zoom and focal length, the same experiments presented in this thesis should be repeated. During a neurosurgical procedure,

surgeons often need to change those settings and move the microscope relative to the surgical cavity. To perform 3D reconstructions at arbitrary zoom and focal length settings and get the real object dimensions in centimeters, Ji et al. [135] obtained two calibration curves (each curve for individual adjustments of zoom and focal length) used to implement pixel scaling on a input reference image. They found that image deformation is due to the change of each microscope setting individually (either zoom or focal length); for example, this means that image deformation due to a change in magnification does not depend on the set value of focal length. The two curves provide pixel scaling ratios for each zoom and focal length value. The pixel scaling is performed using a reference image of the sample; this image is taken at a pre-set zoom and focal length that produce an image of the sample with known dimensions. Finally, the reference image is divided by the multiplication of both pixel scaling factors. The through-microscope profilometry system presented in this thesis could directly use the calibration curves presented by Ji et al. because they were specifically estimated for Zeiss Pentero surgical microscopes, such as the ones used in this project.

An important finding of this thesis is that a single mode laser coupled with a single mode fiber – instead of a multimode source – impacts the reconstruction accuracy. The height experiment with the pyramid phantoms was repeated using the same microscopy setup but with a multimode illumination source. It was found out that the average relative error in the reconstructions with a multimode source increases to 10% (3D reconstruction accuracy ~1 mm) comparatively with an error of 3% (3D reconstruction accuracy ~0.3 mm) obtained with a single mode source.

6.1.2 Profilometry measurements at different angles

When areas of an object are associated with a slope that is too steep (large curvature), the light trajectories may prevent the acquisition of a projected fringe pattern covering the whole surface. In other words, regions of shadows are present in the images and they do not contain information related to the geometry of the object, causing reconstruction errors. To assess the impact of this phenomenon and to quantify errors in depth recovery, an experimental protocol was developed for allowing the surface of an object to be imaged at different angles with respect to the microscope head. Briefly, 3D reconstructions of the surface of a flat platform positioned at

different angles were carried out. In the same way as for the height measurement experiment, the spatial frequencies used were in the range of 1-1.75 cm^{-1}. The platform was rotated at ±15°, ±30° and ±45° around the *x*-axis, as well as by the same tilt angles but this time around the *y*-axis. The reconstruction error for all angles was no more than 2° (~1.5 mm) lending support to the idea that accurate surface reconstruction can still be attained in a surgical environment when imaging surgical cavities with a certain degree of curvature. Within the error obtained it must be considered that the platform itself has a precision error at each inclination setting of approximately ±0.3° [148].

6.1.3 Tissue-like phantom measurement

A brain-shaped tissue simulating phantom with absorption and scattering values within the physiological range of optical properties of the brain was reconstructed. However, in order to reconstruct surfaces, the sine-wave patterns deformed by the shape of a sample must be perceived with enough contrast, *i.e.*, the difference between the maximum and minimum intensities in the fringe pattern should be sufficiently high as to have easily distinguishable patterns. However, the object surface reflectance properties can vary greatly depending on geometric differences and textural features [149]. Thus, the contrast of the fringes can be low when there is irregular reflection from a non-uniform reflecting surface, hindering the 3D reconstruction of an object [150]. In consequence, despite the fact that the brain-shaped phantom was 3D reconstructed correctly, it could be the case that the patient brain surface presents large variations in reflectance, producing low contrast fringes, and making 3D reconstruction difficult.

6.2 Tissue autofluorescence

6.2.1 Spatial and spectral calibration

After verifying that there is a linear relationship between the recorded pixel intensity with integration time and camera gain, the intensity of hyperspectral images was normalized by dividing it by integration time and gain. In addition, the intensity differences in the spatial distribution of the excitation beam were also corrected, as well as the depth differences in the brain surface by carrying out a process of spectral and spatial calibration to correct the

fluorescence and reflectance spectra pixel-by-pixel. The regions of the image that present specular reflections were not useful for the analysis of the fluorescence signal given that specular reflections appear as a group of bright pixels associated with regions of the camera being saturated. The spatial resolution of the imaging system was calculated as 198 μm with a USAF 1951 resolution target; this value is considered to be adequate for the visualization of a tumor on macroscopic scale [119].

6.2.2 Fluorescence normalization technique

An algorithm was also developed and tested for the correction of autofluorescence spectra by combining autofluorescence and white light diffuse reflectance images. This method limits the influence of tissue absorption and scattering contrast associated with non-fluorescent tissue molecules, ensuring the processed signal is intrinsic to fluorescent tissue molecules [151]. However, further testing than what was achieved in this thesis would be necessary to quantify the accuracy of the fluorescence normalization algorithm. This could be done through carefully planned optical phantom experiments [88]. For instance, Gebhart et al. [119] fabricated phantoms to simulate absorption, scattering and autofluorescence values associated with white matter, gray matter and glioma tissue. The absorption and scattering values were taken from [152] and the autofluorescence intensities were mimicked by specific concentrations of a fluorescent dye (Stilbene 420, Exciton); such concentrations were estimated after measuring the fluorescent dye and the autofluorescence of brain tissue with the same optical spectroscopy probe [96]. Alternatively, the fluorescence normalization algorithm could also be tested on phantoms made of Protoporphyrin IX (PpIX) [153]. These phantoms would contain specific concentrations of PpIX to provide fluorescent contrast, intralipid as the optical scattering agent and synthetic hemoglobin or food coloring dye as the absorber. By knowing the specific PpIX concentrations in every phantom, linear calibration curves could be produced representing the real PpIX concentrations with respect to predicted PpIX concentrations computed using the normalization algorithm. R^2 values could then be computed to evaluate the strength of the linear association between estimated and real PpIX concentrations. In addition, the standard deviation of detected PpIX concentrations for phantoms with a single concentration of PpIX and different absorption and scattering coefficients can be calculated. The above-mentioned statistical

parameters could provide a measure of the performance of the fluorescence normalization algorithm.

The fluorescence normalization algorithm was tested *in vivo* using human data acquired during a brain cancer surgery at the Neuro in the scope of a proof-of-concept clinical study designed to evaluate whether or not the system could acquire autofluorescence maps through the neurological microscope. Even if in the literature there is a lack of information about autofluorescence of human brain tissue and more clinical research is needed to characterize the autofluorescence signature of brain in healthy and diseased states [4], overall, the autofluorescence spectral shape of brain tissue (shown in this thesis from 550 to 720 nm) obtained using the normalization algorithm coincides with past work by another group [96]. However, in this other study, spectra were obtained using a fiber optic probe for single point fluorescence measurements and the excitation light delivered to the tissue was at 337 nm (ultraviolet). In our work, excitation was at 405 nm (violet) and fluorescence spectra were computed at each pixel on images acquired with a wide-field microscope. Also, results presented in this thesis showed that tissue autofluorescence collected at the end of the surgery (after tumor removal) had higher intensity compared to the autofluorescence in the tumor (beginning of surgery, after dura opening). This is also consistent with the literature, in which it is suggested that fluorescence intensity is higher in normal tissue than in central nervous system tumors [4].

Finally, this algorithm can eventually be used to compare fluorescence intensities of brain regions in a group of patients to be able to develop statistical models differentiating cancerous from healthy tissue.

6.2.3 Evaluation of contrast-to-noise ratio during neurosurgical procedures

In vivo data acquisition was achieved during five brain cancer resection surgeries as part of a proof-of-concept study aiming to demonstrate intrinsic brain fluorescence can be detected using the hyperspectral imaging system. Data acquisition was done in two imaging sessions during each clinical case and each imaging session was conducted within a two-minute time lapse. Out of the five clinical cases, the first four were used to optimize acquisition parameters (integration time, camera gain) and brain autofluorescence could be detected in the fifth case using the optimized parameters.

The CNR was calculated on two intraoperative fluorescence images from the beginning and end of the surgery, respectively. On an image taken at the beginning of the surgery, the CNR calculation was based on the selection of nine areas representing tumor with autofluorescence, and a background area outside the tumor with no autofluorescence. For the end of the surgery, when the tumor has been already removed, the targeted sections were nine areas with autofluorescence signal (presumably representing non-tumor tissue) in the tumor resection cavity and a background area outside the resection cavity. The average CNR value of the nine selected data points in each image was calculated and it was equal to 22.6 (STD = 2.2) for autofluorescence contrast detected at the beginning of the surgery and 30.1 (STD = 7.1) for autofluorescence detected after tumor resection. However, more clinical results are needed in order to set a CNR threshold value for detectability of autofluorescence in tumor and non-tumor image regions. It is hypothesized that image areas with lower CNR than a calculated threshold value wouldn't provide the contrast needed for autofluorescence detection. That is why in each clinical case the integration time and camera gain must be adjusted to achieve optimized CNR. However, this task is very difficult because even if the main operating room lights are off, illumination from other light sources (lamps, screens and light from multiple medical devices) appear in the images. And so, increasing the gain and camera integration time would also increase the level of light on the camera sensor coming from unwanted light sources, causing saturation (producing bright regions in the image) and limiting the dynamic range of measurement. Thus, the CNR is influenced by the level of background light in the operating room, which varies with the medical devices that are in use and the different operating rooms.

Finally, another factor affecting CNR is the amount of blood that is present in the brain surface during surgery, which causes the attenuation of the excitation light delivered to the sample and the loss of autofluorescence signal reaching the surface of the tissue.

6.3 Limitations of the imaging system and possible improvements

Among the most important limitations of the profilometry setup is that there is a 98% light loss in the system, mostly due to the very small aperture size of the microscope lenses. This is why the typical illumination power that can reach the brain surface is very low. In fact it was measured to be approximately 85 $\mu W/cm^2$ under maximum illumination power at 638 nm and a working

distance of 30 cm. This can yield images with low SNR especially for large absorption and reduced scattering coefficients, which can influence significantly the performance of the phase-shifting profilometry algorithm.

Moreover, the uniformity of the projected image depends on the collimation of the beam that illuminates the DMD chip of the projector, which impacts the depth accuracy of the profilometry system. In this thesis a red laser was chosen because it led to less divergence while passing though the different optical components of the projector when compared to shorter wavelengths in the visible range. Inside the projector there are several optical elements made of glass; glass has a larger index of refraction at lower wavelengths, so red induces less divergence since it is the longest visible wavelength. This means that the quality of the laser beam collimation within the projector depends on the wavelength; and the depth accuracy of the profilometry system may be lower if the projector is coupled with different visible colors of laser light. In addition, the percentage of light losses through the whole imaging system might also vary depending on wavelength, given that the low apertures of the microscope would constrain the passage of more divergent light.

The main limitation of the system for brain autofluorescence imaging is that although the LCTF can capture information starting at 400 nm, the current system configuration can only acquire the tissue autofluorescence signature in the 550-720 nm range. The reason is that the excitation bleed-through (leakage of the microscope excitation source into the captured signal) in the 400-550 nm range is larger than the intensity of detectable autofluorescence. The tissue autofluorescence information lost in this range is the emission of NADH and flavin. However, from 550 nm to 720 nm, the chromophores that contribute to the observed fluorescence signal are: lipopigments, porphyrins and chlorins. Ideally, one or two bandpass or lowpass excitation filters (attenuation > 6 OD), would be placed into the excitation light path of the microscope blue light. The filter would pass light below 410 nm allowing to reduce bleed-through to enable NADH and flavin detection [4]. However, it was found out that, both, the blue and white light exit from the same port of the microscope. These new filters would complement the two longpass filters (cut-on frequency at 442 nm) that were already added to the detection path of the imaging system, specifically in the interior of the imaging bundle adapter. The changes would make possible to implement new techniques to analyze the autofluorescence spectrum and identify each

of the main fluorophores in the brain. For example, calculating the integral under the curve of the emission peaks of NADH, flavin and porphyrin in the autofluorescence spectrum [73] could provide reduction-oxidation and optical index ratios that in the past served to distinguish between cancer and normal cells [4], [98], [154].

On the other hand, it would be desirable for an improved version of this imaging system software to ensure optimal SNR and CNR values can be obtained through auto-adjustment of gain and integration time while avoiding camera saturation.

In addition, it could also be useful to compare the fluorescence normalization technique that was developed in this thesis with other autofluorescence correction techniques employing white light diffuse reflectance to correct for the non-fluorescent tissue optical properties. For instance, reference [119] shows it is possible to differentiate normal brain from tumor tissue from the calculation of a threshold value obtained from the ratio between the fluorescence emission at 460 nm and the diffuse reflectance emission at 700 nm. The justification of the choice of wavelengths is that hemoglobin absorbs much more light in the blue and green region (400-600 nm) compared to the red region (600-720 nm); and it was claimed that the intensity ratio between these two regions can provide a relative measure of the absorption of blood. However, an algorithm for discrimination of brain tumor and tumor margins that considers only information at a few wavelengths that correspond to peaks or valleys of the spectrum has the disadvantage of not including all the information of fluorescence and reflectance spectral signatures [95]. If all the information of fluorescence and reflectance spectra could be taken into account, the combination of data about, for instance, the slope of the curve, the area under the curve and the intensity of the peaks through the entire optical spectrum could provide more information to describe the differences between cancerous and healthy tissue [95].

Finally, as more clinical data is collected with the imaging system, it will be necessary to validate the imaging data with histopathology test results. The gold standard to evaluate the usefulness of an imaging agent for the diagnosis of a disease is the histological analysis by means of H&E (hematoxylin and eosin) staining. However, pathological evaluation of tumor samples through fluorescence measurements is subject to multiple errors [155]–[157]. For example: when it cannot be confirmed that fluorescence is being expressed in a small tumor region within a large volume of tissue, the small fluorescent tumor region could easily go unnoticed as it is not

possible to sample the whole volume. Even if a relatively small tumor biopsy of 1 cm^2 is taken, it would take 2500 cuts to have 4 µm sections, which can be completely impractical [158]. A Raman spectroscopy probe [159] that was developed in the Laboratory of Radiological Optics is currently used in clinical cases at the Neuro to differentiate between cancer and normal tissue. During a clinical case, when a Raman probe measurement is obtained, a biopsy sample is taken from the same tissue interrogation site. Thus, in this thesis it is proposed that when biopsy samples are collected for histopathological analysis, an image of the Raman spectroscopy probe in the microscope field of view is taken with the imaging system presented in this thesis. This would help to relate the location of a biopsy with pixels in the brain image. Nevertheless, during this project, it wasn't possible to do a correlation between Raman and autofluorescence measurements because more clinical cases are necessary in order to obtain more data.

6.4 Future applications

An additional application for the fluorescence imaging system presented in this thesis is the possibility of detecting exogenous fluorescence markers linked with molecules (*e.g.* antibodies, peptides) with high affinity to proteins over-expressed in cancer cells. Each fluorophore can provide different information about the tissue characteristics to determine the extent of cancer [24]. For instance, Indocyanine Green is widely used in angiography to trace arteries and veins [72], and in tumor brain surgery it can help to look more easily at veins and highly vascularized tumors [160]. To excite a particular fluorophore, a fiber-coupled high-power laser diode at a fixed wavelength could be connected to the projector to replace the current illumination source.

On the other hand, spatial frequency domain images (SFDI) can provide a quantitative estimate of absorption and scattering coefficients to be able to correct the intensity of fluorescence images to afford quantification of fluorophore concentrations during brain surgery [161]. With the existing configuration of the through-microscope phase-shifting profilometry system presented here, sinusoidal patterns of variable spatial frequency and phase could be projected to determine μ_a and μ'_s coefficients through the SFDI technique [42]. Under the assumption that the optical properties set the degree of image blurring at a specific spatial frequency, Monte-Carlo simulations of image analysis and the standard diffusion theory [162] can be used to extract the absorption and diffusion coefficients. Next, these values are used in the

qFI (wide-field quantitative fluorescence imaging) model reported in [161] to quantify the intensity of fluorescence images.

Alternatively, with optical property values recovered pixel-by-pixel in an image, scattering maps of tissue could be created, as demonstrated by Kanick et al. [163]. Since scattering is related to tissue structure at the cellular level, *i.e.*, the size and shape of cellular components, it is suggested that a change in the structural characteristics of tissue impacts on the degree of scattering [164]–[171]. Moreover, scattering spectroscopy has already been used in cancer diagnosis [172]–[176] and to identify tumor margins in surgical procedures [177]–[179].

CONCLUSION

This thesis was dedicated to the design, fabrication and testing of a new wide-field spectroscopic imaging system that is seamlessly integrated onto a neurosurgical microscope. The new system is capable of obtaining through-microscope 3D surface reconstructions and to detect the intrinsic fluorescence and diffuse reflectance of brain tissue.

In order to perform profilometry measurements and detection of intrinsic fluorescence, each of the optical and mechanical components of the system were designed, assembled and characterized. In addition, software was developed for visualizing and saving hyperspectral images in real time and to project fringe patterns. In summary, a projection module (consisting of a DLP) and a detection module (including an imaging bundle with a high sensitivity EMCCD and a LCTF) were coupled to separate optical paths of the binocular structure of the neuromicroscope used to provide the surgeon with stereoscopic depth. Spatially-modulated patterns of 4 by 3 cm were projected in the microscope field of view to carry out 3D reconstructions of calibration objects of known dimensions; and the accuracy of 3D surface reconstructions with the system was estimated to be 0.3 mm (precision = 0.6 mm). In addition, a solid phantom simulating the optical properties of human brain tissue was also well reconstructed.

This hyperspectral setup was then used for recording and displaying the autofluorescence signature of brain tissue; first, from animal tissue, where gray and white matter showed different fluorescence intensities. Then, *in vivo* testing was performed on patients with a brain tumor during neurosurgical procedures at the Montreal Neurological Institute and Hospital. The data

were obtained during two imaging sessions in each clinical case to compare the fluorescence intensity in tissue at the beginning and at the end of the surgery. Each imaging session lasted two minutes, without significantly affecting the course of the surgery. The spectral shape of brain autofluorescence was obtained pixel-by-pixel with a fluorescence normalization algorithm developed during this PhD. This algorithm corrects the light attenuation on the images caused by the tissue optical properties. Preliminary image data suggested that the intrinsic fluorescence intensity in tissue is lower at the beginning of the surgery, when tumor is fully exposed, compared to the fluorescence intensity at the end of the surgery when tumor has been extirpated.

Finally, this setup will soon be used in a series of brain cancer surgeries at the Neuro to create 3D maps of the tissue surface containing information of tissue autofluorescence; and later, to extract and geometrically correct the brain optical properties. The imaging system also has the potential to detect some other fluorophores and to quantitatively assess their concentrations which could improve cancer detection during brain tumor surgeries in the near future.

BIBLIOGRAPHY

[1] P. Y. Wen and S. Kesari, “Malignant gliomas in adults.,” *N. Engl. J. Med.*, vol. 359, no. 5, pp. 492–507, Jul. 2008.

[2] L. M. DeAngelis, “Brain tumors.,” *N. Engl. J. Med.*, vol. 344, no. 2, pp. 114–123, Jan. 2001.

[3] M. L. Bondy, M. E. Scheurer, B. Malmer, J. S. Barnholtz-Sloan, F. G. Davis, D. Il’yasova, C. Kruchko, B. J. McCarthy, P. Rajaraman, J. A. Schwartzbaum, S. Sadetzki, B. Schlehofer, T. Tihan, J. L. Wiemels, M. Wrensch, and P. A. Buffler, “Brain tumor epidemiology: consensus from the Brain Tumor Epidemiology Consortium.,” *Cancer*, vol. 113, no. 7 Suppl, pp. 1953–1968, Oct. 2008.

[4] F. Poulon, H. Mehidine, M. Juchaux, P. Varlet, B. Devaux, J. Pallud, and D. Abi Haidar, “Optical properties, spectral, and lifetime measurements of central nervous system tumors in humans,” *Sci. Rep.*, vol. 7, no. 1, p. 13995, 2017.

[5] W. Stummer, U. Pichlmeier, T. Meinel, O. D. Wiestler, F. Zanella, and H.-J. Reulen, “Fluorescence-guided surgery with 5-aminolevulinic acid for resection of malignant glioma: a randomised controlled multicentre phase III trial.,” *Lancet Oncol.*, vol. 7, no. 5, pp. 392–401, May 2006.

[6] F. K. Albert, M. Forsting, K. Sartor, H. P. Adams, and S. Kunze, “Early postoperative magnetic resonance imaging after resection of malignant glioma: objective evaluation of residual tumor and its influence on regrowth and prognosis.,” *Neurosurgery*, vol. 34, no. 1, pp. 41–45, Jan. 1994.

[7] F. G. 2nd Barker, M. D. Prados, S. M. Chang, P. H. Gutin, K. R. Lamborn, D. A. Larson, M. K. Malec, M. W. McDermott, P. K. Sneed, W. M. Wara, and C. B. Wilson, “Radiation response and survival time in patients with glioblastoma multiforme.,” *J. Neurosurg.*, vol. 84, no. 3, pp. 442–448, Mar. 1996.

[8] M. Lacroix, D. Abi-Said, D. R. Fourney, Z. L. Gokaslan, W. Shi, F. DeMonte, F. F. Lang, I. E. McCutcheon, S. J. Hassenbusch, E. Holland, K. Hess, C. Michael, D. Miller, and R. Sawaya, “A multivariate analysis of 416 patients with glioblastoma multiforme: prognosis, extent of resection, and survival.,” *J. Neurosurg.*, vol. 95, no. 2, pp. 190–198, Aug. 2001.

[9] U. Pichlmeier, A. Bink, G. Schackert, W. Stummer, and the A. L. A. G. S. Group, “Resection and survival in glioblastoma multiforme: An RTOG recursive partitioning analysis of ALA study patients,” *Neuro. Oncol.*, vol. 10, no. 6, pp. 1025–1034, Dec. 2008.

[10] W. Stummer, H.-J. Reulen, T. Meinel, U. Pichlmeier, W. Schumacher, J.-C. Tonn, V. Rohde, F. Oppel, B. Turowski, C. Woiciechowsky, K. Franz, and T. Pietsch, "Extent of resection and survival in glioblastoma multiforme: identification of and adjustment for bias.," *Neurosurgery*, vol. 62, no. 3, pp. 564–576, Mar. 2008.

[11] C. J. Vecht, C. J. Avezaat, W. L. van Putten, W. M. Eijkenboom, and S. Z. Stefanko, "The influence of the extent of surgery on the neurological function and survival in malignant glioma. A retrospective analysis in 243 patients.," *J. Neurol. Neurosurg. Psychiatry*, vol. 53, no. 6, pp. 466–471, Jun. 1990.

[12] B. W. Pogue, S. Gibbs-Strauss, P. A. Valdes, K. Samkoe, D. W. Roberts, and K. D. Paulsen, "Review of Neurosurgical Fluorescence Imaging Methodologies.," *IEEE J. Sel. Top. Quantum Electron.*, vol. 16, no. 3, pp. 493–505, May 2010.

[13] R. F. Schmidt and W. D. Willis, Eds., "Neuronavigation," in *Encyclopedia of Pain*, Berlin, Heidelberg: Springer Berlin Heidelberg, 2007, p. 1285.

[14] R. L. Galloway, R. J. Maciunas, and C. A. Edwards, "Interactive image-guided neurosurgery," *IEEE Trans. Biomed. Eng.*, vol. 39, no. 12, pp. 1226–1231, 1992.

[15] P. D. LeRoux, T. C. Winter, M. S. Berger, L. A. Mack, K. Wang, and J. P. Elliott, "A comparison between preoperative magnetic resonance and intraoperative ultrasound tumor volumes and margins.," *J. Clin. Ultrasound*, vol. 22, no. 1, pp. 29–36, Jan. 1994.

[16] D. L. Hill, C. R. J. Maurer, R. J. Maciunas, J. A. Barwise, J. M. Fitzpatrick, and M. Y. Wang, "Measurement of intraoperative brain surface deformation under a craniotomy.," *Neurosurgery*, vol. 43, no. 3, pp. 514–518, Sep. 1998.

[17] N. L. Dorward, O. Alberti, B. Velani, F. A. Gerritsen, W. F. Harkness, N. D. Kitchen, and D. G. Thomas, "Postimaging brain distortion: magnitude, correlates, and impact on neuronavigation.," *J. Neurosurg.*, vol. 88, no. 4, pp. 656–662, Apr. 1998.

[18] X. Fan, S. Ji, A. Hartov, D. W. Roberts, and K. D. Paulsen, "Stereovision to MR image registration for cortical surface displacement mapping to enhance image-guided neurosurgery.," *Med. Phys.*, vol. 41, no. 10, p. 102302, Oct. 2014.

[19] T. Nagaya, Y. A. Nakamura, P. L. Choyke, and H. Kobayashi, "Fluorescence-Guided Surgery," *Front. Oncol.*, vol. 7, p. 314, 2017.

[20] J. T. Alander, I. Kaartinen, A. Laakso, T. Patila, T. Spillmann, V. V Tuchin, M. Venermo, and P. Valisuo, "A review of indocyanine green fluorescent imaging in surgery.," *Int. J. Biomed. Imaging*, vol. 2012, p. 940585, 2012.

[21] L. Xi and H. Jiang, “Image-guided surgery using multimodality strategy and molecular probes.,” *Wiley Interdiscip. Rev. Nanomed. Nanobiotechnol.*, vol. 8, no. 1, pp. 46–60, 2016.

[22] A. Kim, M. Khurana, Y. Moriyama, and B. C. Wilson, “Quantification of in vivo fluorescence decoupled from the effects of tissue optical properties using fiber-optic spectroscopy measurements.,” *J. Biomed. Opt.*, vol. 15, no. December, p. 067006, 2010.

[23] N. Haj-Hosseini, J. Richter, S. Andersson-Engels, and K. Wårdell, “Optical touch pointer for fluorescence guided glioblastoma resection using 5-aminolevulinic acid,” *Lasers Surg. Med.*, vol. 42, no. October 2009, pp. 9–14, 2010.

[24] P. a Valdés, F. Leblond, V. L. Jacobs, B. C. Wilson, K. D. Paulsen, and D. W. Roberts, “Quantitative, spectrally-resolved intraoperative fluorescence imaging.,” *Sci. Rep.*, vol. 2, p. 798, 2012.

[25] Y. Tamura, T. Kuroiwa, Y. Kajimoto, Y. Miki, S.-I. Miyatake, and M. Tsuji, “Endoscopic identification and biopsy sampling of an intraventricular malignant glioma using a 5–aminolevulinic acid–induced protoporphyrin IX fluorescence imaging system,” *J. Neurosurg.*, vol. 106, no. 3, pp. 507–510, Mar. 2007.

[26] S. Utsuki, N. Miyoshi, H. Oka, Y. Miyajima, S. Shimizu, S. Suzuki, and K. Fujii, “Fluorescence-guided resection of metastatic brain tumors using a 5-aminolevulinic acid-induced protoporphyrin IX: Pathological study,” *Brain Tumor Pathol.*, vol. 24, pp. 53–55, 2007.

[27] Y. Kajimoto, T. Kuroiwa, S.-I. Miyatake, T. Ichioka, M. Miyashita, H. Tanaka, and M. Tsuji, “Use of 5-aminolevulinic acid in fluorescence-guided resection of meningioma with high risk of recurrence,” *J. Neurosurg.*, vol. 106, no. 6, pp. 1070–1074, Jun. 2007.

[28] P. Valdes, P. Valdes, B. T. Harris, B. T. Harris, F. Leblond, F. Leblond, K. M. Fontaine, K. M. Fontaine, S. Ji, S. Ji, B. W, and B. W, “Brain tumor resection guided by fluorescence imaging and MRI image guidance,” *Proc. SPIE*, vol. 7261, pp. 726103–726103–8, 2009.

[29] F. Leblond, K. M. Fontaine, P. Valdes, S. Ji, B. W. Pogue, A. Hartov, D. W. Roberts, and K. D. Paulsen, “Brain tumor resection guided by fluorescence imaging,” *Proc. SPIE*, vol. 7164, p. 71640M–71640M–8, 2009.

[30] S. Gioux, A. Mazhar, D. J. Cuccia, A. J. Durkin, B. J. Tromberg, and J. V Frangioni, “Three-dimensional surface profile intensity correction for spatially modulated imaging.,” *J. Biomed. Opt.*, vol. 14, no. June 2009, p. 034045, 2009.

[31] D. J. Mirota, M. Ishii, and G. D. Hager, “Vision-based navigation in image-guided interventions.,” *Annu. Rev. Biomed. Eng.*, vol. 13, pp. 297–319, Aug. 2011.

[32] The Mathworks Inc., “Stereo vision for depth estimation,” 2018. [Online]. Available: https://fr.mathworks.com/discovery/stereo-vision.html. [Accessed: 28-Mar-2018].

[33] M. Qasaimeh and E. N. Salahat, “Real-Time Image and Video Processing Using High-Level Synthesis (HLS),” in *Handbook of Research on Advanced Concepts in Real-Time Image and Video Processing*, Hershey, PA: IGI Global, 2018, pp. 390–408.

[34] S. Cagnoni, M. Mordonini, L. Mussi, and G. Adorni, “Hybrid Dual Camera Vision Systems,” in *Encyclopedia of Artificial Intelligence*, IGI Global., J. R. Rabuñal Dopico, J. Dorado, and A. Pazos, Eds. Hershey, PA: IGI Global, 2009, pp. 848–852.

[35] P. K. Rastogi and H. Erwin, *Optical methods for solid mechanics : a full-field approach*. Weinheim: Wiley-VCH., 2012.

[36] Q. Zhang, *Precision Agriculture Technology for Crop Farming*. Boca Raton, FL, USA: CRC Press, Inc., 2015.

[37] D. Scharstein, *View Synthesis Using Stereo Vision*. Berlin, Heidelberg: Springer-Verlag, 1999.

[38] M. Bennamoun and G. J. Mamic, *Object Recognition: Fundamentals and Case Studies*. New York, NY, USA: Springer-Verlag New York, Inc., 2002.

[39] C. Loop and Z. Zhang, “Computing rectifying homographies for stereo vision,” in *Proceedings. 1999 IEEE Computer Society Conference on Computer Vision and Pattern Recognition (Cat. No PR00149)*, 1999, vol. 1, pp. 1–131 Vol. 1.

[40] J. Geng, “Structured-light 3D surface imaging: a tutorial,” *Adv. Opt. Photon.*, vol. 3, no. 2, pp. 128–160, Jun. 2011.

[41] A. S. Malik, T. S. Choi, and H. Nisar, Eds., *Depth Map and 3D Imaging Applications*. IGI Global, 2012.

[42] D. J. Cuccia, F. Bevilacqua, A. J. Durkin, F. R. Ayers, and B. J. Tromberg, “Quantitation and mapping of tissue optical properties using modulated imaging,” *J. Biomed. Opt.*, vol. 14, no. 2, pp. 24012–24013, 2009.

[43] G. Bhatia, M. W. Vannier, K. E. Smith, P. K. Commean, J. Riolo, and V. L. Young, “Quantification of Facial Surface Change Using a Structured Light Scanner.,” *Plast. Reconstr. Surg.*, vol. 94, no. 6, 1994.

[44] R. P. Mehta, S. Zhang, and T. A. Hadlock, “Novel 3-D video for quantification of facial movement,” *Otolaryngol. Neck Surg.*, vol. 138, no. 4, pp. 468–472, Apr. 2008.

[45] S. Zhang and S.-T. Yau, “High-resolution, real-time 3D absolute coordinate measurement based on a phase-shifting method,” *Opt. Express*, vol. 14, no. 7, pp. 2644–2649, 2006.

[46] I. AKS, H. Sugimoto, D. B. Smith, and M. S. Sacks, “Dynamic in vitro quantification of bioprosthetic heart valve leaflet motion using structured light projection.,” *Ann. Biomed. Eng.*, vol. 29, no. 11, pp. 963–973, Nov. 2001.

[47] C. Schmalz, F. Forster, A. Schick, and E. Angelopoulou, “An endoscopic 3D scanner based on structured light.,” *Med. Image Anal.*, vol. 16, no. 5, pp. 1063–1072, Jul. 2012.

[48] S. Van der Jeught and J. J. J. Dirckx, “Real-time structured light-based otoscopy for quantitative measurement of eardrum deformation,” *J. Biomed. Opt.*, vol. 22, no. 1, p. 16008, 2017.

[49] S. Ji, X. Fan, K. D. Paulsen, D. W. Roberts, S. K. Mirza, and S. S. Lollis, “Patient Registration Using Intraoperative Stereovision in Image-guided Open Spinal Surgery.,” *IEEE Trans. Biomed. Eng.*, vol. 62, no. 9, pp. 2177–2186, Sep. 2015.

[50] S. Ji, X. Fan, D. W. Roberts, A. Hartov, and K. D. Paulsen, “Flow-Based Correspondence Matching in Stereovision BT - Machine Learning in Medical Imaging: 4th International Workshop, MLMI 2013, Held in Conjunction with MICCAI 2013, Nagoya, Japan, September 22, 2013. Proceedings,” G. Wu, D. Zhang, D. Shen, P. Yan, K. Suzuki, and F. Wang, Eds. Cham: Springer International Publishing, 2013, pp. 106–113.

[51] A. Brahme, *Comprehensive biomedical physics*. Oxford, UK: Elsevier, 2014.

[52] M. Schwab, Ed., “Fluorescence,” in *Encyclopedia of Cancer*, Berlin, Heidelberg: Springer Berlin Heidelberg, 2011, pp. 1426–1427.

[53] A. Garman, *Non-Radioactive Labelling*. London, UK: Academic Press, 1997, p. 160.

[54] J. R. Lakowicz, *Principles of fluorescence spectroscopy*. p. 2006.

[55] “Excitation Spectrum,” in *Encyclopedic Reference of Genomics and Proteomics in Molecular Medicine*, Berlin, Heidelberg: Springer Berlin Heidelberg, 2006, p. 536.

[56] “Photobleaching,” in *Encyclopedic Reference of Genomics and Proteomics in Molecular Medicine*, Berlin, Heidelberg: Springer Berlin Heidelberg, 2006, p. 1407.

[57] M. S. Patterson, B. C. Wilson, and D. R. Wyman, “The propagation of optical radiation in tissue I. Models of radiation transport and their application,” *Lasers Med. Sci.*, vol. 6, no. 2, pp. 155–168, Jun. 1991.

[58] M. Joel and V.-D. Tuan, “Biomedical Photonics Handbook,” Boca Raton, Florida: CRC Press, 2003, pp. 1–76.

[59] G. Keiser, “Biophotonics : concepts to applications,” 2016.

[60] A. Roggan, “The optical properties of biological tissue in the near infrared wavelength range: review and measurements,” in *Laser-Induced Interstitial Thermotherapy Workshop*, Bellingham, Washington: SPIE, 1995, pp. 10–44.

[61] G. Lu and B. Fei, “Medical hyperspectral imaging: a review,” *J. Biomed. Opt.*, vol. 19, p. 10901, 2014.

[62] A. J. Welch, M. J. C. van Gemert, and W. M. Star, “Definitions and Overview of Tissue Optics,” in *Optical-Thermal Response of Laser-Irradiated Tissue*, A. J. Welch and M. J. C. van Gemert, Eds. Dordrecht: Springer Netherlands, 2011, pp. 27–64.

[63] “Fundamentals of Laser-Tissue Interactions,” *Veterinary Laser Surgery*. 28-Jan-2008.

[64] F. S. Azar, X. Intes, *Translational multimodality optical imaging*. Boston : Artech House, c2008.

[65] R. Salzer, “Biomedical Imaging: Principles and Applications .” Wiley , Hoboken , 2012.

[66] V. Tuchin, *Tissue Optics: Light Scattering Methods and Instruments for Medical Diagnosis*. SPIE, 2015.

[67] M. Sasha, M. Jelena, and F. Michael, “Reflectance spectroscopy,” in *Handbook of Biomedical Optics*, CRC Press, 2011, pp. 103–130.

[68] N. Nishida, H. Yano, T. Nishida, T. Kamura, and M. Kojiro, “Angiogenesis in Cancer,” *Vasc. Health Risk Manag.*, vol. 2, no. 3, pp. 213–219, Sep. 2006.

[69] J. Samuel and C. Franklin, “Hypoxemia and Hypoxia BT - Common Surgical Diseases: An Algorithmic Approach to Problem Solving,” J. A. Myers, K. W. Millikan, and T. J. Saclarides, Eds. New York, NY: Springer New York, 2008, pp. 391–394.

[70] R. Weissleder and V. Ntziachristos, “Shedding light onto live molecular targets,” *Nat. Med.*, vol. 9, p. 123, Jan. 2003.

[71] D. Roblyer, R. Richards-Kortum, K. Sokolov, A. K. El-Naggar, M. D. Williams, C. Kurachi, and A. M. Gillenwater, “Multispectral optical imaging device for in vivo detection of oral neoplasia,” *J. Biomed. Opt.*, vol. 13, no. 2, p. 24019, 2008.

[72] B. W. Pogue, S. L. Gibbs-Strauss, P. a. Valdés, K. S. Samkoe, D. W. Roberts, and K. D. Paulsen, “Review of neurosurgical fluorescence imaging methodologies,” *IEEE J. Sel. Top. Quantum Electron.*, vol. 16, no. 3, pp. 493–505, 2010.

[73] D. A. Haidar, B. Leh, M. Zanello, and R. Siebert, “Spectral and lifetime domain measurements of rat brain tumors.,” *Biomed. Opt. Express*, vol. 6, no. 4, pp. 1219–1233, Apr. 2015.

[74] M. Zanello, F. Poulon, P. Varlet, F. Chretien, F. Andreiuolo, M. Pages, A. Ibrahim, J. Pallud, E. Dezamis, G. Abi-Lahoud, F. Nataf, B. Turak, B. Devaux, and D. Abi-Haidar, “Multimodal optical analysis of meningioma and comparison with histopathology.,” *J. Biophotonics*, vol. 10, no. 2, pp. 253–263, Feb. 2017.

[75] I. J. Bigio and S. G. Bown, “Spectroscopic sensing of cancer and cancer therapy: current status of translational research.,” *Cancer Biol. Ther.*, vol. 3, no. 3, pp. 259–267, Mar. 2004.

[76] A. C. Croce and G. Bottiroli, “Autofluorescence spectroscopy and imaging: a tool for biomedical research and diagnosis.,” *Eur. J. Histochem.*, vol. 58, no. 4, p. 2461, Dec. 2014.

[77] F. Bevilacqua, D. Piguet, P. Marquet, J. D. Gross, B. J. Tromberg, and C. Depeursinge, “In vivo local determination of tissue optical properties: applications to human brain.,” *Appl. Opt.*, vol. 38, no. 22, pp. 4939–4950, Aug. 1999.

[78] A. N. Yaroslavsky, P. C. Schulze, I. V Yaroslavsky, R. Schober, F. Ulrich, and H. J. Schwarzmaier, “Optical properties of selected native and coagulated human brain tissues in vitro in the visible and near infrared spectral range.,” *Phys. Med. Biol.*, vol. 47, no. 12, pp. 2059–2073, Jun. 2002.

[79] J. Swartling, S. Palsson, P. Platonov, S. B. Olsson, and S. Andersson-Engels, “Changes in tissue optical properties due to radio-frequency ablation of myocardium.,” *Med. Biol. Eng. Comput.*, vol. 41, no. 4, pp. 403–409, Jul. 2003.

[80] M. Solonenko, R. Cheung, T. M. Busch, A. Kachur, G. M. Griffin, T. Vulcan, T. C. Zhu, H.-W. Wang, S. M. Hahn, and A. G. Yodh, “In vivo reflectance measurement of optical properties, blood oxygenation and motexafin lutetium uptake in canine large bowels, kidneys and prostates.,” *Phys. Med. Biol.*, vol. 47, no. 6, pp. 857–873, Mar. 2002.

[81] E. Rosenthal and K. R. Zinn 1959, “Optical imaging of cancer: clinical applications ; Eben Rosenthal, Kurt R. Zinn, editors .” Springer , New York , 2009.

[82] A. Bogaards, A. Varma, S. P. Collens, A. Lin, A. Giles, V. X. D. Yang, J. M. Bilbao, L. D. Lilge, P. J. Muller, and B. C. Wilson, “Increased brain tumor resection using fluorescence image guidance in a preclinical model,” *Lasers Surg. Med.*, vol. 35, no. June, pp. 181–190, 2004.

[83] M. Olivo and B. C. Wilson, “Mapping ALA-induced PPIX fluorescence in normal brain and brain tumour using confocal fluorescence microscopy.,” *Int. J. Oncol.*, vol. 25, no. 8, pp. 37–45, 2004.

[84] W. Stummer, A. Novotny, H. Stepp, C. Goetz, K. Bise, and H. J. Reulen, “Fluorescence-guided resection of glioblastoma multiforme by using 5-aminolevulinic acid-induced porphyrins: a prospective study in 52 consecutive patients.,” *J. Neurosurg.*, vol. 93, no. 6, pp. 1003–1013, Dec. 2000.

[85] W. Stummer and H. Stepp, “Delineating Normal from Diseased Brain by Aminolevulinic Acid-Induced Fluorescence,” in *Bioanalysis Advanced Materials , Methods , and Devices*, S. J. Madsen, Ed. Las Vegas: Springer, 2013, pp. 173–205.

[86] S. Utsuki, H. Oka, S. Sato, S. Shimizu, S. Suzuki, Y. Tanizaki, K. Kondo, Y. Miyajima, and K. Fujii, “Histological examination of false positive tissue resection using 5-aminolevulinic acid-induced fluorescence guidance.,” *Neurol. Med. Chir. (Tokyo).*, vol. 47, no. 5, pp. 210–214, May 2007.

[87] S. Miyatake, T. Kuroiwa, Y. Kajimoto, M. Miyashita, H. Tanaka, and M. Tsuji, “Fluorescence of non-neoplastic, magnetic resonance imaging-enhancing tissue by 5-aminolevulinic acid: case report.,” *Neurosurgery*, vol. 61, no. 5, pp. E1101–3; discussion E1103–4, Nov. 2007.

[88] A. V DSouza, H. Lin, E. R. Henderson, K. S. Samkoe, and B. W. Pogue, “Review of fluorescence guided surgery systems: identification of key performance capabilities beyond indocyanine green imaging.,” *J. Biomed. Opt.*, vol. 21, no. 8, p. 80901, Aug. 2016.

[89] H. Stepp and W. Stummer, “Delineating Normal from Diseased Brain by Aminolevulinic Acid-Induced Fluorescence,” in *Optical Methods and Instrumentation in Brain Imaging and Therapy*, S. J. Madsen, Ed. New York, NY: Springer New York, 2013, pp. 173–205.

[90] G. A. Wagnieres, W. M. Star, and B. C. Wilson, “In vivo fluorescence spectroscopy and imaging for oncological applications,” *Photochem. Photobiol.*, vol. 68, no. 5, pp. 603–632, Nov. 1998.

[91] R. Richards-Kortum and E. Sevick-Muraca, “Quantitative optical spectroscopy for tissue diagnosis.,” *Annu. Rev. Phys. Chem.*, vol. 47, pp. 555–606, 1996.

[92] B. W. Pogue, B. Chen, X. Zhou, and P. J. Hoopes, “Analysis of sampling volume and tissue heterogeneity on the in vivo detection of fluorescence.,” *J. Biomed. Opt.*, vol. 10, no. 4, p. 41206, 2005.

[93] M. Sinaasappel and H. J. Sterenborg, “Quantification of the hematoporphyrin derivative by fluorescence measurementusing dual-wavelength excitation and dual-wavelength detection.,” *Appl. Opt.*, vol. 32, no. 4, pp. 541–548, Feb. 1993.

[94] H. J. C. M. Sterenborg, A. E. Saarnak, R. Frank, and M. Motamedi, “Evaluation of spectral correction techniques for fluorescence measurements on pigmented lesions in vivo,” *J. Photochem. Photobiol. B Biol.*, vol. 35, no. 3, pp. 159–165, 1996.

[95] W. C. Lin, S. A. Toms, M. Johnson, E. D. Jansen, and A. Mahadevan-Jansen, “In vivo brain tumor demarcation using optical spectroscopy.,” *Photochem. Photobiol.*, vol. 73, no. 4, pp. 396–402, Apr. 2001.

[96] S. A. Toms, W.-C. Lin, R. J. Weil, M. D. Johnson, E. D. Jansen, and A. Mahadevan-Jansen, “Intraoperative optical spectroscopy identifies infiltrating glioma margins with high sensitivity.,” *Neurosurgery*, vol. 61, no. 1 Suppl, pp. 326–327, Jul. 2007.

[97] W. C. Lin, S. A. Toms, M. Motamedi, E. D. Jansen, and A. Mahadevan-Jansen, “Brain tumor demarcation using optical spectroscopy; an in vitro study.,” *J. Biomed. Opt.*, vol. 5, no. 2, pp. 214–220, Apr. 2000.

[98] R. Cicchi, A. Crisci, A. Cosci, G. Nesi, D. Kapsokalyvas, S. Giancane, M. Carini, and F. S. Pavone, “Time- and Spectral-resolved two-photon imaging of healthy bladder mucosa and carcinoma in situ.,” *Opt. Express*, vol. 18, no. 4, pp. 3840–3849, Feb. 2010.

[99] M. C. Skala, K. M. Riching, A. Gendron-Fitzpatrick, J. Eickhoff, K. W. Eliceiri, J. G. White, and N. Ramanujam, “In vivo multiphoton microscopy of NADH and FAD redox states, fluorescence lifetimes, and cellular morphology in precancerous epithelia,” *Proc. Natl. Acad. Sci.*, vol. 104, no. 49, p. 19494 LP – 19499, Dec. 2007.

[100] G. Papayan, N. Petrishchev, and M. Galagudza, “Autofluorescence spectroscopy for NADH and flavoproteins redox state monitoring in the isolated rat heart subjected to ischemia-reperfusion.,” *Photodiagnosis Photodyn. Ther.*, vol. 11, no. 3, pp. 400–408, Sep. 2014.

[101] K. Drozdowicz-Tomsia, A. G. Anwer, M. A. Cahill, K. N. Madlum, A. M. Maki, M. S. Baker, and E. M. Goldys, “Multiphoton fluorescence lifetime imaging microscopy reveals free-to-bound NADH ratio changes associated with metabolic inhibition,” vol. 19, pp. 86013–86016, 2014.

[102] J. Horilova, B. Cunderlikova, and A. M. Chorvatova, “Time- and spectrally resolved characteristics of flavin fluorescence in U87MG cancer cells in culture,” vol. 20, pp. 51017–51018, 2014.

[103] L. C. Courrol, F. R. de Oliveira Silva, E. L. Coutinho, M. F. Piccoli, R. D. Mansano, N. D. Vieira Junior, N. Schor, and M. H. Bellini, “Study of blood porphyrin spectral profile for diagnosis of tumor progression.,” *J. Fluoresc.*, vol. 17, no. 3, pp. 289–292, May 2007.

[104] S. Palmer, K. Litvinova, A. Dunaev, J. Yubo, D. McGloin, and G. Nabi, "Optical redox ratio and endogenous porphyrins in the detection of urinary bladder cancer: A patient biopsy analysis.," *J. Biophotonics*, vol. 10, no. 8, pp. 1062–1073, Aug. 2017.

[105] B. Chance, B. Schoener, R. Oshino, F. Itshak, and Y. Nakase, "Oxidation-reduction ratio studies of mitochondria in freeze-trapped samples. NADH and flavoprotein fluorescence signals.," *J. Biol. Chem.*, vol. 254, no. 11, pp. 4764–4771, Jun. 1979.

[106] M. G. Muller, I. Georgakoudi, Q. Zhang, J. Wu, and M. S. Feld, "Intrinsic fluorescence spectroscopy in turbid media: disentangling effects of scattering and absorption.," *Appl. Opt.*, vol. 40, no. 25, pp. 4633–4646, Sep. 2001.

[107] C. J. Gulledge and M. W. Dewhirst, "Tumor oxygenation: a matter of supply and demand.," *Anticancer Res.*, vol. 16, no. 2, pp. 741–749, 1996.

[108] R. Drezek, C. Brookner, I. Pavlova, I. Boiko, A. Malpica, R. Lotan, M. Follen, and R. Richards-Kortum, "Autofluorescence microscopy of fresh cervical-tissue sections reveals alterations in tissue biochemistry with dysplasia.," *Photochem. Photobiol.*, vol. 73, no. 6, pp. 636–641, Jun. 2001.

[109] N. Ramanujam, R. Richards-Kortum, S. Thomsen, A. Mahadevan-Jansen, M. Follen, and B. Chance, "Low Temperature Fluorescence Imaging of Freeze-trapped Human Cervical Tissues.," *Opt. Express*, vol. 8, no. 6, pp. 335–343, Mar. 2001.

[110] M. C. Skala, A. Fontanella, L. Lan, J. A. Izatt, and M. W. Dewhirst, "Longitudinal optical imaging of tumor metabolism and hemodynamics.," *J. Biomed. Opt.*, vol. 15, no. 1, p. 11112, 2010.

[111] Q. Liu, G. Grant, J. Li, Y. Zhang, F. Hu, S. Li, C. Wilson, K. Chen, D. Bigner, and T. Vo-Dinh, "Compact point-detection fluorescence spectroscopy system for quantifying intrinsic fluorescence redox ratio in brain cancer diagnostics.," *J. Biomed. Opt.*, vol. 16, no. 3, p. 37004, Mar. 2011.

[112] H. Sato and T. Takino, "Coordinate action of membrane-type matrix metalloproteinase-1 (MT1-MMP) and MMP-2 enhances pericellular proteolysis and invasion," *Cancer Sci.*, vol. 101, no. 4, pp. 843–847, 2010.

[113] A. Varone, J. Xylas, K. P. Quinn, D. Pouli, G. Sridharan, M. E. McLaughlin-Drubin, C. Alonzo, K. Lee, K. Münger, and I. Georgakoudi, "Endogenous Two-Photon Fluorescence Imaging Elucidates Metabolic Changes Related to Enhanced Glycolysis and Glutamine Consumption in Precancerous Epithelial Tissues," *Cancer Res.*, vol. 74, no. 11, pp. 3067–3075, Jun. 2014.

[114] J. H. Ostrander, C. M. McMahon, S. Lem, S. R. Millon, J. Q. Brown, V. L. Seewaldt, and N. Ramanujam, "Optical redox ratio differentiates breast cancer cell lines based on estrogen receptor status.," *Cancer Res.*, vol. 70, no. 11, pp. 4759–4766, Jun. 2010.

[115] S. Palmer, K. Litvinova, E. U. Rafailov, and G. Nabi, "Detection of urinary bladder cancer cells using redox ratio and double excitation wavelengths autofluorescence," *Biomed. Opt. Express*, vol. 6, no. 3, pp. 977–986, Mar. 2015.

[116] M. H. Bellini, E. L. Coutinho, L. C. Courrol, F. de Oliveira Silva, N. D. Vieira Júnior, and N. Schor, "Correlation between autofluorescence intensity and tumor area in mice bearing renal cell carcinoma," *J. Fluoresc.*, vol. 18, no. 6, p. 1163—1168, Nov. 2008.

[117] M. Inaguma and K. Hashimoto, "Porphyrin-like fluorescence in oral cancer," *Cancer*, vol. 86, no. 11, pp. 2201–2211, 1999.

[118] O. Aboumarzouk, R. Valentine, R. Buist, S. Ahmad, G. Nabi, S. Eljamel, H. Moseley, and S. G. Kata, "Laser-induced autofluorescence spectroscopy: can it be of importance in detection of bladder lesions?," *Photodiagnosis Photodyn. Ther.*, vol. 12, no. 1, pp. 76–83, Mar. 2015.

[119] S. C. Gebhart, R. C. Thompson, and A. Mahadevan-Jansen, "Liquid-crystal tunable filter spectral imaging for brain tumor demarcation.," *Appl. Opt.*, vol. 46, no. 10, pp. 1896–1910, Apr. 2007.

[120] W. Stummer, H. Stepp, G. Möller, a. Ehrhardt, M. Leonhard, and H. J. Reulen, "Technical principles for protoporphyrin-IX-fluorescence guided microsurgical resection of malignant glioma tissue," *Acta Neurochir. (Wien).*, vol. 140, pp. 995–1000, 1998.

[121] P. A. Valdes, V. L. Jacobs, B. C. Wilson, F. Leblond, D. W. Roberts, and K. D. Paulsen, "System and methods for wide-field quantitative fluorescence imaging during neurosurgery," *Opt. Lett.*, vol. 38, no. 15, pp. 2786–2788, Aug. 2013.

[122] J. J. Bravo, J. D. Olson, S. C. Davis, D. W. Roberts, K. D. Paulsen, and S. C. Kanick, "Hyperspectral data processing improves PpIX contrast during fluorescence guided surgery of human brain tumors," *Sci. Rep.*, vol. 7, no. 1, p. 9455, 2017.

[123] S. Van der Jeught, J. A. M. Soons, and J. J. J. Dirckx, "Real-time microscopic phase-shifting profilometry," *Appl. Opt.*, vol. 54, no. 15, pp. 4953–4959, May 2015.

[124] VariSpec Liquid Crystal Tunable Filters, "How do they work? Tunable filters for VIS or NIR imaging with no moving parts.," 2013. [Online]. Available: https://www.perkinelmer.com.cn/CMSResources/Images/46-151237TCH_010933_01_VariSpec_FAQ.pdf. [Accessed: 22-Mar-2018].

[125] Edmund Optics, “Understanding Microscopes and Objectives,” 2018. [Online]. Available: https://www.edmundoptics.eu/resources/application-notes/microscopy/understanding-microscopes-and-objectives/. [Accessed: 21-Mar-2018].

[126] SCHOTT AG, “SCHOTT® Wound Fiber Bundles.” [Online]. Available: http://www.schott.com/d/lightingimaging/de2564e1-ab91-46bf-8f85-bb7cff7e9c45/1.0/wound_fiber_bundles_general_int_october_2013_final_.pdf. [Accessed: 22-Mar-2018].

[127] Texas Instruments, “DLP System Optics,” *Application Report*, 2010. [Online]. Available: http://www.ti.com/lit/an/dlpa022/dlpa022.pdf. [Accessed: 25-Mar-2018].

[128] J. Allen, “Application of patterned illumination using a DMD for optogenetic control of signaling,” *Nat. Methods*, vol. 14, Oct. 2017.

[129] Texas Instruments, “DLP Products - Getting started,” 2017. [Online]. Available: http://www.ti.com/dlp-chip/getting-started.html. [Accessed: 25-Mar-2018].

[130] S. Dewald, “Introduction to DLP Optics.” [Online]. Available: http://www.dlinnovations.com/dli/wp-content/uploads/presentation-introduction-to-dlp-optics.pdf. [Accessed: 23-May-2017].

[131] Y. Lu, R. Zhang, and H. Guo, “Correction of illumination fluctuations in phase-shifting technique by use of fringe histograms,” *Appl. Opt.*, vol. 55, no. 1, pp. 184–197, Jan. 2016.

[132] C. B. Jaffe and S. M. Jaffe, “Lumencor White Paper: Solid state light engines for bioanalytical instruments and biomedical devices,” 2010. [Online]. Available: http://lumencor.com/wp-content/uploads/sites/3/2014/09/Lumencor-White-Paper-II.pdf. [Accessed: 23-May-2017].

[133] U.-H. Lee and Y.-G. Ju, “Effects of a Cylindrical Cavity on the Etendue of a Light Source,” *Jpn. J. Appl. Phys.*, vol. 50, no. 12R, p. 122501, 2011.

[134] J. T. Elliott, A. V Dsouza, K. Marra, B. W. Pogue, D. W. Roberts, and K. D. Paulsen, “Microdose fluorescence imaging of ABY-029 on an operating microscope adapted by custom illumination and imaging modules.,” *Biomed. Opt. Express*, vol. 7, no. 9, pp. 3280–3288, Sep. 2016.

[135] S. Ji, X. Fan, D. W. Roberts, and K. D. Paulsen, “Efficient stereo image geometrical reconstruction at arbitrary camera settings from a single calibration.,” *Med. Image Comput. Comput. Assist. Interv.*, vol. 17, no. Pt 1, pp. 440–447, 2014.

[136] Y. Gosselin, “Caméra hyperspectrale d’imagerie en fluorescence pour guider l’exérèse de tumeurs du cerveau,” École Polytechnique de Montréal, 2014.

[137] M. Jermyn, Y. Gosselin, P. A. Valdes, M. Sibai, K. Kolste, J. Mercier, L. Angulo, D. W. Roberts, K. D. Paulsen, K. Petrecca, O. Daigle, B. C. Wilson, and F. Leblond, "Improved sensitivity to fluorescence for cancer detection in wide-field image-guided neurosurgery," *Biomed. Opt. Express*, vol. 6, no. 12, pp. 5063–5074, Dec. 2015.

[138] D. Malacara, *Optical Shop Testing*. Hoboken, USA: John Wiley & Sons, Incorporated, 2007.

[139] A. J. Lewis, "Absolute length measurement using multiple-wavelength phase-stepping interferometry," University of London, 1993.

[140] M. Gdeisat and F. Lilley, "Two-Dimensional Phase Unwrapping Problem." .

[141] S. J. Madsen and B. C. Wilson, "Optical Properties of Brain Tissue," in *Optical Methods and Instrumentation in Brain Imaging and Therapy*, S. J. Madsen, Ed. New York, NY: Springer New York, 2013, pp. 1–22.

[142] N. Haj-Hosseini, B. Kistler, and K. Wårdell, "Development and characterization of a brain tumor mimicking fluorescence phantom," *Proc. SPIE*, vol. 8945. pp. 894505–894507, 2014.

[143] Semrock, "442 nm EdgeBasic™ best-value long-pass edge filter," 2018. [Online]. Available: https://www.semrock.com/filterdetails.aspx?id=blp01-442r-25.

[144] D. H. Foster, "Tutorial on Transforming Hyperspectral Images," *(University of Manchester)*, 2015. [Online]. Available: http://personalpages.manchester.ac.uk/staff/d.h.foster/Tutorial_HSI2RGB/Tutorial_HSI2RGB.html. [Accessed: 20-Jul-2008].

[145] W. R. Hendee, "Breast MRI: Fundamentals and Technical Aspects," *Med. Phys.*, vol. 35, no. 3, pp. 1163–1164, 2008.

[146] S. W. Smith, "CHAPTER 25 - Special Imaging Techniques," in *Digital Signal Processing*, S. W. Smith, Ed. Boston: Newnes, 2003, pp. 423–450.

[147] "Techniques for fluorescence detection of protoporphyrin IX in skin cancers associated with photodynamic therapy ," *Photonics & Lasers in Medicine* , vol. 2 . p. 287, 2013.

[148] Thorlabs, "Articulating platforms," 2018. [Online]. Available: https://www.thorlabs.com/newgrouppage9.cfm?objectgroup_id=209&pn=AP180/M#6150. [Accessed: 23-Apr-2018].

[149] L.-C. Chen and L.-H. Tsai, "Dual Phase-shifting Moiré Projection with Tunable High Contrast Fringes for Three-Dimensional Microscopic Surface Profilometry," *Phys. Procedia*, vol. 19, pp. 67–75, 2011.

[150] L.-C. Chen, D.-H. Duong, and C.-S. Chen, "3-D Surface Profilometry for Objects Having Extremely Different Reflectivity Regions," in *The 14th IFToMM World Congress*, 2015.

[151] G. Themelis, J. S. Yoo, K.-S. Soh, R. Schulz, and V. Ntziachristos, "Real-time intraoperative fluorescence imaging system using light-absorption correction.," *J. Biomed. Opt.*, vol. 14, no. 6, p. 64012, 2009.

[152] S. C. G. and W. C. L. and A. Mahadevan-Jansen, "In vitro determination of normal and neoplastic human brain tissue optical properties using inverse adding-doubling," *Phys. Med. Biol.*, vol. 51, no. 8, p. 2011, 2006.

[153] M. Marois, J. J. Bravo, S. C. Davis, and S. C. Kanick, "Characterization and standardization of tissue-simulating protoporphyrin IX optical phantoms," vol. 21, pp. 35003–35009, 2016.

[154] M. Zanello, F. Poulon, J. Pallud, P. Varlet, H. Hamzeh, G. Abi Lahoud, F. Andreiuolo, A. Ibrahim, M. Pages, F. Chretien, F. Di Rocco, E. Dezamis, F. Nataf, B. Turak, B. Devaux, and D. Abi Haidar, "Multimodal optical analysis discriminates freshly extracted human sample of gliomas, metastases and meningiomas from their appropriate controls," *Sci. Rep.*, vol. 7, p. 41724, Feb. 2017.

[155] D. Basaran, M. C. Salman, G. Boyraz, I. Selcuk, A. Usubutun, N. Ozgul, and K. Yuce, "Accuracy of intraoperative frozen section in the evaluation of patients with adnexal mass: retrospective analysis of 748 cases with multivariate regression analysis.," *Pathol. Oncol. Res.*, vol. 21, no. 1, pp. 113–118, Jan. 2015.

[156] K. J. Chambers, S. Kraft, and K. Emerick, "Evaluation of frozen section margins in high-risk cutaneous squamous cell carcinomas of the head and neck," *Laryngoscope*, vol. 125, no. 3, pp. 636–639, 2015.

[157] G. Novita, J. R. Filassi, C. A. Ruiz, M. D. Ricci, K. M. Pincerato, H. R. de Oliveira Filho, J. M. J. Soares, and E. C. Baracat, "Evaluation of frozen-section analysis of surgical margins in the treatment of breast cancer.," *Eur. J. Gynaecol. Oncol.*, vol. 33, no. 5, pp. 498–501, 2012.

[158] E. L. Rosenthal, J. M. Warram, E. de Boer, J. P. Basilion, M. A. Biel, M. Bogyo, M. Bouvet, B. E. Brigman, Y. L. Colson, S. R. DeMeester, G. C. Gurtner, T. Ishizawa, P. M. Jacobs, S. Keereweer, J. C. Liao, Q. T. Nguyen, J. M. Olson, K. D. Paulsen, D. Rieves, B. D. Sumer, M. F. Tweedle, A. L. Vahrmeijer, J. P. Weichert, B. C. Wilson, M. R. Zenn, K. R. Zinn, and G. M. van Dam, "Successful Translation of Fluorescence Navigation During Oncologic Surgery: A Consensus Report.," *J. Nucl. Med.*, vol. 57, no. 1, pp. 144–150, Jan. 2016.

[159] M. Jermyn, K. Mok, J. Mercier, J. Desroches, J. Pichette, K. Saint-Arnaud, L. Bernstein, M.-C. Guiot, K. Petrecca, and F. Leblond, "Intraoperative brain cancer detection with

Raman spectroscopy in humans.," *Sci. Transl. Med.*, vol. 7, no. 274, p. 274ra19, Feb. 2015.

[160] M. M. Haglund, M. S. Berger, and D. W. Hochman, "Enhanced Optical Imaging of Human Gliomas and Tumor Margins," *Neurosurgery*, vol. 38, no. 2, 1996.

[161] M. Sibai, I. Veilleux, J. T. Elliott, F. Leblond, and B. C. Wilson, "Quantitative spatial frequency fluorescence imaging in the sub-diffusive domain for image-guided glioma resection," *Biomed. Opt. Express*, vol. 6, no. 12, p. 4923, 2015.

[162] D. J. Cuccia, F. Bevilacqua, A. J. Durkin, and B. J. Tromberg, "Modulated imaging: quantitative analysis and tomography of turbid media in the spatial-frequency domain.," *Opt. Lett.*, vol. 30, no. 11, pp. 1354–1356, Jun. 2005.

[163] S. C. Kanick, D. M. 3rd McClatchy, V. Krishnaswamy, J. T. Elliott, K. D. Paulsen, and B. W. Pogue, "Sub-diffusive scattering parameter maps recovered using wide-field high-frequency structured light imaging.," *Biomed. Opt. Express*, vol. 5, no. 10, pp. 3376–3390, Oct. 2014.

[164] N. N. Boustany, S. C. Kuo, and N. V Thakor, "Optical scatter imaging: subcellular morphometry in situ with Fourier filtering," *Opt. Lett.*, vol. 26, no. 14, pp. 1063–1065, Jul. 2001.

[165] A. Wax, C. Yang, V. Backman, K. Badizadegan, C. W. Boone, R. R. Dasari, and M. S. Feld, "Cellular organization and substructure measured using angle-resolved low-coherence interferometry.," *Biophys. J.*, vol. 82, no. 4, pp. 2256–2264, Apr. 2002.

[166] G. Schuele, E. Vitkin, P. Huie, C. O'Connell-Rodwell, D. Palanker, and L. T. Perelman, "Optical spectroscopy noninvasively monitors response of organelles to cellular stress.," *J. Biomed. Opt.*, vol. 10, no. 5, p. 51404, 2005.

[167] Y. Liu, X. Li, Y. L. Kim, and V. Backman, "Elastic backscattering spectroscopic microscopy.," *Opt. Lett.*, vol. 30, no. 18, pp. 2445–2447, Sep. 2005.

[168] Y. L. Kim, Y. Liu, R. K. Wali, H. K. Roy, and V. Backman, "Low-coherent backscattering spectroscopy for tissue characterization," *Appl. Opt.*, vol. 44, no. 3, pp. 366–377, Jan. 2005.

[169] V. Krishnaswamy, P. J. Hoopes, K. S. Samkoe, J. A. O'Hara, T. Hasan, and B. W. Pogue, "Quantitative imaging of scattering changes associated with epithelial proliferation, necrosis, and fibrosis in tumors using microsampling reflectance spectroscopy.," *J. Biomed. Opt.*, vol. 14, no. 1, p. 14004, 2009.

[170] H. Subramanian, P. Pradhan, Y. Liu, I. R. Capoglu, J. D. Rogers, H. K. Roy, R. E. Brand, and V. Backman, "Partial-wave microscopic spectroscopy detects subwavelength

refractive index fluctuations: an application to cancer diagnosis.," *Opt. Lett.*, vol. 34, no. 4, pp. 518–520, Feb. 2009.

[171] F. van Leeuwen–van Zaane, U. A. Gamm, P. B. A. A. van Driel, T. J. A. Snoeks, H. S. de Bruijn, A. van der Ploeg–van den Heuvel, I. M. Mol, C. W. G. M. Löwik, H. J. C. M. Sterenborg, A. Amelink, and D. J. Robinson, "In vivo quantification of the scattering properties of tissue using multi-diameter single fiber reflectance spectroscopy," *Biomed. Opt. Express*, vol. 4, no. 5, pp. 696–708, May 2013.

[172] V. Backman and H. K. Roy, "Optical spectroscopic markers of cancer.," *Disease markers*, vol. 25, no. 6. United States, p. 279, 2008.

[173] A. Wax, Y. Zhu, N. G. Terry, X. L. Chen, S. C. Gebhart, and W. J. Brown, "Label-Free Nuclear Morphology Measurements of Dysplasia in the Egda Rat Model Using Angle-Resolved Low Coherence Interferometry," *Gastroenterology*, vol. 136, no. 5, p. A–122, Apr. 2018.

[174] J. Yi, A. J. Radosevich, Y. Stypula-Cyrus, N. N. Mutyal, S. M. Azarin, E. Horcher, M. J. Goldberg, L. K. Bianchi, S. Bajaj, H. K. Roy, and V. Backman, "Spatially resolved optical and ultrastructural properties of colorectal and pancreatic field carcinogenesis observed by inverse spectroscopic optical coherence tomography.," *J. Biomed. Opt.*, vol. 19, no. 3, p. 36013, Mar. 2014.

[175] Y. Liu, S. Uttam, S. Alexandrov, and R. K. Bista, "Investigation of nanoscale structural alterations of cell nucleus as an early sign of cancer," *BMC Biophys.*, vol. 7, no. 1, p. 1, 2014.

[176] M. Patel, A. Gomes, S. Ruderman, D. Hardee, S. Crespo, M. Raimondo, T. Woodward, V. Backman, H. Roy, and M. Wallace, "Polarization gating spectroscopy of normal-appearing duodenal mucosa to detect pancreatic cancer.," *Gastrointest. Endosc.*, vol. 80, no. 5, pp. 782–786, Nov. 2014.

[177] A. M. Laughney, V. Krishnaswamy, E. J. Rizzo, M. C. Schwab, R. J. Barth, B. W. Pogue, K. D. Paulsen, and W. A. Wells, "Scatter spectroscopic imaging distinguishes between breast pathologies in tissues relevant to surgical margin assessment," *Clin. Cancer Res.*, vol. 18, no. 22, pp. 6315–6325, Nov. 2012.

[178] A. M. Laughney, V. Krishnaswamy, E. J. Rizzo, M. C. Schwab, R. J. J. Barth, D. J. Cuccia, B. J. Tromberg, K. D. Paulsen, B. W. Pogue, and W. A. Wells, "Spectral discrimination of breast pathologies in situ using spatial frequency domain imaging.," *Breast Cancer Res.*, vol. 15, no. 4, p. R61, 2013.

[179] A. M. Laughney, V. Krishnaswamy, T. B. Rice, D. J. Cuccia, R. J. Barth, B. J. Tromberg, K. D. Paulsen, B. W. Pogue, and W. A. Wells, "System analysis of spatial frequency

domain imaging for quantitative mapping of surgically resected breast tissues.," *J. Biomed. Opt.*, vol. 18, no. 3, p. 36012, Mar. 2013.

[180] Nuvu cameras, "HNü 512 Spectsheet," 2017. [Online]. Available: http://www.nuvucameras.com/wp-content/uploads/2017/11/NUVUCAMERAS_HNu512.pdf.

[181] S. L. Jacques, "Optical properties of biological tissues: a review," *Phys. Med. Biol.*, vol. 58, no. 11, p. R37, 2013.

[182] R. K. Hobbie and B. J. Roth, "Intermediate physics for medicine and biology." Springer, New York, NY, 2007.

[183] M. Kohl, U. Lindauer, G. Royl, M. Kühl, L. Gold, A. Villringer, and U. Dirnagl, "Physical model for the spectroscopic analysis of cortical intrinsic optical signals," *Phys. Med. Biol.*, vol. 45, no. 12, p. 3749, 2000.

APPENDIX A – TECHNICAL SPECIFICATIONS OF SYSTEM COMPONENTS

Table A-1: Technical specifications of the NUVU camera [180].

Maximum available EM (electron multiplication) gain	5000
Readout noise through: EM channel with electron multiplication Conventional channel	 < 0.1ē @ 20 MHz 3ē @ 100 kHz
Vertical clock speed	EM 0.3 − 5 μs Conv 0.3 − 5 μs
Dark current (All operating modes)	0.0002 ē/pixel/s
Clock-induced charges	0.001 ē/pixel/frame
Charge transfer efficiency	> 0.999993
Single photon detection probability (EM gain = 5000)	> 91%
Imaging area	512 × 512 pixels 16 μm × 16 μm pixel area 8.19 mm × 8.19 mm effective area

Table A-2: Technical information of the single mode laser source coupled to the projector.

Type of laser	Single mode
Fiber optic output	Single mode Core diameter ~3 µm and NA 0.12
Beam diameter	2 mm using Thorlabs collimator (FC220APC-633)
Beam angle (collimated)	~0.45 mrad
Output power (out of single mode fiber)	>= 100 mW
Wavelength	Red (638 nm)
Fiber connector	FC/APC

APPENDIX B – HEIGHT MEASUREMENTS WITH A SINGLE MODE *VS.* A MULTIMODE LASER

Table B-1: Depth measurements obtained from patterns projected by a single mode laser.

Real height (cm)	Computed height (cm)	Standard deviation (cm)	Relative error
0.150	0.159	0.056	0.060
0.300	0.314	0.057	0.046
0.400	0.410	0.058	0.026
0.500	0.508	0.059	0.016
0.600	0.613	0.048	0.022
0.750	0.805	0.045	0.073
0.800	0.822	0.069	0.027
0.900	0.925	0.071	0.028
1.000	1.019	0.053	0.019
1.200	1.233	0.067	0.028
1.400	1.414	0.047	0.010
1.500	1.504	0.079	0.003
1.600	1.650	0.063	0.031
1.800	1.866	0.046	0.037
2.000	2.079	0.053	0.039
2.100	2.149	0.083	0.023
2.200	2.274	0.045	0.034
2.400	2.435	0.040	0.015
2.500	2.478	0.069	0.009
2.600	2.600	0.041	0.000
2.700	2.674	0.076	0.010
2.800	2.837	0.028	0.013
3.000	2.903	0.043	0.032

Table B-2: Reconstruction of steps with different heights using a multimode source for the projection.

Real height (cm)	Computed height (cm)	Standard deviation (cm)	Relative error
0.200	0.217	0.067	0.084
0.300	0.352	0.084	0.174
0.400	0.431	0.057	0.077
0.500	0.557	0.079	0.114
0.600	0.644	0.038	0.073
0.800	0.852	0.037	0.065
0.900	1.006	0.051	0.118
1.000	1.079	0.032	0.079
1.200	1.308	0.037	0.090
1.400	1.531	0.036	0.094
1.500	1.659	0.057	0.106
1.600	1.745	0.041	0.091
1.800	1.969	0.044	0.094
2.000	2.220	0.057	0.110

APPENDIX C – *IN VIVO* TISSUE AUTOFLUORESCENCE

C.1 Fluorescence normalization algorithm

The first spectrometers measured the transmitted light from the sample *T* through a medium containing a chromophore (this medium was non-scattering) by applying the Beer-Lambert law [181] as:

$$T = 10^{-\varepsilon C l} = 10^{-\mu_a l} \quad \text{(C-1)}$$

where:

ε: extinction coefficient of the chromophore

C: chromophore concentration

l: path length factor

μ_a: absorption coefficient

For a scattering medium, such as biological tissue and following the Beer-Lambert law, a scattering factor can be added to the variable *T*, such that ($\mu_a + \mu'_s$) is the *total linear attenuation coefficient* [182]:

$$T = 10^{-(\mu_a + \mu'_s) l} = 10^{-(\varepsilon C + \mu'_s) l} \quad \text{(C-2)}$$

where:

ε: extinction coefficient of the chromophore

C: chromophore concentration

μ'_s: tissue scattering coefficient

l: path length factor

In the literature μ'_s is defined as $\mu'_s = \frac{a(\lambda)^{-b}}{500\ \text{nm}}$; with specific values of *a* (cm^{-1}) = 24.2 and *b* = 1.611 for brain tissue [181].

If we consider that the main chromophores that absorb light strongly in the brain and that significantly affect the intensity of the transmitted light through the sample (*T*) are oxy- and deoxyhemoglobin at different concentrations, together with the level of scattering in the tissue, then:

$$T(\lambda) = 10^{-l(C_{HbO}\varepsilon_{HbO}(\lambda) + C_{HbR}\varepsilon_{HbR}(\lambda) + \mu'_s)} \quad \text{(C-3)}$$

where:

l = 1 (it is constant pixel-by-pixel along the image [183])

C = concentration

HbO = oxyhemoglobin

HbR = deoxyhemoglobin

ε = extinction coefficients for the emission wavelengths

λ = emission wavelengths = 550:720 nm with 4 nm steps.

The -$\log_{10}$ of the white light reflectance intensities ($R_d^{corrected}$) – already spatially and spectrally calibrated – at the different emission wavelengths provides an estimate of the tissue absorbance, this is:

$$A(\lambda) = -\log_{10}\left(R_d^{corrected}(\lambda)\right) \tag{C-4}$$

$$\approx (C_{HbO}\varepsilon_{HbO}(\lambda) + C_{HbR}\varepsilon_{HbR}(\lambda) + \mu'_s) \tag{C-5}$$

Then from Eq. C-3:

$$T(\lambda) \approx 10^{(-A(\lambda))} \tag{C-6}$$

It can be suggested that the fluorescence signal (raw fluorescence data that have undergone all the stages of spatial and spectral calibration, F_R) captured by the imaging system contains the real intensity of the fluorophore of interest at a specific concentration (F_c) and also information of the transmittance factor (T) through the tissue.

$$F_R(\lambda) = F_c(\lambda) \times T(\lambda) \tag{C-7}$$

The excitation source at 405 nm (I_{ex}) could also be included in Eq. C-7. However, to simplify the analysis, the term I_{ex} was not taken into account after having done a spatial calibration on the images; since it is considered that I_{ex} illuminates homogenously the tissue, therefore, the contribution of I_{ex} to the overall emission signal at each pixel may perhaps not make a big difference among pixels.

From Eq. C-7, the corrected fluorescence F_C is:

$$F_C(\lambda) = \frac{F_R(\lambda)}{T(\lambda)} \tag{C-8}$$

And, since $T(\lambda) \approx 10^{(-A(\lambda))}$

$$F_C(\lambda) = \frac{10^{\left(\log_{10}\left(F_R(\lambda)\right)\right)}}{10^{(-A(\lambda))}} \tag{C-9}$$

$$F_C(\lambda) = 10^{\left(\log_{10}\left(F_R(\lambda)\right) - (-A(\lambda))\right)} \tag{C-10}$$

and since $A(\lambda) = -\log_{10}\left(R_d^{corrected}(\lambda)\right)$, the equation applied in this thesis to correct fluorescence emission spectra directly with white light reflectance images is:

$$F_C(\lambda) = 10^{\left(\log_{10}\left(F_R(\lambda)\right) - \log_{10}\left(R_d^{corrected}(\lambda)\right)\right)} \tag{C-11}$$

To confirm that the information in each pixel is due to the tissue response and not to specular reflections, it is checked whether the spectrum in each pixel follows the shape of the absorption spectrum of blood. As explained above, the absorption spectrum for each pixel can be retrieved as $A(\lambda) = -\log_{10}\left(R_d^{corrected}(\lambda)\right)$.

C-2 *In vivo* clinical data

In the following images, it is displayed individually the spectra recorded at nine different interrogation points in brain tissue at the beginning of a surgery, and another group of nine spectra from the end of the same surgery. The point where each spectral signature is taken from is indicated as a datatip on an image next to each spectrum plot. Each plot includes normalized signals (intensities between 0 and 1) of: (a) white light reflectance; (b) raw fluorescence; and, (c) corrected fluorescence. Signals (a) and (b) have already undergone a spectral and spatial calibration and signal (c) is the fluorescence signal retrieved by combining (a) and (b) after applying the fluorescence normalization algorithm explained in section 5.1.1.2.

At the end, Figure C-1 shows a measurement of the possible extent of bleed-through leaking into the emission wavelengths of brain tissue autofluorescence. The same image analysis that was carried out on brain tissue was also done for a Spectralon diffuse reflectance standard to obtain the spectrum in Figure C-1.

i. Fluorescence images from the beginning of the surgery

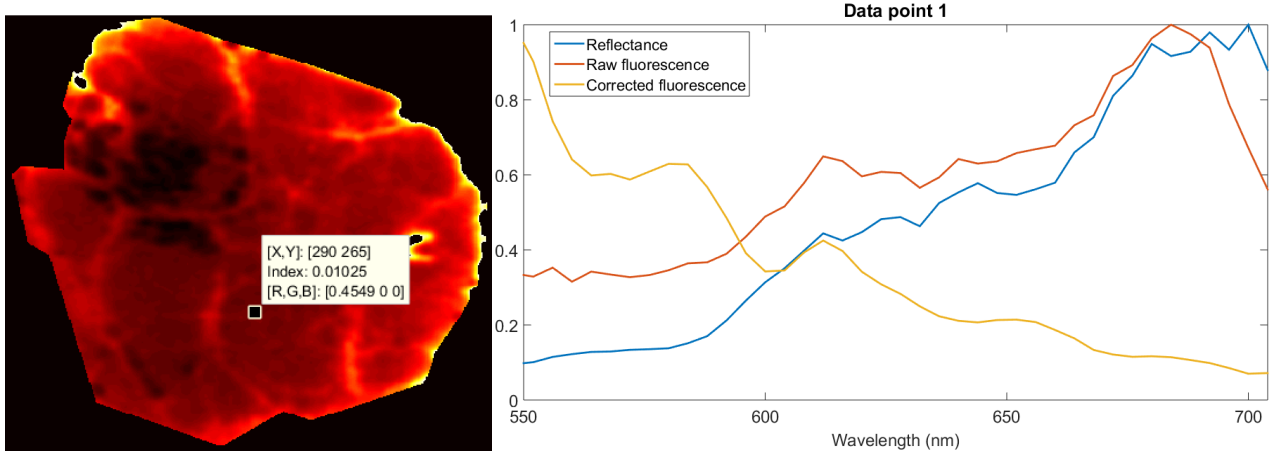

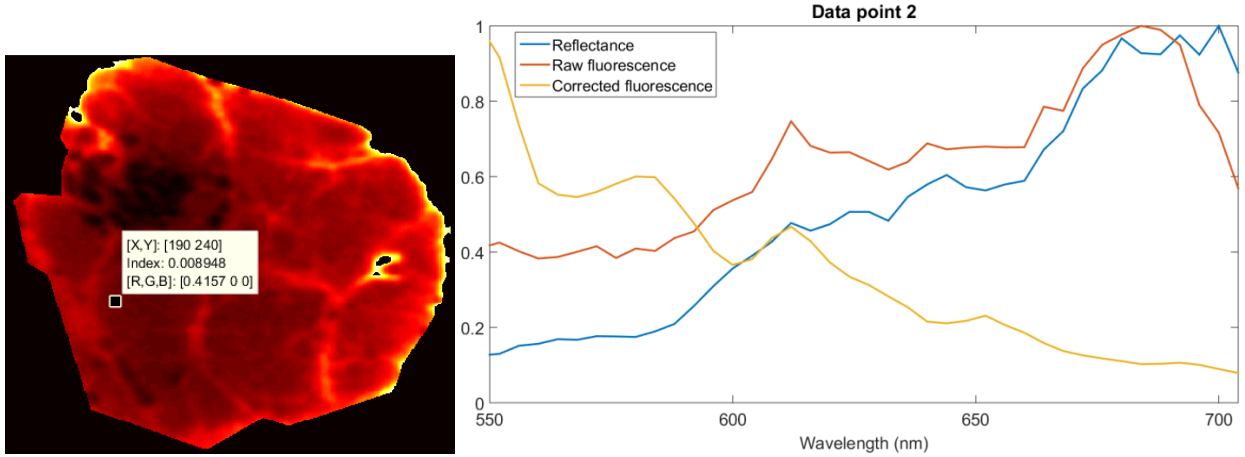

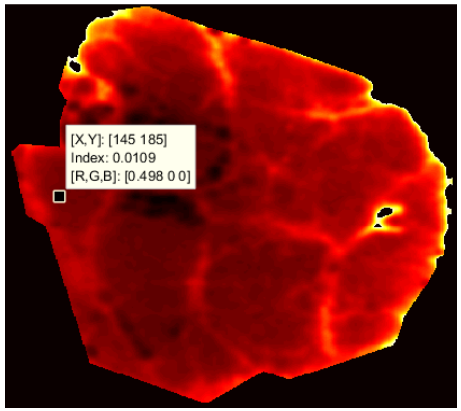
[X,Y]: [145 185]
Index: 0.0109
[R,G,B]: [0.498 0 0]

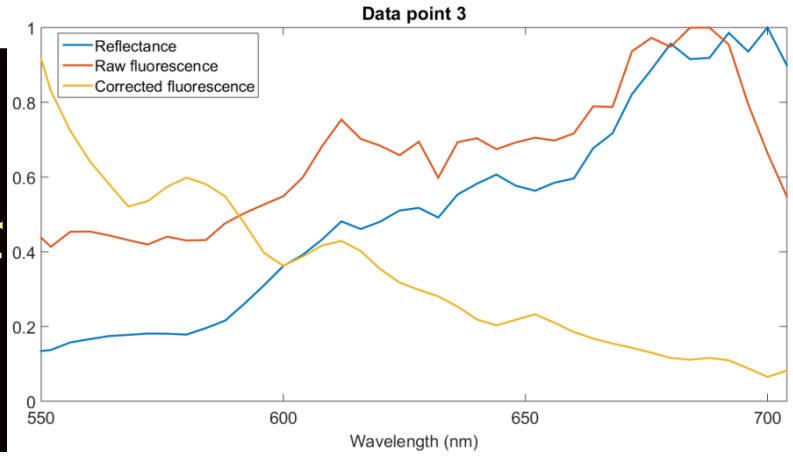
Data point 3
Reflectance
Raw fluorescence
Corrected fluorescence
1
0.8
0.6
0.4
0.2
0
550
600
650
700
Wavelength (nm)

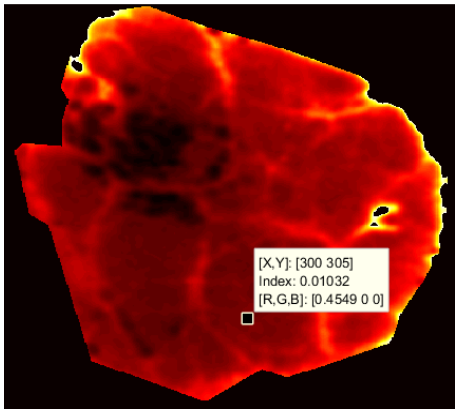
[X,Y]: [300 305]
Index: 0.01032
[R,G,B]: [0.4549 0 0]

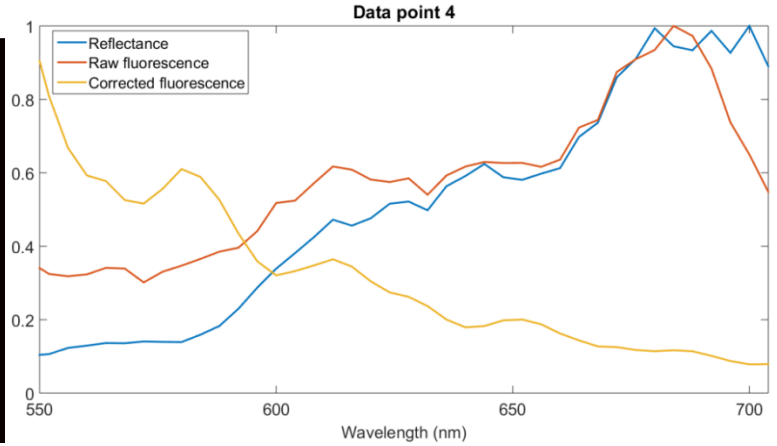
Data point 4
Reflectance
Raw fluorescence
Corrected fluorescence
1
0.8
0.6
0.4
0.2
0
550
600
650
700
Wavelength (nm)

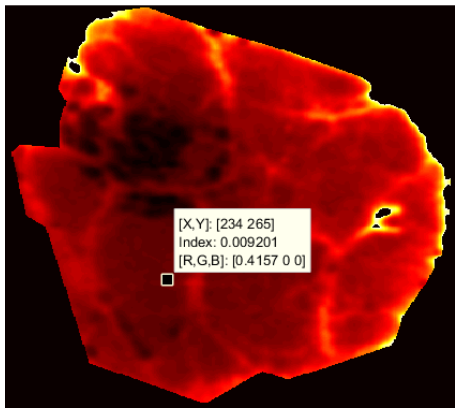
[X,Y]: [234 265]
Index: 0.009201
[R,G,B]: [0.4157 0 0]

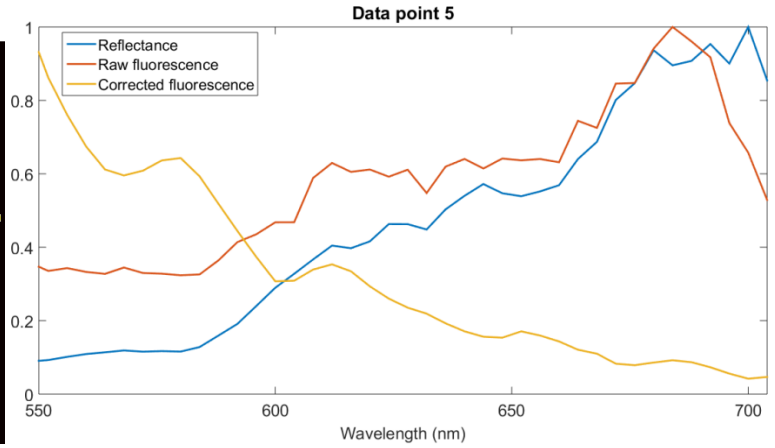
Data point 5
Reflectance
Raw fluorescence
Corrected fluorescence
1
0.8
0.6
0.4
0.2
0
550
600
650
700
Wavelength (nm)

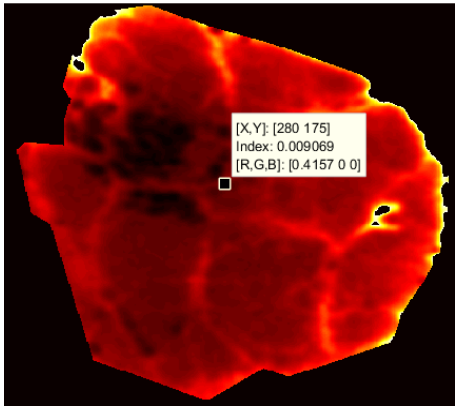
[X,Y]: [280 175]
Index: 0.009069
[R,G,B]: [0.4157 0 0]

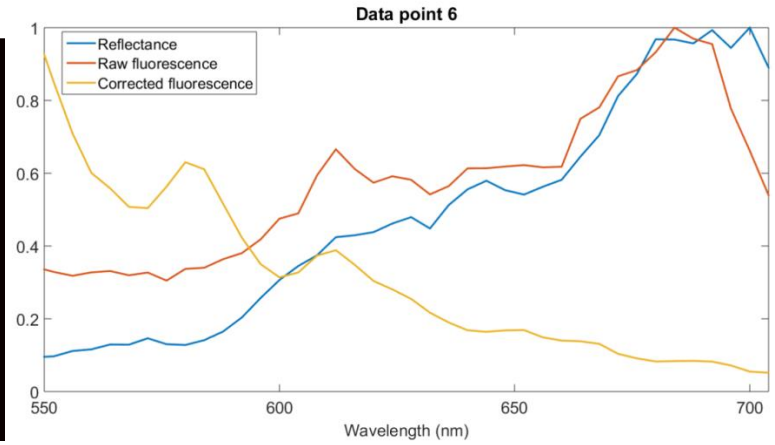
Data point 6
Reflectance
Raw fluorescence
Corrected fluorescence
1
0.8
0.6
0.4
0.2
0
550
600
650
700
Wavelength (nm)

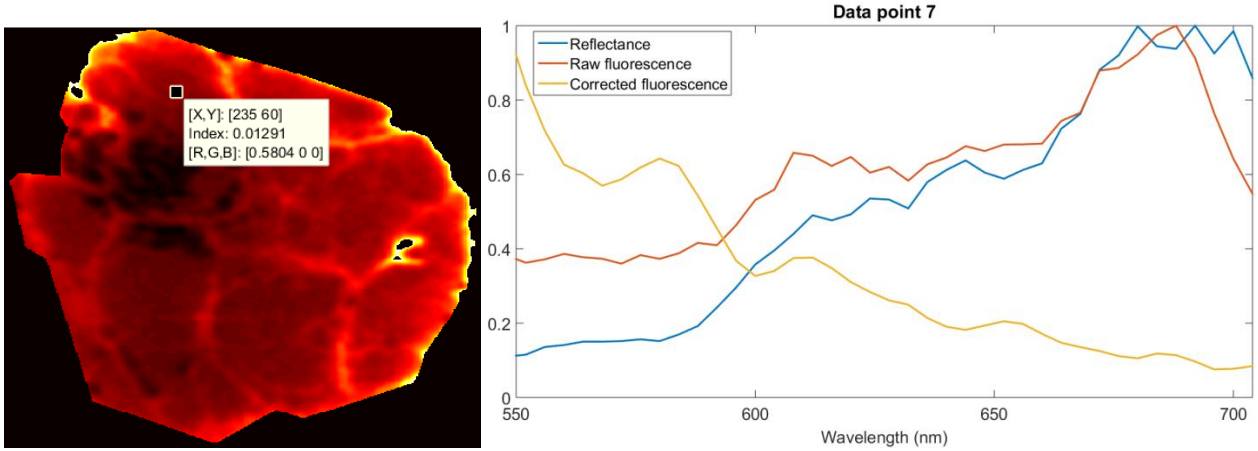
[X,Y]: [235 60]
Index: 0.01291
[R,G,B]: [0.5804 0 0]
Data point 7
Reflectance
Raw fluorescence
Corrected fluorescence
0
0.2
0.4
0.6
0.8
1
550
600
650
700
Wavelength (nm)

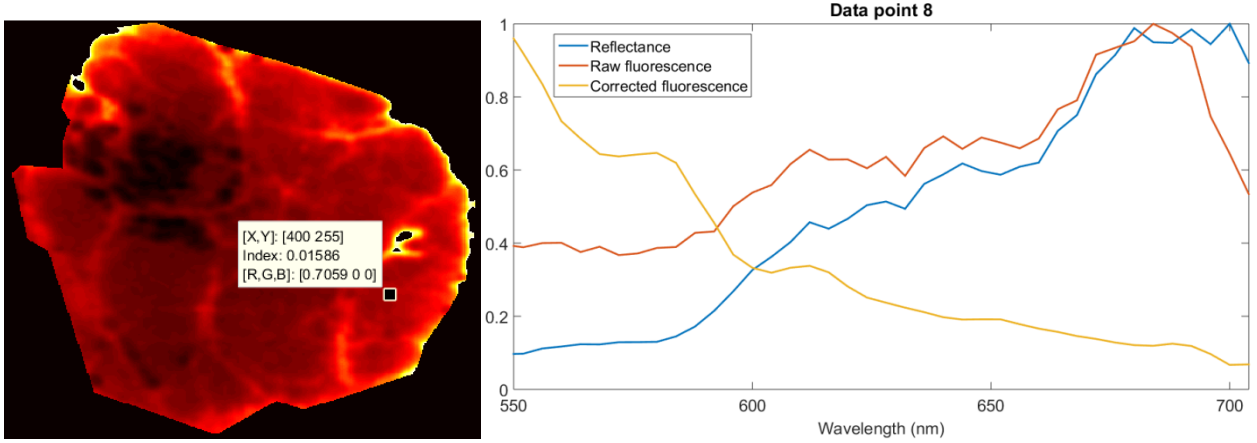
[X,Y]: [400 255]
Index: 0.01586
[R,G,B]: [0.7059 0 0]
Data point 8
Reflectance
Raw fluorescence
Corrected fluorescence
0
0.2
0.4
0.6
0.8
1
550
600
650
700
Wavelength (nm)

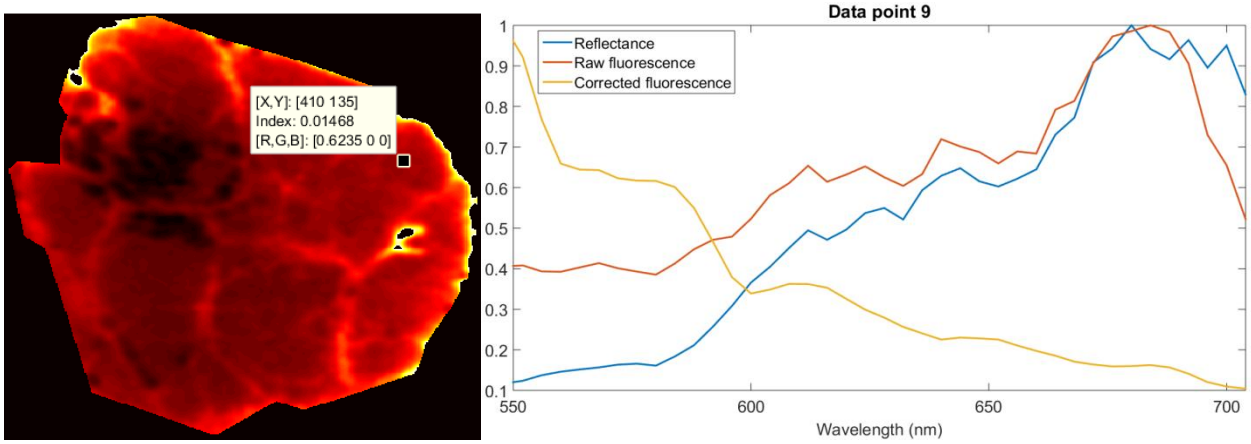

ii. Fluorescence images from the end of the surgery

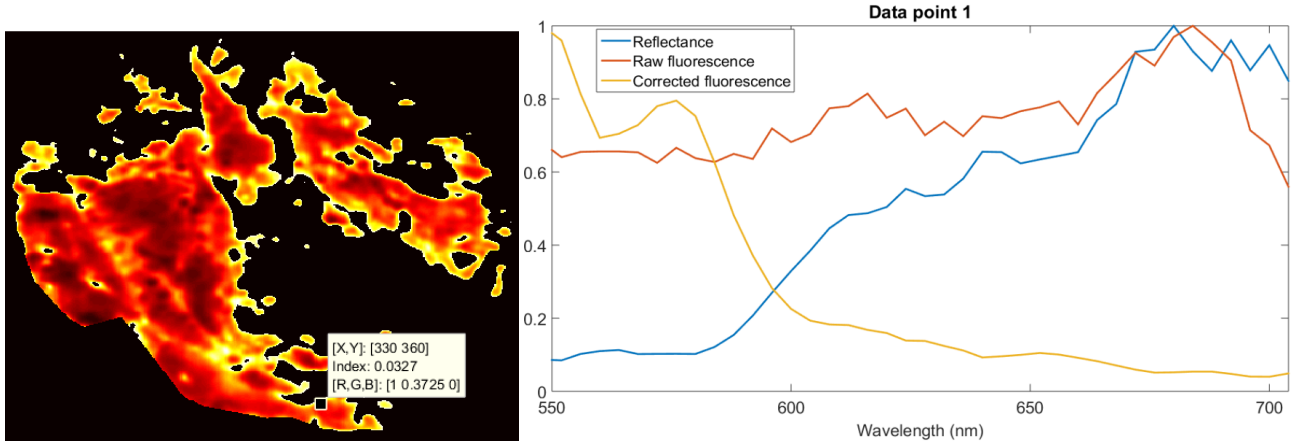

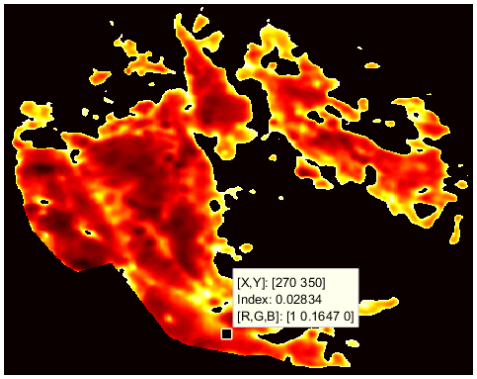
[X,Y]: [270 350]
Index: 0.02834
[R,G,B]: [1 0.1647 0]

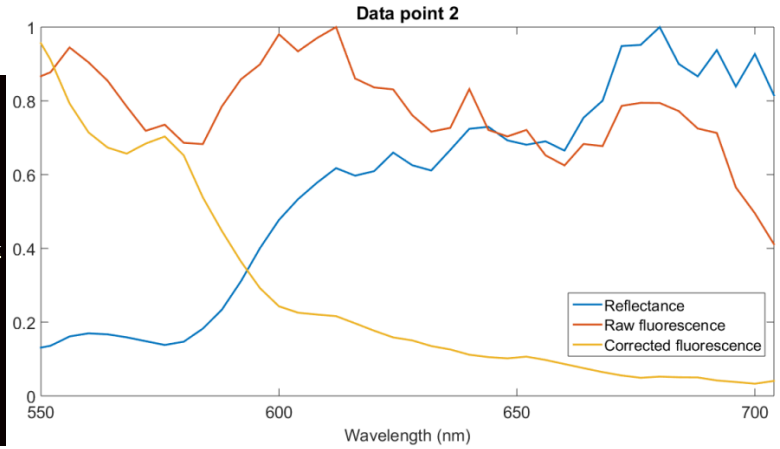
Data point 2
1
0.8
0.6
0.4
0.2
0
550
600
650
700
Wavelength (nm)
Reflectance
Raw fluorescence
Corrected fluorescence

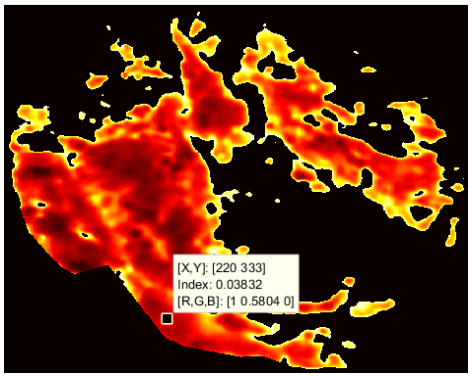
[X,Y]: [220 333]
Index: 0.03832
[R,G,B]: [1 0.5804 0]

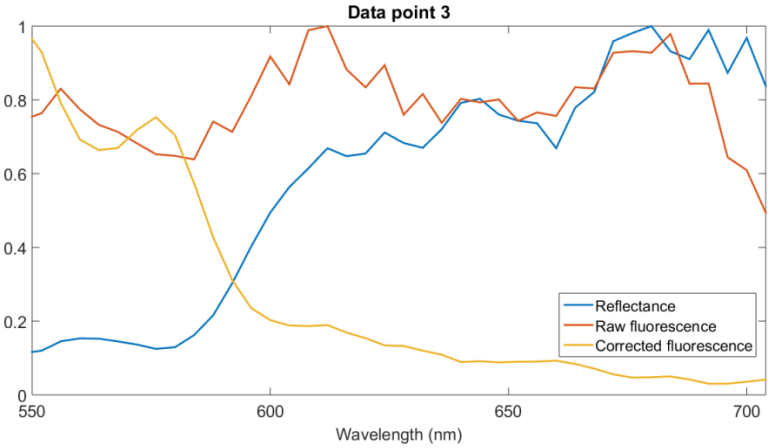
Data point 3
1
0.8
0.6
0.4
0.2
0
550
600
650
700
Wavelength (nm)
Reflectance
Raw fluorescence
Corrected fluorescence

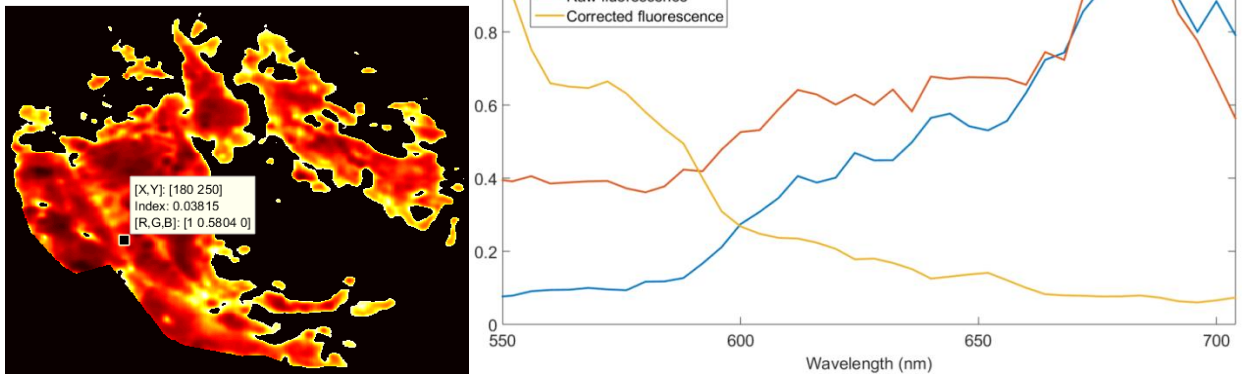
[X,Y]: [180 250]
Index: 0.03815
[R,G,B]: [1 0.5804 0]
Data point 4
Reflectance
Raw fluorescence
Corrected fluorescence
0
0.2
0.4
0.6
0.8
1
550
600
650
700
Wavelength (nm)

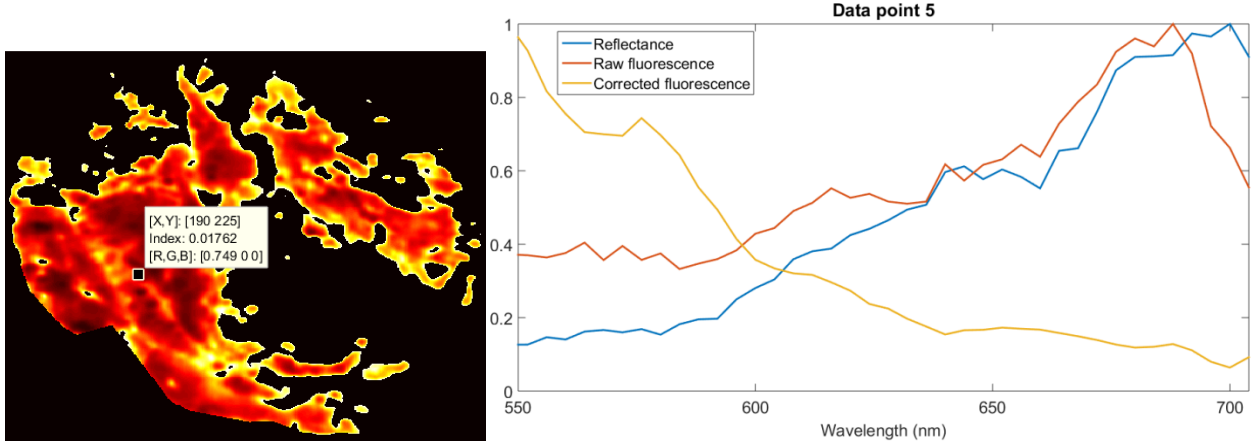
[X,Y]: [190 225]
Index: 0.01762
[R,G,B]: [0.749 0 0]
Data point 5
Reflectance
Raw fluorescence
Corrected fluorescence
0
0.2
0.4
0.6
0.8
1
550
600
650
700
Wavelength (nm)

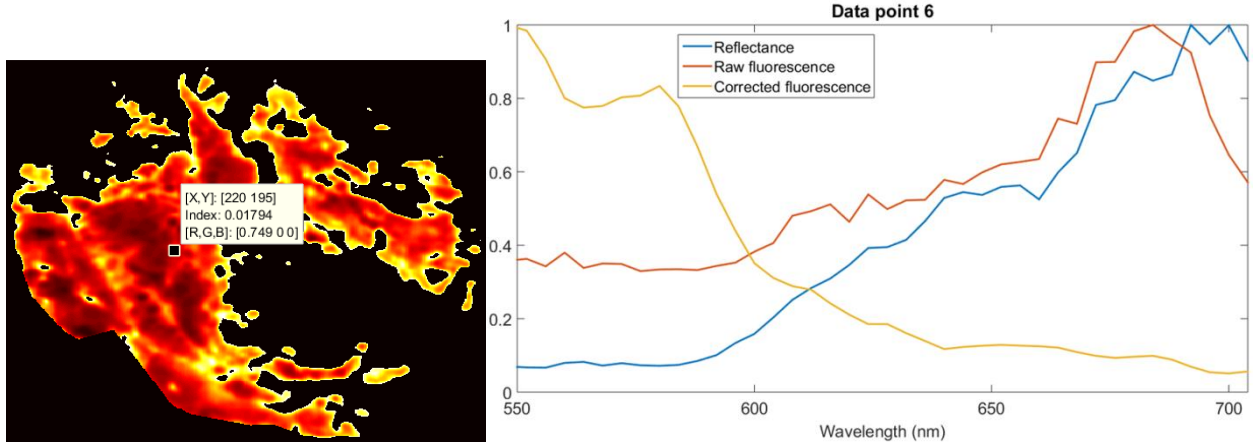
[X,Y]: [220 195]
Index: 0.01794
[R,G,B]: [0.749 0 0]
Data point 6
Reflectance
Raw fluorescence
Corrected fluorescence
1
0.8
0.6
0.4
0.2
0
550
600
650
700
Wavelength (nm)

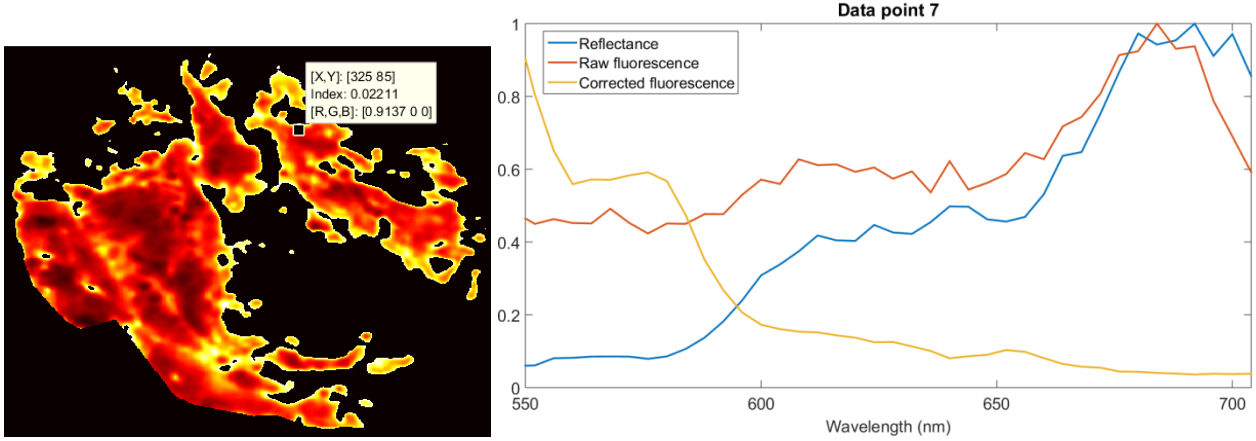
[X,Y]: [325 85]
Index: 0.02211
[R,G,B]: [0.9137 0 0]
Data point 7
Reflectance
Raw fluorescence
Corrected fluorescence
1
0.8
0.6
0.4
0.2
0
550
600
650
700
Wavelength (nm)

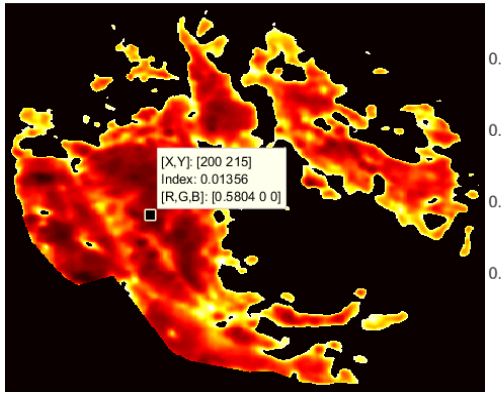
[X,Y]: [200 215]
Index: 0.01356
[R,G,B]: [0.5804 0 0]

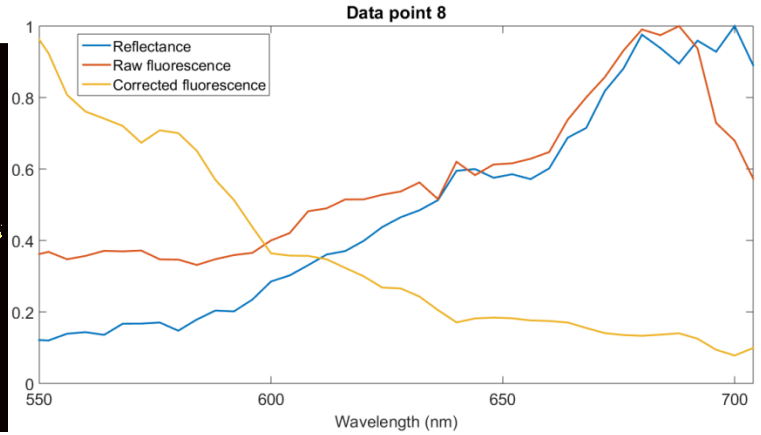
Data point 8
Reflectance
Raw fluorescence
Corrected fluorescence
1
0.8
0.6
0.4
0.2
0
550
600
650
700
Wavelength (nm)

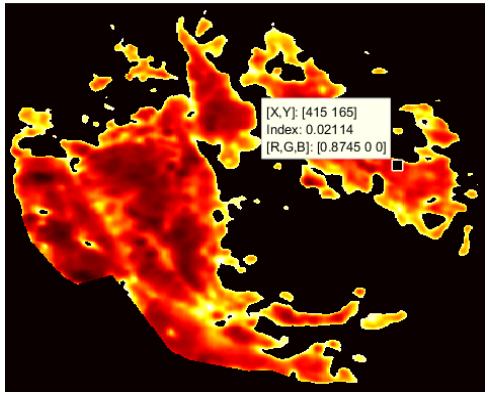
[X,Y]: [415 165]
Index: 0.02114
[R,G,B]: [0.8745 0 0]

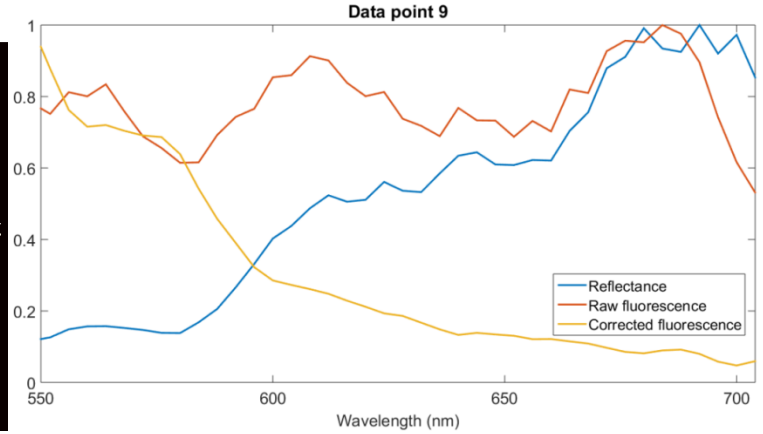
Data point 9
Reflectance
Raw fluorescence
Corrected fluorescence
1
0.8
0.6
0.4
0.2
0
550
600
650
700
Wavelength (nm)

iii. Evaluation of bleed-through from the fluorescence excitation source

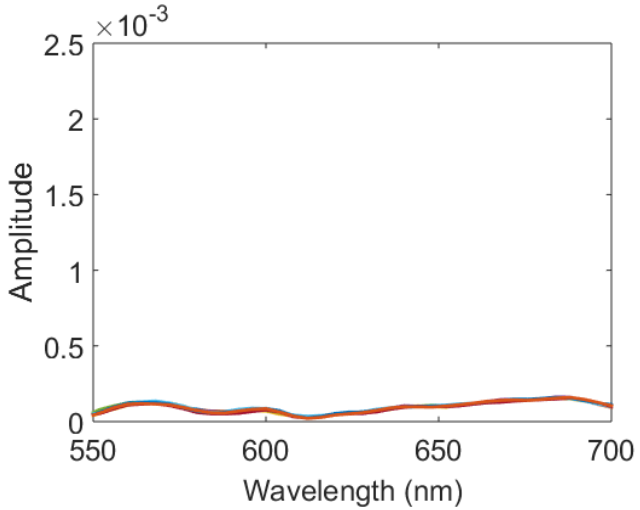

Figure C-1: The plot represents nine signals for different image coordinates of a Spectralon when it was under blue illumination with the microscope source. These signals indicate the amplitude and spectral shape of bleed-through from the excitation source that could possibly be present in *in vivo* autofluorescence signals of the brain.